Passivation strategies for the optimization of perovskite solar cells

Department of Electrical and Information Engineering.

Electrical and Information Engineering Ph.D. Program.

SSD: CHEM-02/A; CHEM-03/A

Final Dissertation.

Passivation strategies for the optimization of perovskite solar cells.

by

Supervisors:

Coordinator of Ph.D. Program:

Course n°37, 01/01/2021-31/12/2024

La sottoscritta Francesca Russo nata a Canosa di Puglia il 14/09/89 residente a San Ferdinando di Puglia in via Dante Alighieri n.84 e-mail francesca.russo@poliba.it iscritto al 3° anno di Corso di Dottorato di Ricerca in Smart and Sustainable Industry (industry 4.0) ciclo 37° area green, ed essendo stato ammesso a sostenere l'esame finale con la prevista discussione della tesi dal titolo:

Passivation strategies for the optimization of perovskite solar cells.

DICHIARA

1) di essere consapevole che, ai sensi del D.P.R. n. 445 del 28.12.2000, le dichiarazioni mendaci, la falsità negli atti e l'uso di atti falsi sono puniti ai sensi del codice penale e delle Leggi speciali in materia, e che nel caso ricorressero dette ipotesi, decade fin dall'inizio e senza necessità di nessuna formalità dai benefici conseguenti al provvedimento emanato sulla base di tali dichiarazioni;
2) di essere iscritto al Corso di Dottorato di ricerca in Smart and Sustainable Industry (industry 4.0) ciclo 37°, corso attivato ai sensi del "Regolamento dei Corsi di Dottorato di ricerca del Politecnico di Bari", emanato con D.R. n.286 del 01.07.2013;
3) di essere pienamente a conoscenza delle disposizioni contenute nel predetto Regolamento in merito alla procedura di deposito, pubblicazione e autoarchiviazione della tesi di dottorato nell'Archivio Istituzionale ad accesso aperto alla letteratura scientifica;
4) di essere consapevole che attraverso l'autoarchiviazione delle tesi nell'Archivio Istituzionale ad accesso aperto alla letteratura scientifica del Politecnico di Bari (IRIS-POLIBA), l'Ateneo archivierà e renderà consultabile in rete (nel rispetto della Policy di Ateneo di cui al D.R. 642 del 13.11.2015) il testo completo della tesi di dottorato, fatta salva la possibilità di sottoscrizione di apposite licenze per le relative condizioni di utilizzo (di cui al sito http://www.creativecommons.it/Licenze), e fatte salve, altresì, le eventuali esigenze di "embargo", legate a strette considerazioni sulla tutelabilità e sfruttamento industriale/commerciale dei contenuti della tesi, da rappresentarsi mediante compilazione e sottoscrizione del modulo in calce (Richiesta di embargo);

5) che la tesi da depositare in IRIS-POLIBA, in formato digitale (PDF/A) sarà del tutto identica a quelle **consegnate**/inviate/da inviarsi ai componenti della commissione per l'esame finale e a qualsiasi altra copia depositata presso gli Uffici del Politecnico di Bari in forma cartacea o digitale, ovvero a quella da discutere in sede di esame finale, a quella da depositare, a cura dell'Ateneo, presso le Biblioteche Nazionali Centrali di Roma e Firenze e presso tutti gli Uffici competenti per legge al momento del deposito stesso, e che di conseguenza va esclusa qualsiasi responsabilità del Politecnico di Bari per quanto riguarda eventuali errori, imprecisioni o omissioni nei contenuti della tesi;

6) che il contenuto e l'organizzazione della tesi è opera originale realizzata dal sottoscritto e non compromette in alcun modo i diritti di terzi, ivi compresi quelli relativi alla sicurezza dei dati personali; che pertanto il Politecnico di Bari ed i suoi funzionari sono in ogni caso esenti da responsabilità di qualsivoglia natura: civile, amministrativa e penale e saranno dal sottoscritto tenuti indenni da qualsiasi richiesta o rivendicazione da parte di terzi;

7) che il contenuto della tesi non infrange in alcun modo il diritto d'Autore né gli obblighi connessi alla salvaguardia di diritti morali od economici di altri autori o di altri aventi diritto, sia per testi, immagini, foto, tabelle, o altre parti di cui la tesi è composta.

Luogo e data BARI, 09/04/25. *Firma* 

La sottoscritta, con l'autoarchiviazione della propria tesi di dottorato nell'Archivio Istituzionale ad accesso aperto del Politecnico di Bari (POLIBA-IRIS), pur mantenendo su di essa tutti i diritti d'autore, morali ed economici, ai sensi della normativa vigente (Legge 633/1941 e ss.mm.ii.),

CONCEDE

- *al Politecnico di Bari il permesso di trasferire l'opera su qualsiasi supporto e di convertirla in qualsiasi formato al fine di una corretta conservazione nel tempo. Il Politecnico di Bari garantisce che non verrà effettuata alcuna modifica al contenuto e alla struttura dell'opera.*

- *al Politecnico di Bari la possibilità di riprodurre l'opera in più di una copia per fini di sicurezza, back-up e conservazione.*

Luogo e data BARI, 09/04/25. *Firma* 

Tauc of contents.

List of Acronyms.

Absorption coefficient (α)

Air Mass (AM)

Attenuated Total Reflectance - Fourier Transform Infrared Spectroscopy (ATR-FTIR).

Bathocuproine (BCP)

Cesium Iodide (CsI)

Cesium lead triiodide ($CsPbI_3$)

Chlorobenzene (CB)

Crystalline silicon (c-Si)

Current Density at Maximum Power Point (J_{MPP})

Dielectric constant (ε)

Diffuse radiation (G_d)

Dimethylammonium chloride (DMACl)

Dimethylformamide (DMF)

Dimethylammonium lead triiodide ($DMAPbI_3$)

Dimethyl sulfoxide (DMSO)

2-(3,6-Dimethoxy-9H-carbazol-9-yl)ethyl]phosphonic Acid (MeO-2PACZ)

Direct radiation (G_b)

Electron Transport Layer (ETL)

Electrochemical Impedance Measurements (EIS)

Energy gap (E_g)

Fill Factor (FF)

Formamidinium iodide (FAI, $CH(NH_2)_2I$)

formamidinium lead triiodide ($HC[NH_2]_2PbI_3$, $FAPbI_3$, FAPI)

Frequency (v)

Fullerene (C_{60})

Global radiation (G_g)

Goldschmidt tolerance factor (t)

2-(9H-carbazol-9-yl)ethyl]-phosphonic acid (2PACZ)

Highest Occupied Molecular Orbital (HOMO)

Hole Transport Layer (HTL)

Incident-photon-to current conversion efficiency (IPCE)

Incoming Light Power (P_{in})

Lead iodide (PbI_2)

Lowest Unoccupied Molecular Orbital (LUMO)

Low-Temperature (LT)

Metal halide perovskites (MHPs)

Methylammonium iodide (MA, CH_3NH_3I)

Methylammonium Lead Iodide Bromide ($MAPb(I_{1-x}Br_x)_3$)

Methylammonium lead triiodide ($CH_3NH_3PbI_3$, $MAPbI_3$, MAPI)

N-methyl-2-pyrrolidone (NMP)

Open-circuit voltage (Voc)

2,2′,2″,2‴-((perchlorocyclohexa-2,5-diene-1,4-diyliene)bis(methanediylyldene))tetrakis-(1,3,5-trichlorobenzene) (TTH)

Perovskite Solar Cells (PSCs)

6,6-Phenyl C61 butyric acid methyl ester (PCBM)

Photoluminescence (PL)

Photovoltaic (PV)

Poly[bis(4-phenyl)(2,4,6-trimethylphenyl)amine] (PTAA)

Poly(3,4-ethylenedioxythiophene)-poly(styrenesulfonate) (PEDOT:PSS)

Power Conversion Efficiencies (PCE)

Planar Heterojunction (PHJ)

Planck's constant (h)

Poly(3-hydroxybutyrate) (PHB)

Poly(3-hexylthiophene-2,5-diyl) (P3HT)

Reactive Oxygen Species (ROS)

Reflected radiation (G_r)

Relative Humidity (RH)

Room-Temperature (RT)

Scanning Electron Microscopy (SEM)

Series Resistance (R_s)

Silver (Ag)

Shockley-Queisser index ($\mathscr{E}_{SQ}$)

Short-Circuit Current/density (Isc, Jsc)

Shunt Resistance (R_{sh})

Solar irradiance (G)

Standard Testing Conditions (STC)

2,2′,7,7′-tetrakis(N,N-pdimethoxyphenylamino)-9,9′-spirobifluorene (spiro-OMeTAD)

X-Ray diffraction (XRD)

X-ray Photoelectron Spectroscopy (XPS).

Voltage at Maximum Power Point (V_{MPP})

Zenith angle (θ_Z).

Abstract.

This thesis focuses on developing environmentally sustainable strategies to enhance the performance, stability, and scalability of PSCs, among the most promising PV technologies of the current scenario.

The experimental results are organized in three sections, chapters 3 to 5, the first one employing bio-derived materials as components of the PSC device foreseeing the amelioration of the photoactive film characteristics combined with the engineering of device interfaces. In details, chapter 3 reports on the use of β-carotene and PHB, to improve the environmental stability and optoelectronic properties of perovskite films. β-carotene, which scavenges oxidizing species, mitigates perovskite degradation, leading to increased material stability and prolonged charge carrier lifetimes. Devices incorporating β-carotene achieve a PCE of 20%, highlighting its potential to improve the lifespan and sustainability of solar cells. Similarly, PHB, a biodegradable polymer, enhances the mechanical flexibility and crystalline quality of perovskite films, and surpasses the reference efficiency, achieving a PCE of 9.3%. This suggests the potential of PHB to contribute to the development of more sustainable, flexible, and eco-friendly perovskite-based devices. The second section is focused on the key role of device interfaces for fully inorganic $CsPbI_3$-based solar cells.

The incorporation of PCBM as an interlayer between C_{60} and $CsPbI_3$ enhances energy level alignment and reduces defects, contributing to more efficient charge transfer. Successively, the introduction of TTH as a novel interlayer further improves device performance, with a PCE of 8.12% surpassing the reference efficiency of 6%, by reducing interfacial recombination and facilitating efficient charge separation. These innovations demonstrate the potential to optimize perovskite-based devices for more sustainable energy solutions.

Finally, in chapter 5 plasma-based treatments are explored as environmentally friendly surface modification methods for $MAPbI_3$ perovskite films. Plasma treatments with gases like Ar and H_2 enhance device performance by selectively removing organic components and introducing chemical functionalities that improve the stability and efficiency of the interfaces. Unlike traditional chemical treatments, plasma-based methods offer a less invasive and potentially more eco-friendly approach to surface engineering.

In conclusion, this thesis demonstrates the potential of combining bio-inspired additives, interlayer engineering, and plasma treatments to address key challenges in perovskite solar cell technology. These advancements not only improve the efficiency and stability of the devices but also pave the way for the development of more environmentally sustainable and scalable photovoltaic solutions, contributing to the global transition towards clean and renewable energy sources.

Chapter 1

Introduction.

Modern industry is shifting towards a "smart and sustainable" model, driven by the adoption of advanced technologies enhancing efficiency and reducing environmental impact. This shift is fueled by the energy demand rising, linked to global population growth, and the need to address the depletion of non-renewable resources like fossil fuels, which contribute to widespread environmental challenges. As a result, the transition to renewable energy is rapidly accelerating. Solar energy stands out as one of the most promising renewable sources due to its abundance, cleanliness, and inexhaustibility. With solar radiation reaching about 1 kW/m² at the Earth's surface [1], it offers immense potential for sustainable energy generation. Among renewable technologies-such as solar heating, artificial photosynthesis, photocatalytic water-splitting, wind energy and hydroelectric power- PV has gained significant attention for its scalability and versatility, suitable for both large-scale power plants and residential or commercial systems.
Currently, the photovoltaic market is dominated by single-junction crystalline silicon (c-Si) devices, which achieve PCE above 26% under standard solar illumination (AM 1.5) [2]. Recent reductions in production costs for high-quality c-Si solar cells have accelerated the adoption of photovoltaics, making them a more viable solution for large-scale energy generation. As a result, forecasts predict that photovoltaics will account for nearly a third of global electricity generation capacity by 2030 [3].
However, c-Si production process is energy-intensive and involves the use of water and caustic chemicals such as sodium hydroxide and hydrofluoric acid, leading to environmental concerns. Emerging PV technologies, such as thin-film solar cells (<1 mm) with simple deposition methods, hold promises for reducing production costs and improving semiconductor quality. Among these, metal halide PSCs have emerged in the last decade as a promising alternative [4]. PSCs stand out due to their high efficiency, low-cost fabrication, and use of earth-abundant materials. Their impressive performance, combined with simple manufacturing methods, makes them highly competitive with traditional c-Si solar cells. There are still issues that need to be solved for allowing PSCs on the market, among which their instability to heat and moisture and the toxicity of lead. However, ongoing research is developing strategies for addressing these challenges, making PSCs a very promising key player in the solar energy market, complementing or even replacing silicon-based technologies for a more sustainable future.

1.1 Physics of Solar Cells.

1.1.1 Properties of Sunlight.

Solar radiation, denoted by the letter G and measured in W/m², represents the total power emitted by a radiant source that reaches a unit area of a surface. In the context of energy produced by photovoltaic technologies, the reference radiant source is the Sun, which can be considered an ideal emitter of radiation, i.e., a black body. For a unit area, orthogonal to the

incoming solar rays, the solar irradiance G can be obtained by integrating the spectral irradiance distribution g(λ) in $W \cdot m^2 \cdot nm^{-1}$ over the entire wavelength range.

$$G = \int g(\lambda) d(\lambda) \approx 1367 W/m^2 \quad (1.1)$$

Figure 1.1 presents the spectral distribution under two different conditions, namely outside and inside Earth's atmosphere, along with the radiation distribution of an ideal emitter, i.e., a black body.

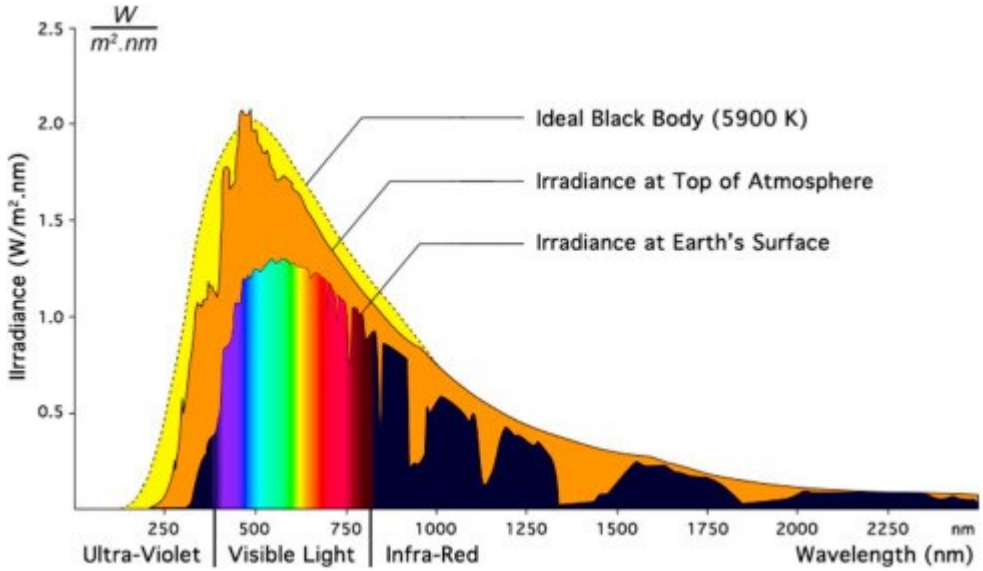

Figure 1.1 Theoretical black body spectrum and full solar spectrum at earth's surface and the top of atmosphere [5].

Incident solar radiation on Earth's surface is classified into three components:
-Direct radiation (G_b): Radiation that reaches the surface without scattering or energy loss, measured in W/m².
-Diffuse radiation (G_d): Radiation scattered by the atmosphere before reaching the ground, also measured in W/m². Under clear skies, direct radiation predominates, with diffuse radiation contributing less than 20% of the total. On cloudy days, diffuse radiation becomes the dominant component.
-Reflected radiation (G_r): Also known as albedo, it represents the portion of radiation reflected from Earth's surface back into the atmosphere, measured in W/m². This reflection is quantified by the reflection coefficient ρ, which depends on the surface's color and the wavelength of incident light. Bright surfaces, like snow, reflect more radiation, while darker surfaces absorb more, reducing the reflection.
Global radiation (G_g) incident on the surface is the sum of the three previously analyzed components.
The intensity of solar radiation reaching the Earth's surface is subject to both daily and annual variations due to the apparent motion of the Sun, as well as changes in meteorological conditions such as cloud cover, rainfall, and atmospheric composition. These factors significantly affect the availability and quality of solar energy, making it crucial to account for local weather conditions when designing a PV system. Accurate measurement of these

conditions near the installation site is essential for optimizing system performance. At ground level, the solar radiation incident on a surface is influenced by the altitude above sea level and the tilt angle of the surface relative to the horizontal plane. Higher altitudes generally receive greater solar irradiance due to reduced atmospheric thickness, while the inclination of the surface determines how effectively it captures sunlight. Another critical factor is the Air Mass (AM), which quantifies the effect of the Earth's atmosphere on solar irradiance. The Air Mass describes the path length that sunlight travels through the atmosphere, which impacts the absorption and scattering of solar radiation. The atmosphere attenuates many parts of the spectrum due to air molecules, dust, particularly water (H_2O), oxygen (O_2), ozone (O_3) and carbon dioxide (CO_2). Ozone absorbs hard ultraviolet light below 300 nm and protects live species from harmful UV effect. CO_2 absorbs radiation above 1 μm and thus preserving infrared radiation from dissipation creating a greenhouse effect. The AM value depends on the angle of incidence, defined by the Zenith angle, θ_Z (*Figure 1.2*). This angle is measured between the incoming solar rays and the perpendicular to the Earth's surface at a given location. As the Zenith angle increases (e.g., during sunrise or sunset), the solar radiation passes through a thicker atmospheric layer, leading to greater attenuation. Conversely, at smaller angles (e.g., near solar noon), the radiation encounters less atmospheric resistance, resulting in higher irradiance levels. Given these factors, the design and optimization of photovoltaic systems require precise knowledge of site-specific conditions. By evaluating variables such as altitude, surface tilt, and Air Mass, engineers can predict the quality and intensity of the solar radiation available, thereby tailoring the system to achieve maximum energy efficiency under local environmental conditions.

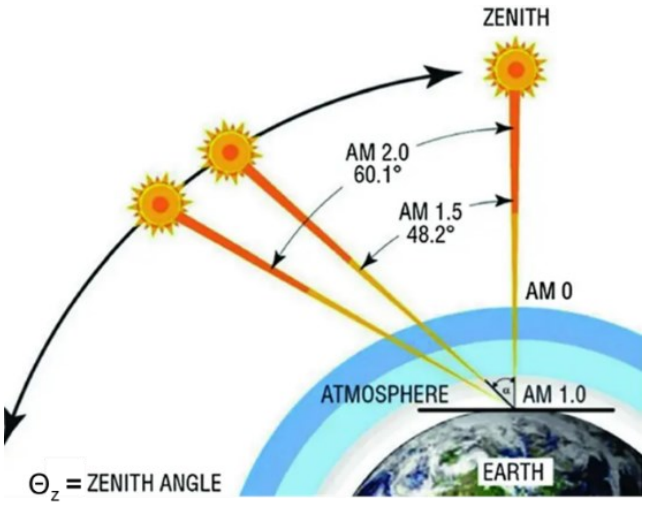

Figure 1.2 Air Mass Spectrum.

The efficiency of a solar cell is influenced by the emission spectrum of the radiation incident on its surface. To enable a fair comparison of the performance of different solar cells exposed to varying solar spectra, standard reference spectra have been defined.
One such standard is AM1.5G, which represents global radiation (including direct, diffuse, and reflected components) under clear sky conditions, with an irradiance of G=1000 W/m^2. Another standard, AM1.5D, accounts only for diffuse radiation.

Additionally, the AM0 spectrum represents extraterrestrial radiation, unaffected by atmospheric interference. This spectrum is particularly relevant for solar cell applications in satellites and space missions.

1.1.2 The Role of Semiconductors in Photovoltaic Energy Conversion.

The photovoltaic effect is a physical phenomenon that occurs when an electron present in the valence band of a material (usually semiconductor) passes to the conduction one, following the absorption of a sufficiently energetic photon. This effect is closely linked to the photoelectric effect for which a metallic surface emits electrons when struck by electromagnetic radiation with a given wavelength. The absorption and the emission occur, therefore, by exchange of photons, or light quanta, whose energy is regulated by Planck's law ($E=h\nu$). Semiconductors, like silicon or perovskites, are materials whose electrical properties and conductivity fall between those conductors and insulators. Their energy levels are characterized by a small E_g that separates the valence band from the conduction band. For an electron to be excited to the conduction band, the incident photon must have an energy ($h\nu$) at least equal to E_g. Photons with insufficient energy cannot be absorbed by the semiconductor and are instead transmitted or reflected.

Once an electron is excited to the conduction band, it quickly loses energy through phonon generation. Upon reaching the bottom of the conduction band, there are no lower-energy electronic states available. To return to the valence band, the electron must release all its excitation energy in a single step. The electron's lifetime within the conduction band is approximately 10^{-9} seconds, during which it can convert its energy into electricity.

The excitation of an electron to the conduction band leaves a hole in the valence band. This hole can be filled by another electron, forming an electrically neutral hole-electron pair. To complete the photovoltaic conversion process, the excited electrons must be separated from the holes.

Key factors in designing photovoltaic cells include the value of the energy gap, the type of semiconductor (direct or indirect), and the density of electronic states in the bands. These properties strongly influence the material's absorption coefficient (α), which determines the relationship $I=I_0e^{-\alpha x}$.

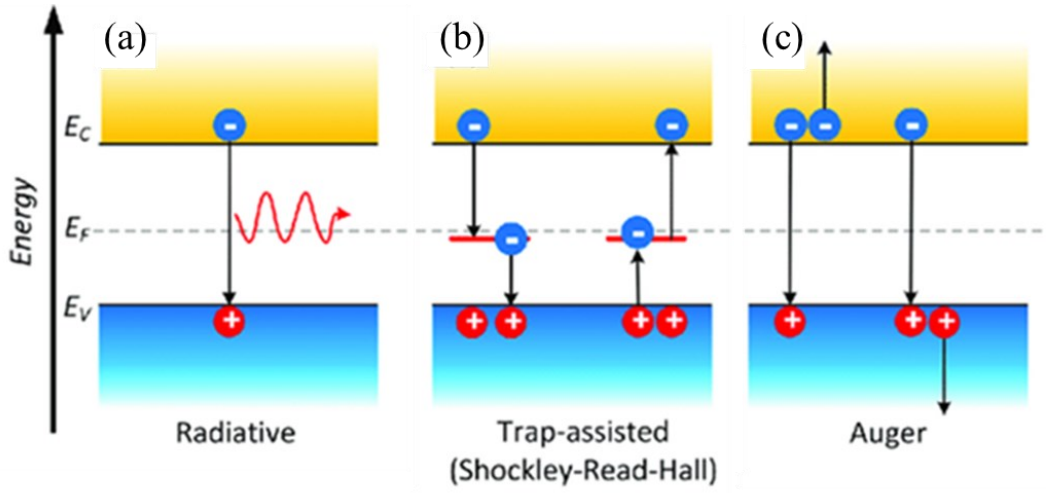

Figure 1.3 Recombination mechanisms in semiconductors. The direct radiative and Auger band-to-band decays are intrinsic processes, whereas the Shockley-Read-Hall (SRH) and surface recombination are extrinsic processes assisted by a defect level in the bandgap. The black arrows indicate the direction of the electron (blue circuit with minus sign) transitions. The holes (red circle with plus sign) travel against the arrow direction. (a) Depicts the schematic of spontaneous radiative recombination, (b) depicts the (e^-) and (h^+) Auger recombination processes, (c) shows the four basic transitions that may occur during SRH recombination [6].

While absorbing solar radiation is essential for the operation of a photovoltaic cell, it is not sufficient on its own. After the absorption of radiation and the generation of hole-electron pairs, the charges must successfully reach the electrodes. Charge carriers are subject to recombination mechanisms, which can reduce efficiency. These mechanisms include band-to-band recombination, trap-assisted recombination (Shockley-Read-Hall), and Auger recombination (*Figure 1.3*).

Band to band is the simplest and most direct form of recombination, it is a bimolecular process (*Figure 1.3a*). It happens when an electron in the conduction band falls back down into a hole in the valence band, releasing energy. This energy can take the form of light (photons) or heat (phonons). Band-to-band recombination is the principle behind how LEDs and semiconductor lasers work, as these devices are designed to emit light efficiently through this process. In the Trap-Assisted Recombination (Shockley-Read-Hall or SRH Recombination), the process is mediated by a defect or impurity in the semiconductor (*Figure 1.3b*). These defects create energy states in the bandgap, which act like steppingstones for electrons or holes. Instead of recombining directly, an electron first gets "trapped" in one of these defect states before recombining with a hole. This type of recombination does not emit light but instead releases energy as heat. It's a monomolecular process because it involves one charge at a time. It's a major loss mechanism in devices like solar cells or LEDs, as it reduces their overall efficiency by wasting energy. Auger recombination is a trimolecular process, the energy of recombination between hole and electron is transferred to a third particle, hole or electron, which is excited (*Figure 1.3c*). Here, the energy released when an electron and hole recombine doesn't produce light or heat directly. Instead, this energy is transferred to another electron (or hole), which gains energy and then loses it as heat. This process becomes significant in devices with high carrier densities, like high-intensity solar cells or semiconductor lasers. Unfortunately, Auger recombination can significantly limit the efficiency of such devices under intense operating conditions.

1.1.3 Solar Cell Working Mechanism.

A solar cell is a device which converts a portion of the energy from visible radiation to electrical current, which can flow in an external circuit against a certain potential. This conversion starts with the absorption of light from the active material and the subsequent generation of an exciton. In inorganic semiconductors, excitons are typically formed only at low temperatures. When sunlight strikes a solar cell, electrons in the silicon are ejected, leaving behind "holes", the vacancies created by the escaping electrons. After the separation of the exciton, the positive and negative charges are collected, and current can flow through the solar cell to the external circuit. For such separation to be effective, the solar cell needs an internal electric field, which is called built-in electric field. Ideally, the solar cell can be modelized with an equivalent circuit, which consists of a load and a diode. This simplified model is known as the Shockley diode, as represented in *Figure 1.4*. This model contains a diode with current-voltage curve I_{dark} which follows the Shockley diode equation in parallel with a current source that generates a voltage-independent photocurrent. When the solar cell is illuminated, it generates a photocurrent proportional to the light intensity. The diode supplies the voltage to drive the generated photocurrent through the load.

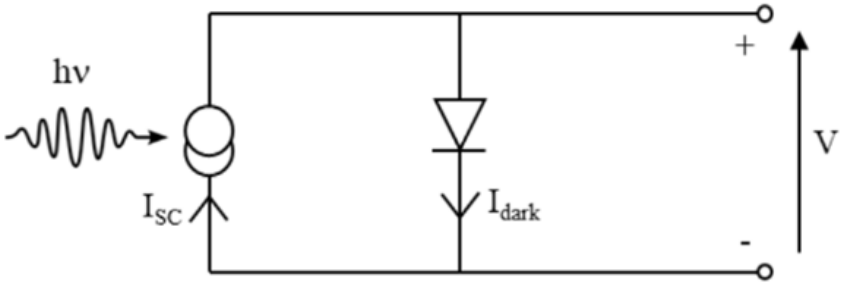

Figure 1.4 Equivalent circuit of an ideal solar cells as per the Shockley model [7].

1.2 Solar Cells Characterizations.

This paragraph addresses the methods used to characterize solar cell devices, focusing on how their response to optical and electrical stimuli is determined. Device characterization is directly tied to the final product and, consequently, to the overarching goal of all research efforts: achieving an efficient solar cell. However, since these measurements evaluate the device as an integrated system, interpreting the results can be challenging. This difficulty arises from the fact that many optical and electronic phenomena contribute to relatively generalized outcomes, such as current-voltage curves. Therefore, the key challenge in device characterization lies not only in performing accurate measurements but also in interpreting the data, a process often supported by device simulations.

To compare different PV systems and achieve an optimal design for a PV system, it is essential to understand the current-voltage (I-V) characteristics of the individual PV module used in the system.

From the formula it is evident how only photons whose wavelength will be greater than that given by the work function, will be able to produce photoelectrons.

1.2.1 Measurement of I/V Curves.

Illuminated I/V curves are generally measured under standard testing conditions (STC), 25°C AM1.5 1 sun [8]. The J/V curve (*Figure 1.5*) is a key tool for assessing solar cell performance, illustrating how current density (J, in A/cm²) changes with varying voltage (V). It provides critical parameters such as short-circuit current (J_{sc}), open-circuit voltage (V_{oc}), fill factor (FF), and overall energy conversion efficiency.

Four figures of merit can be extracted from this measurement [4]:

V_{oc} is the maximum voltage reached by the solar cell when the current is zero. It is determined by the electronic properties of the material, such as the bandgap. With larger bandgaps typically leading to higher V_{OC}. Other factors influencing V_{OC} include the built-in potential of the junction, the quality of the charge carrier collection at the interface, and the extent of carrier recombination.

Isc is the maximum current generated by the cell when the applied voltage is zero. It is primarily determined by the number of photogenerated charge carriers, which depend on factors such as the light absorption efficiency of the active material, the device thickness, and the quality of the material. The higher the absorption and the better the charge carrier collection, the higher the I_{SC}. Additionally, recombination losses, especially bulk recombination in the absorber material, can reduce I_{SC}. The short-circuit current density (J_{SC}) replaces the I_{SC} to remove the dependence on the illuminated area. The unit of measurement for J_{SC} is amperes per square centimeter (A/cm²).

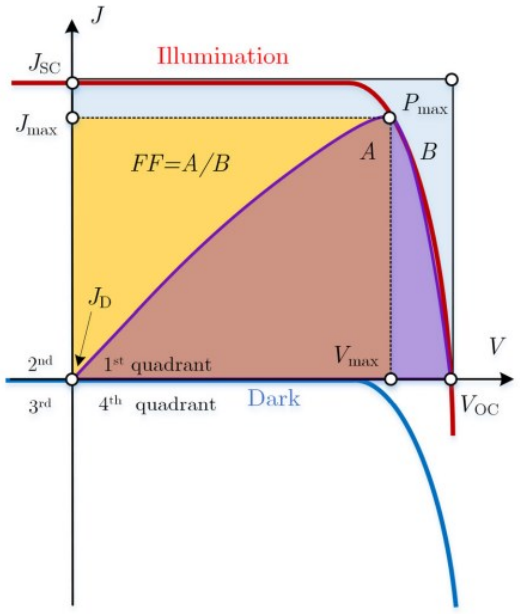

Figure 1.5 Example of J-V curve for a solar cell under light (red line) and durk (blue line) conditions. The yellow rectangle represents the maximum power spanned by V_{MPP} and J_{MPP}. The rectangle spanned by the dotted red line indicates the theoretical maximum power from V_{OC} and J_{SC}. The ratio between these two figures represents the FF.

.

FF reflects the "squareness" of the solar cell's J/V curve. FF provides insight into the efficiency of the solar cell in converting the photogenerated charge carriers into usable electrical power. It is influenced by the series resistance (R_s) and shunt resistance (R_{sh}), where higher series resistance or lower shunt resistance results in a lower FF. Additionally, recombination losses, particularly at the interfaces, can reduce FF by limiting the number of charge carriers that contribute to the current output. Therefore, FF can be calculated as follows equation 1.2:

$$FF = \frac{J_{MPP}\, V_{MPP}}{J_{SC}\, V_{OC}} \tag{1.2}$$

The R_s refers to the resistive losses in the current path from the active layer to the external circuit, including the contacts, interconnects, and any other resistive components in the device (*Figure 1.6*). High series resistance limits the amount of current that can flow through the solar cell, especially under high voltage conditions, which reduces the fill factor and the efficiency of the device. Series resistance is particularly important in high current regimes, as it causes a voltage drop and power loss.

R_{sh} represents the unwanted conductive paths that allow current to leak through the solar cell, by passing the active material and reducing the amount of current that flows through the external load (*Figure 1.6*). Shunt resistance typically arises due to defects, such as pinholes, cracks, or poor material interfaces, which create these leakage paths. Low R_{sh} increases leakage currents, particularly at lower voltages, and results in a reduced fill factor. High shunt resistance, on the other hand, minimizes such leakage and ensures that more of the photogenerated current is delivered to the external circuit.

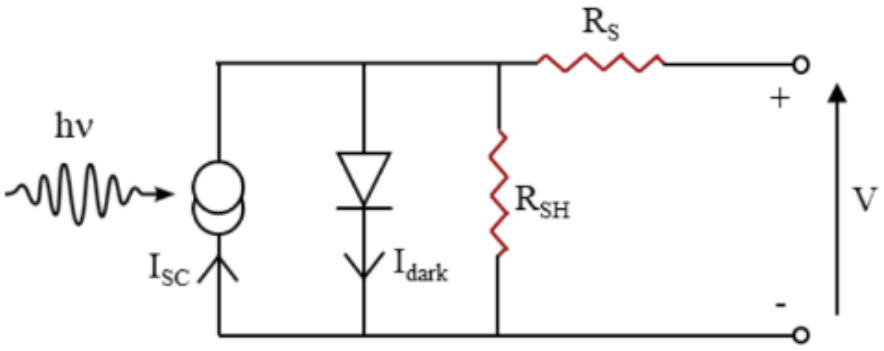

Figure 1.6 Equivalent circuit of real solar cells including series and shunt resistances [7].

PCE of the solar cell represents the ratio between the power delivered at the MPP and the incoming light power P_{in}. To achieve high efficiency, a solar cell must maximize I_{SC} through high light absorption and effective charge collection, maintain a high V_{OC} for efficient energy conversion, and optimize FF by minimizing resistive losses and recombination.

$$PCE = \frac{V_{MPP}\, J_{MPP}}{P_{in}} = \frac{V_{OC}\ J_{SC}\, FF}{P_{in}} \tag{1.3}$$

In summary, I_{SC} is influenced by the absorption characteristics and charge carrier dynamics, V_{OC} by the material's electronic properties and junction quality, and FF by resistive losses and recombination. Optimizing these parameters requires balancing material choice, device architecture, and fabrication processes to minimize losses and maximize the conversion of light into electricity.

1.3 The Evolution of Solar Cell Technologies.

1.3.1 Designing the Ideal Absorber for Photovoltaic Cells.

Designing an ideal absorber for a photovoltaic cell requires achieving a delicate balance between efficient optical absorption and effective charge transport. A crucial characteristic of such a material is its ability to absorb light across a broad spectral range, particularly from 350 nm to 950 nm. This ensures that the material captures a significant portion of the solar spectrum, especially near its peak, and aligns with an optimal bandgap energy of 1 to 1.5 eV. Such a range maximizes the energy harnessed from sunlight, which is essential for high efficiency. Equally important is the capacity of the material to facilitate the movement of electron-hole pairs toward the electrodes with minimal losses due to recombination. Efficient charge transport is fundamental to converting absorbed light into electrical energy with the least possible wastage, thereby optimizing the device's overall performance. The internal field that mobilizes the charges is directly related to the bandgap; therefore, it cannot be reduced excessively without compromising the device's functionality. Additionally, the material must be cost-effective and composed of elements that are abundant in nature. This ensures scalability and widespread adoption, as production costs and resource availability are key factors in transitioning photovoltaic technologies from laboratories to practical applications. Stability and durability are also critical considerations. The material must withstand harsh operational conditions, such as exposure to high temperatures and moisture, while maintaining its performance over extended periods. This resilience is essential for ensuring long-term reliability and economic feasibility. Finally, minimizing environmental impact throughout the material's lifecycle, from extraction and production to disposal, is vital. A sustainable approach not only addresses ecological concerns but also aligns with the broader goal of renewable energy technologies to reduce humanity's carbon footprint.

As previously discussed, the absorption limit of a material is inherently tied to the solar radiation spectrum, which defines the amount of light that can be captured by a solar cell. While no material can absorb all incident radiation, the goal is to develop materials that perform efficiently near the spectrum's peak. The optimal bandgap value of the material is thus constrained by this spectral consideration and by the need to maximize the cell's power output. When the E_g of the material is too low, it absorbs a significant amount of light, but the energy of the generated charge carriers will be minimal. This leads to a high current but a low voltage, ultimately reducing the output power. On the other hand, if E_g is too high, the material absorbs less light, but the energy of the charge carriers increases. In this case, the current is low, but the voltage is high, which also limits the overall power output. Therefore, achieving the right balance between these two extremes is crucial for optimizing efficiency.

This balance between current and voltage is essential in understanding the performance of photovoltaic cells. In this context, the Shockley-Queisser (SQ) index ($\mathscr{E}_{SQ}$) plays a critical role in quantifying the capacity of a solar cell technology to approach its theoretical efficiency limit. The $\mathscr{E}_{SQ}$ is derived from the detailed balance model, which considers how efficiently the semiconductor's bandgap(s) can convert the solar spectrum into electrical energy as shown in equation 1.4 and *Figure 1.6*:

$$PCE_{SQ}(Eg) = 1 - \frac{Eg}{Eg+0,5} \tag{1.4}$$

$$\mathcal{E}_{SQ} = \frac{PCE}{PCE_{SQ}} \tag{1.5}$$

The $\mathscr{E}_{SQ}$ according to the equation 1.5, basically reflects the ratio between the conversion efficiency of a "real" solar cell (i.e., affected by limiting effects, such as series resistance losses, non-radiative recombination, or overheating above the ambient temperature) and the "ideal" Shockley Queisser efficiency of the cell (a value close to 1 indicating a "close to ideal" behaviour of the cell, while a value approaching 0 denotes strong "non-ideal" losses).

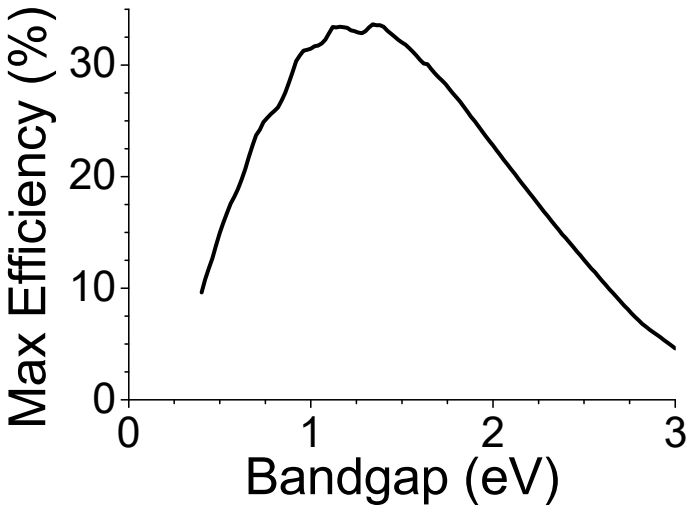

Figure 1.7 The Shockley-Queisser limit for the maximum achievable efficiency of a solar cell, with the x-axis representing the bandgap of the solar cell and the y-axis showing the theoretical maximum efficiency (ratio of electrical power output to light power input), assuming a single-junction solar cell under AM1.5.

It is important to note, however, that a high S-Q index does not automatically imply that the cell itself will have high conversion efficiency. The theoretical limit determined by the detailed balance model is closely tied to the intrinsic properties of the semiconductor material, particularly its bandgap(s). For single-junction devices, this means that the bandgap must be tailored to efficiently absorb the most relevant portion of the solar spectrum. In the case of multijunction devices, multiple bandgaps are optimized to cover a broader range of the solar spectrum. Therefore, understanding the mechanisms that limit the $\mathscr{E}_{SQ}$, such as recombination losses and suboptimal E_g absorption, is key to developing solar cells that can achieve efficiencies close to this theoretical limit [9].

From *Figure 1.7* it can be deduced that the perfect solar absorber can have a maximum theoretical efficiency of approximately 33% when the E_g value is about 1.3/1.4 eV. The "ideal" solar cell, as described by Shockley and Queisser in their detailed balance model, is based on a set of simplifying assumptions that help to define its theoretical efficiency limit. These assumptions are designed to model an idealized version of a solar cell under optimal conditions. The key assumptions are as follows:

-Photon absorption and electron-hole generation: It is assumed that each absorbed photon generates exactly one electron-hole pair. This assumption disregards the possibility of multiple exciton generation or any other mechanisms that might lead to the creation of more than one charge carrier from a single photon.

-Photon energy and bandgap: Only photons with energy equal to or greater than the semiconductor's bandgap are absorbed by the material. Photons with energy lower than the bandgap cannot be absorbed, as they lack the energy required to excite an electron from the

valence band to the conduction band. This simplifies the absorption process by neglecting any sub-bandgap absorption or photon upconversion mechanisms.
-Radiative recombination: The only recombination process considered within the cell is radiative recombination, where an electron and a hole recombine and release energy in the form of a photon. Non-radiative recombination processes, such as those described by the SRH model or Auger recombination, which involve energy loss without photon emission, are neglected. These processes are generally responsible for reducing the efficiency of real-world solar cells but are omitted in the ideal model to simplify the analysis.
-Zero resistive losses: In the ideal solar cell model, it is assumed that there are no resistive losses, either in the bulk of the material or in the contacts. This means that there is no energy lost due to the resistance of the semiconductor or the electrodes, which in real-world devices would reduce overall efficiency.
-Ambient temperature: The model assumes that the solar cell operates at a temperature of 300 K, which is the typical temperature for a cell under standard conditions. This assumption is important because the temperature affects the efficiency of the cell, particularly in terms of the carrier mobility, recombination rates, and the voltage generated by the cell.
These assumptions, while simplifying the real-world complexities of solar cell operation, provide a clear theoretical framework for understanding the maximum possible efficiency of a solar cell, based on the fundamental principles of energy conservation and charge transport. The Shockley-Queisser model serves as a reference point for evaluating the performance of different solar cell technologies and understanding the limitations imposed by the laws of physics.
The history of solar cells can be divided into three main generations, each characterized by the use of different absorber materials that convert solar energy into electricity. Each generation represents a significant step forward in the evolution of photovoltaic technology, aiming to improve efficiency, reduce costs, and minimize environmental impact.

1.3.2 Evolution of Solar Cell Technologies: Advancements in Absorber Materials

The history of solar cells can be divided into three main generations, each characterized by the use of different absorber materials that convert solar energy into electricity. Each generation represents a significant step forward in the evolution of photovoltaic technology, aiming to improve efficiency, reduce costs, and minimize environmental impact.
The **first generation** of solar cells is dominated by crystalline silicon (c-Si) as the primary absorber material, which remains the oldest, most widely used, and solar cell technology. These cells are based on thin silicon wafers, known as monocrystalline solar cells, which utilize high-purity silicon to absorb sunlight and generate electricity. The commercial production of c-Si modules began in 1963, when Sharp Corporation in Japan pioneered the manufacturing of PV modules and installed a 242-Watt PV system (Green, 2001).
Monocrystalline solar cells stand out for their higher efficiency compared to other solar PV technologies, achieving values of up to 26% [10]. This means they can generate more electricity from a given panel area, making them a preferred choice where space efficiency is a priority. The silicon wafers used in these cells are produced through the Czochralski process, a method also widely applied in silicon-based electronics to ensure the high purity required for optimal performance.
Silicon solar cells typically have two layers: a positive layer (p-type) and a negative layer (n-type). The positive layer is usually made by doping silicon with boron to create extra holes in

the silicon lattice, while the negative layer is formed by doping silicon with phosphorus to introduce additional electrons [11]. Despite their efficiency, monocrystalline cells currently represent only about 30% of the market. This is largely due to their higher production costs, driven by the energy-intensive and complex purification process needed to produce high-quality silicon.

In response to these limitations, the **second generation** of solar cells emerged, utilizing thin-film materials as absorbers. These materials are significantly thinner than crystalline silicon, allowing for a substantial reduction in the amount of material required for production. Common absorber materials for thin-film cells include cadmium telluride (CdTe) and copper indium gallium selenide (CIGS).

A key difference between second-generation and first-generation solar cells lies in the semiconductor material: thin-film cells use materials with a direct band gap, unlike the indirect band gap of silicon. This allows for more efficient absorption of sunlight at lower material thicknesses, although the cells still rely on a p-n junction design.

Thin-film solar cells offer several advantages, including lower manufacturing costs, greater flexibility, and reduced environmental impact. However, these benefits come at the expense of lower efficiency compared to crystalline silicon-based cells.

Due to high costs of first-generation solar cells and toxicity and limited availability of materials for second generation solar cells, a new generation of solar cells emerged.

The **third generation** of solar cells is focused on emerging materials and advanced technologies to overcome the efficiency and cost limitations of earlier generations. are inherently different from the previous two generations because they do not rely on the p-n junction design of the others.

New absorber materials, such as organic semiconductors, perovskites, and other novel materials, show great promise for reducing production costs further while enabling flexible and transparent solar cells for various applications. Their implementation with thin film technologies could have a huge impact economically, making solar energy one of the most accessible and cheapest options for future energy production. Thin-film technologies have the benefit of a tunable bandgap, making them a better option for light harvesting [12]. Additionally, this generation is exploring design innovations such as multi-junction cells and concentrating on photovoltaics to enhance efficiency.

1.4 Metal Halide Perovskites.

Metal halide perovskites (MHPs) have revolutionized photovoltaic research, offering a unique combination of tunable optoelectronic properties and straightforward fabrication processes. A key advantage of these materials lies in their exceptional carrier diffusion length, which can extend over micrometer scales, enabling efficient charge transport even in thin-film architectures. This property, coupled with their high absorption coefficient and ambipolar charge transport capabilities, allows hybrid perovskites to achieve high power conversion efficiencies while maintaining relatively simple device structures [13,14].

Their unique chemical structure, characterized by a perovskite lattice that can accommodate a wide variety of organic and inorganic components, enables fine-tuning of their optoelectronic properties. This adaptability allows for the development of materials optimized for specific applications, from highly efficient single-junction solar cells to advanced tandem devices.

One of the most significant areas of exploration in perovskite research involves varying the composition of the lattice to balance performance, stability, and environmental impact. Hybrid structures, which combine organic and inorganic components, have demonstrated exceptional efficiency and ease of processing, while all-inorganic perovskites, with their robust thermal and environmental stability, are increasingly being developed for applications in extreme operating conditions.

1.4.1 Structural Properties and Adaptability of MHPs.

Understanding the structural properties of MHPs is crucial for optimizing their performance, as their crystalline adaptability allows for tuning the physicochemical characteristics to meet specific application needs. Structurally, the light harvesting material in the PSCs is a crystalline material with a flexible inorganic framework that can incorporate organic components, forming a three-dimensional lattice with the general formula ABX_3 *Figure 1.8a*. In this lattice, the A site is occupied by a monovalent organic or inorganic cation (e.g., methylammonium (MA) $CH_3NH_3^+$, formamidinium (FA) $CH(NH_2)_2^+$, or Cs^+), the B site hosts a divalent metal cation (e.g., Pb^{2+}, Sn^{2+}), and the X site is occupied by a halide anion (e.g., I^-, Br^-, Cl^-) [15]. This highly adaptable framework enables fine-tuning of structural and electronic properties for specific applications, which is essential for achieving high performance in devices like solar cells.

The crystal structure of perovskite adopts a face-centered cubic $Pm\bar{3}m$ arrangement, where A (Wyckoff position 1a) is coordinated to 12 X (3c) anions, B (1b) is bonded to six X anions, and BX_6 octahedra are corner-connected to form a three-dimensional framework. The structural adaptability of the lattice is further enhanced by the hinged nature of the BX_6 octahedra, which allows for wide adjustments in the B–X–B bond angle. Several cooperative rotations, known as tilt transitions, promote symmetry reduction from the cubic aristotype. This adaptability is quantified using Goldschmidt tolerance factor (t) is a reliable empirical index to predict which structure is preferentially formed. The Goldschmidt tolerance factor is calculated from the ionic radius of the atoms according with equation 1.6:

$$t = \frac{r_A + r_X}{\sqrt{2}(r_B + r_X)} \tag{1.6}$$

where r_A is the ionic radius of the A-site cation, r_B is the radius of the B-site cation, and r_X is the radius of the X-site anion. The Goldschmidt tolerance factor indicates the degree to which the crystal lattice can accommodate the ions without distortion. Assuming that the organic molecule is free to rotate around its center of mass, its effective ionic radius r_A can be calculated as discussed by Kieslich et al. [16], following the relation $r_A = r_{mass} + r_{ion}$ (r_{mass} is the distance between the center of mass and the most distant atom of the molecule, with r_{ion} its corresponding ionic radius). When the value of t is close to 1 (typically between 0.8 and 1), the crystal structure tends to be stable, and the material adopts a regular, three-dimensional perovskite structure. In this stable configuration, the BX_6 octahedra are aligned in a way that supports optimal charge transport and electronic properties. However, if t deviates significantly from 1 (either lower or higher), the crystal structure becomes unstable, leading to distortions such as tilted or distorted octahedra [17,18,19]. Two scenarios are notable:

- $(r_A + r_X) > \sqrt{2}(r_B + r_X)$ (tolerance factor > 1): this leads to a tendency toward tetragonal elongation.

- $(r_A + r_X) < \sqrt{2}(r_B + r_X)$ (tolerance factor < 1): this results in the buckling of the octahedra.

These distortions can affect the electronic properties of the material, such as its band gap, charge carrier mobility, and overall photovoltaic performance. In some cases, these structural distortions may even lead to the formation of alternative crystal structures, which could have different electronic characteristics, potentially impacting the efficiency of perovskite-based devices. The relationship between the perovskite structure and the tolerance factor, along with its implications for material properties, is illustrated schematically in *Figure 1.8b*.

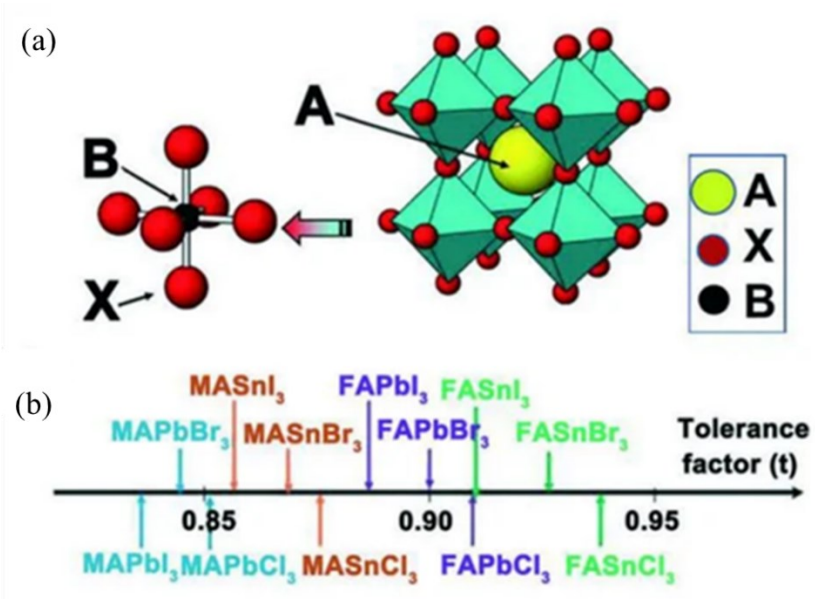

Figure 1.8 (a) Unit cell of ABX_3 with octahedral structure; (b) the tolerance factor of different crystal structures [20].

A perovskite material with a specific chemical composition often exhibits multiple structural forms, influenced by temperature and preparation methods. For simplicity, we refer to the cubic structure as the α-phase and the non-perovskite structures (t>1) as the δ-phase. The structural flexibility also plays a significant role in choosing the B-site cation, where group 14 elements like Pb^{2+} and Sn^{2+} are often preferred due to their stereochemically active s^2 lone pairs. Their larger ionic radii and higher polarizability enhance charge transfer and overlap with halide orbitals, optimizing the bandgap for photovoltaic applications. Pb^{2+} offers superior stability and conductivity but is toxic, while Sn^{2+} provides an eco-friendlier alternative, albeit with reduced stability due to oxidation ($Sn^{2+} \rightarrow Sn^{4+}$). Ge^{2+} is less effective due to weaker lone pair activity and a wider bandgap. The A-site component in MHPs primarily serves as a counterion for charge balance and physical stabilization, but its impact on octahedral orientation and dimensionality significantly affects the electronic structure. In fact, the following sections examine the key properties, advantages, and challenges of perovskite materials for PV, where A is organic or inorganic.

1.4.2. Organic-Inorganic Perovskites.

The prototypical MHPs are methylammonium lead iodide ($MAPbI_3$) and formamidinium lead iodide ($FAPbI_3$), which feature optical band gaps nearly optimal for solar absorption. affects the electronic structure. The synthesis of $MAPbI_3$ was first described by Weber, who reported its cubic perovskite structure (space group $Pm\bar{3}m$, Z = 1) at high temperature. In this cubic phase,

the unit cell contains only one formula unit, and the non-centrosymmetric methylammonium $(CH_3NH_3)^+$ ions, which exhibit C_{3v} symmetry, must be orientationally disordered to comply with the O_h symmetry of the structure. This disorder means that the methylammonium cation is statistically distributed over eight equivalent positions (x, x, x). In these positions, the carbon and nitrogen atoms are randomly arranged within the eight tetrahedral interstices of the A-site cuboctahedra of the perovskite aristotype, resulting in a 24 disordered state [21]. At 327.4 K, $MAPbI_3$ undergoes a phase transition from cubic ($Pm\bar{3}m$) to tetragonal (I4/mcm), reducing the orientational disorder of the $(CH_3NH_3)^+$ ions to eight distinct configurations. A second transition occurs at 162.2 K, producing an orthorhombic phase ($Pmc2_1$), where the methylammonium cations are immobilized, eliminating dynamic disorder.

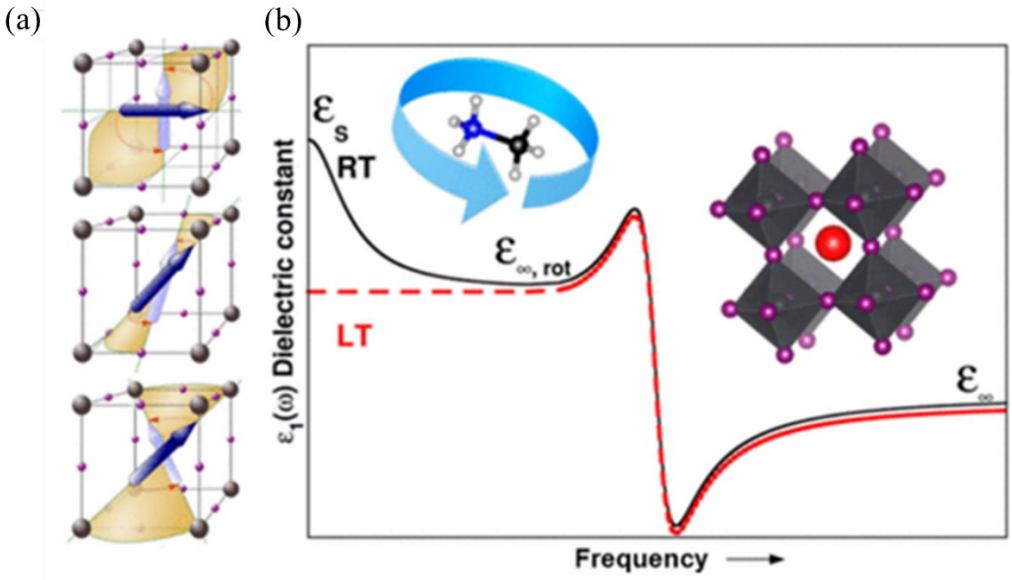

Figure 1.9 (a) High probability tumbling modes of $CH_3NH_3^+$ in the room temperature tetragonal and high temperature cubic phases of $CH_3NH_3PbI_3$. Conical reorientation pathways determined using quasi-elastic neutron scattering are along the faces (top), edges (middle), and corners (bottom) [23] (b)Schematic drawing of the dielectric constant as a function of frequency displaying respective contributions of $CH_3NH_3^+$ rotations and perovskite's vibrational phonons [22].

The dynamic disorder depending of $CH_3NH_3^+$ is linked to its structural asymmetry and significant permanent dipole moment (2.3 D). Extensive experimental and computational studies conducted over the past three decades have demonstrated that these molecular cations interact with the inorganic framework primarily through electrostatic forces and, to a lesser extent, hydrogen bonding. In high-temperature phases, $CH_3NH_3^+$ exhibits dynamic reorientations, including rotations around the C–N axis and tumbling motions. Several possible tumbling modes have been identified (illustrated in *Figure 1.9a*). In contrast, at low temperatures in the orthorhombic phase, $CH_3NH_3^+$ reorientation is suppressed, and dynamic disorder is absent.

The rotational freedom of dipoles in the perovskite structure allows molecular cations to dynamically respond to external perturbations, significantly affecting dielectric properties. $CH_3NH_3PbI_3$ exhibits distinct behavior across temperatures. In the low-temperature (LT) orthorhombic phase and room-temperature (RT) tetragonal phase, the real part of the dielectric function, $\varepsilon(\omega) = \varepsilon_1(\omega) + i\varepsilon_2(\omega)$, reflects the material's polarizability. where $\varepsilon_1(\omega)$ is related to

polarizability of the medium in response to an oscillating electric field. Because polarization is frequency-dependent, it is convenient to discuss limiting cases known as the static $\varepsilon_s = \lim_{\omega \to 0} \varepsilon_1(\omega)$ and high-frequency or optical [$\varepsilon_\infty = \varepsilon_1(\sim 10^{15}$ Hz)] dielectric constants. ε_s is associated with coupling of all polarizable elements within the lattice (dipoles, ions, and electrons), while only electronic perturbations contribute to ε_∞. For scale in *Figure 1.9b*, the plateau of ε_∞ in $CH_3NH_3PbI_3$ is 6.5 and ε_s is 36 at LT (20 K) and 62 at RT. In the high frequency limit, the main contributions to ε_1 are vibrational polar phonon modes within the inorganic lattice, thus ε_∞ is comparable in the RT tetragonal and low-temperature orthorhombic phases. However, in the static limit there is a large deviation in the response, with the tetragonal phase increasing rapidly in the vicinity of ε_s [22]. Even et al. [23] attribute this large discrepancy to rotational motion of $CH_3NH_3^+$. This same mechanism does not come into play in the orthorhombic phase where molecular cations are unable to reorient. The dielectric constant has important implications for Coulombic interactions between electrons and holes.

By contrast, recent studies of lead halide perovskites with formamidinium (FA) as an A-site cation demonstrated a high degree of orientational disorder of the FA cation within the inorganic framework, even at cryogenic temperatures. The FA cation is larger than MA, which may restrict its rotational motion by steric interactions. It also has an almost negligible dipole moment, and it contains two nitrogen positions including hydrogens that can form hydrogen bonds with the lead iodide cage. $FAPbI_3$ exhibits a high-temperature cubic perovskite structure and a low-temperature structure with octahedral tilting [24]. Carignano et al. have performed *ab initio* molecular dynamics simulations on $FAPbI_3$ and reported that at high temperatures there are preferential alignments of the FA ion due to hydrogen bonds with the cage [25]. They also concluded that FA rotates preferentially around the N–N axis, which has later been supported by other studies. The stable structure of $FAPbI_3$ at room temperature is a nonperovskite hexagonal structure (δ-phase, $P6_3/mmc$), but a metastable cubic (α) perovskite phase ($Pm\bar{3}m$) can be stabilized at room temperature for several days by heating to above the δ−α phase transition at around 410 K. Upon cooling the α-phase, the structure transforms to a tetragonal (β) phase ($P4/mbm$) for 140 K $\lesssim T \lesssim$ 285 K and to yet another tetragonal (γ) phase for $T \lesssim$ 140 K. $FAPbI_3$ exhibits similar behavior to $MAPbI_3$, but with important differences. In the FA cation, which is less dipolar and lacks significant dipole-dipole interactions, it is the specific interactions with Pb and I ions, as well as steric forces, that influence the formation of ordered domains. Furthermore, the rotation dynamics of the FA cation are slower than those of MA, due to steric interactions and hydrogen bonding with the Pb–I cage [24].

Within a given dimensionality, optical response is most readily modified through substitutions of the halide component, which primarily alters the VB position influencing the material's optical and electronic properties. The X-site typically refers to the halide anion (such as iodine (I), bromine (Br), or chlorine (Cl), and substituting one halide with another can lead to significant changes in the bandgap. For example, replacing iodine (I) with bromine (Br) in a lead halide perovskite increases the bandgap, shifting the absorption edge towards higher energies (shorter wavelengths), which can optimize the material for certain applications.

Mixed halide perovskites, $ABX_{3-x}X'_x$, where x indicates the halide content of the perovskite where two or more halides are combined at the X-site, offer even greater flexibility in tuning the bandgap. Pioneering work suggested that perovskite films exhibit composition-structure dependent properties, which can be accessed by various processing approaches. Noh et al.,

[26] demonstrated that the chemical modification of $MAPbI_3$ through the substitution of iodide with bromide enables effective bandgap tuning across a wide range, from 1.5 eV to 2.3 eV. This tunability was further confirmed through UV–visible absorption spectra (*Figure 1.10a*) of $MAPb(I_{1-x}Br_x)_3$ ($0 \leq x \leq 1$), which revealed a systematic shift in the absorption edge from 786 nm (1.58 eV) for $MAPbI_3$ to 544 nm (2.28 eV) for $MAPb(I_{1-x}Br_x)_3$. This shift not only highlights the flexibility in bandgap engineering but also enables precise control over the material's color, transitioning from dark brown for $MAPbI_3$ to red and eventually to yellow with increasing bromide content as shown in *Figure 1.10b*. Such compositional tuning, described by a quadratic relationship between bandgap and halide composition, underscores the potential of mixed-halide perovskites for tailoring optical and electronic properties to meet the demands of diverse photovoltaic and optoelectronic applications, including colorful solar cells (*Figure 1.10c*).

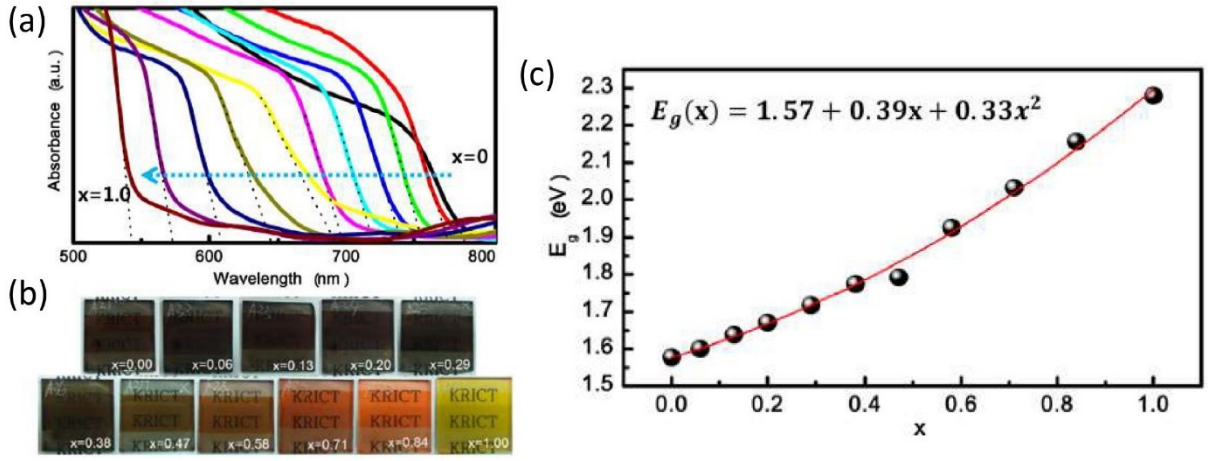

Figure 1.10 Photographs and UV−vis absorption spectra of $MAPb(I_{1-x}Br_x)_3$. (a) UV−vis absorption spectra of FTO/bl-TiO_2/mp-TiO_2/ $MAPb(I_{1-x}Br_x)_3$/Au cells measured using an integral sphere. (b) Photographs of 3D TiO_2/ $MAPb(I_{1-x}Br_x)_3$ bilayer nanocomposites on FTO glass substrates. (c) A quadratic relationship of the band-gaps of $MAPb(I_{1-x}Br_x)_3$ as a function of Br composition (x) [26].

The diffusion length in the mixed halide perovskite are >1 mm with the factor of ~5 to 10 greater than the absorption depth. In contrast, the diffusion lengths in the triiodide perovskite are only on the order of, or slightly shorter, than the absorption depth (~100 nm). The larger diffusion length in the mixed halide perovskite results from a much longer recombination lifetime and is consistent with far superior performance in planar heterojunction solar cells has been reported by Stranks et al. for $MAPb(I_{1-x}Cl_x)_3$ [27]. Lahoucine Atourki et al. [28] demonstrated that the substitution of I ions with Br ions in $MAPb(I_{1-x}Br_x)_3$ induces a change to the perovskite phase from tetragonal to cubic compared with that of the pure $MAPbI_3$ material. *Figure 1.11* shows the X-Ray diffraction (XRD) patterns of $MAPb(I_{1-x}Br_x)_3$ with different bromide fractions. As the bromide content is increased, the diffraction profiles are shifted towards higher angles, resulting from the decrease of lattice spacing due to the partial substitution of the larger iodine atom (ionic radius 2.2Å) with a smaller Br atom (ionic radius 1.96Å). For instance, the pure $MAPbI_3$ exhibits a tetragonal phase with characteristic diffraction peaks, such as the one at 23.46° associated with the (2 1 1) planes. However, upon increasing

the substitution level (x), particularly when x = 0.4 or higher, the material shifts to a cubic phase with a space group $Pm\bar{3}m$, like that of $MAPbBr_3$, increasing the thermal stability.

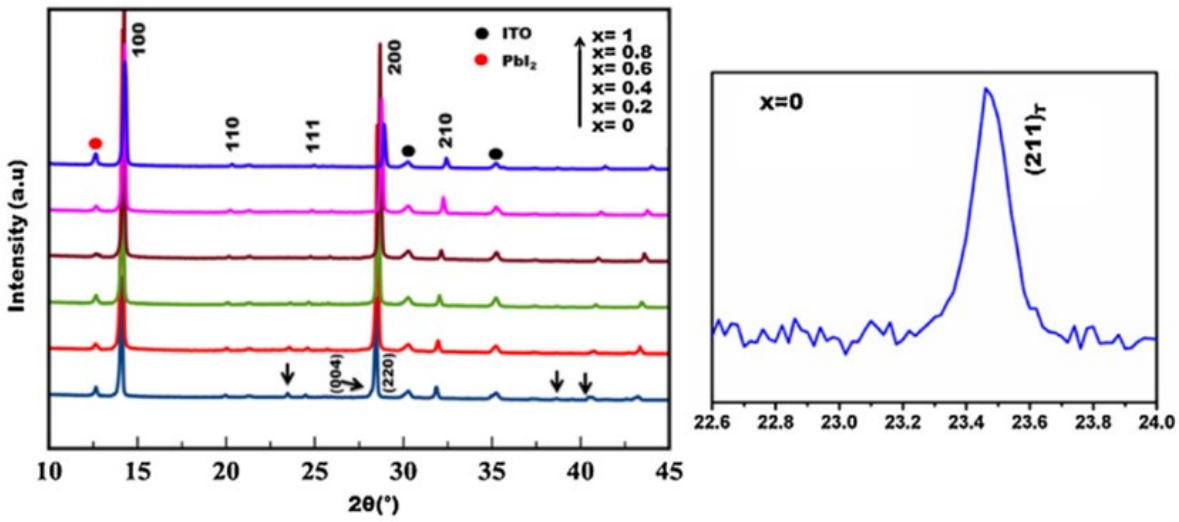

Figure 1.11 XRD of $MAPb(I_{1-x}Br_x)_3$ (x = 0, 0.2, 0.4, 0.6, 0.8, 1.0) perovskites thin films [28].

Chiang et al. fabricated a high quality mixed-halide $MAPb(I/Br/Cl)_3$ perovskite films, suggested that the presence of Br can increase the V_{oc} values and improve device stability while Cl positively impacted the film morphology as well as the charge transport processes. $MAPbBr_3$ has higher LUMO and lower HOMO energy level than $MAPbI_3$. Therefore solar cell based on $MAPbBr_3$ (or $MAPb(I_{1-x}Br_x)_3$) exhibit higher open-circuit voltage [29].

1.5 Issues of Hybrid Halide Perovskites.

Stability has been identified as a significant challenge for perovskite materials and, consequently, for PSCs. In evaluating the stability of these materials and devices, it is essential to consider the effects of temperature, illumination, and exposure to ambient factors such as oxygen and moisture. Among these, moisture plays a critical role in accelerating degradation, although it does not directly react with perovskite. Instead, it acts as a catalyst for the chemical reactions responsible for degradation.

Niu et al. investigated these processes and, based XRD patterns, proposed a series of reactions that involve the formation of hydrogen gas (H_2), which escapes from the system and hinders the reversibility of the degradation reactions [30]. The specific reactions involved in the degradation of the perovskite layer in the presence of water are illustrated in Equations (1.7)-(1.10).

$$CH_3NH_3PbI_3(s) \leftrightarrow PbI_2(s) + CH_3NH_3I(aq) \quad (1.7)$$

$$CH_3NH_3I(aq) \leftrightarrow CH_3NH_2(aq) + HI(aq) \quad (1.8)$$

$$4HI(aq) + O_2(g) \leftrightarrow 2I_2(s) + 2H_2O\ (l) \quad (1.9)$$

$$2HI(aq) \leftrightarrow H_2(g) + I_2 \quad (1.10)$$

Yang et al. further explored the impact of relative humidity (RH) on perovskite degradation using in situ absorption spectroscopy and grazing-incidence XRD [31]. Their work documented the gradual phase changes occurring under varying RH levels and analyzed the corresponding

decline in the PCE. Their findings indicated that PSCs remain relatively stable at RH levels up to 50%. However, at higher RH levels of 80% and 98%, degradation accelerated significantly. Under these conditions, the absorbance of the perovskite dropped to just 20% of its initial value within the first 20 hours of operation, highlighting the critical impact of moisture on device performance.

In addition, the ingress of oxygen in the perovskite layer can induce the degradation of the perovskite material by photo-oxidation. While oxygen alone can only slightly degrade the device, the degradation is more severe in illuminated conditions. In photo-oxidation, iodide ions from I_2 in the presence of light also forms H_2 in the process. The subsequent degradation effect of this reaction is twofold. H_2 tends to escape the device, and I_2 reacts with the back electrode to form metal iodides. In addition, Pb^{2+} is oxidized to Pb^{4+} ions by photo-oxidation, forming a layer of PbO_2 on the surface of perovskite. It has been reported that the devices do not show any considerable oxidation when kept in the dark under a wet atmosphere. However, in the presence of light, oxygen seems to have an unavoidable effect on the stability of the devices [32].

Degradation of perovskite upon exposure to UV light is predominantly caused by chemical reactions at the $TiO_2/CH_3NH_3PbI_3$ interface. TiO_2, which is the commonly used ETL in PSCs, has a suitable bandgap of 3.2 eV. However, TiO_2 acts as a photocatalyst to oxidize water and organic materials in both mesoporous and planar forms. Possible chemical reactions involving the degradation of perovskite are shown in Equation (1.11) -(1.13).

$$2I^- \leftrightarrow I_2 + 2e^- \quad (1.11)$$

$$3CH_3NH_3^+ \leftrightarrow 3CH_3NH_2 + 3H^+ \quad (1.12)$$

$$I^- + I_2 + 3H^+ + 2e^- \leftrightarrow 3HI \quad (1.13)$$

Here, the TiO_2 interface is involved in the formation of I_2 from iodide ions by oxidation. The second reaction should shift to the left (reactant) side due to reaction kinetics. However, the evaporation of methyl anime and reaction of H^+ to form HI (which also evaporates) causes the second reaction to proceed to the right side and causes degradation of methylamine [31].

High temperature also accelerates the breakdown of the perovskite layer and causes performance degradation as a result. Degradation at elevated temperatures is related to the change of the phase of perovskite.

Furthermore, reactive oxygen species (ROS) have emerged as critical mediators in the degradation pathways of perovskite materials. The ROS-induced reactions lead to structural damage, breaking down the perovskite lattice and increasing the density of defect states, which further amplifies recombination losses and device instability. A possible pathway of degradation reported in literature for $MAPbI_3$, supposed that neutral oxygen absorbs on the surface of the perovskite (preferably at iodide vacancies) in unoccupied adsorption sites (*) and then gets reduced by photoexcited electrons to form superoxide radicals ($O_2^{\bullet -*}$). Furthermore, $O_2^{\bullet -*}$ can abstract protons from methylammonium cations (MA^+), yielding adsorbed hydroperoxyl radicals ($O_2^{\bullet -*} + H^+ \rightarrow HO_2^{\bullet *}$). Once this species is present, other ROS may form, including H_2O_2, $OH^\bullet$, and OH^-. Each ROS may react with MA^+, abstracting either a proton or a neutral hydrogen [33]. A plausible complete pathway is as follows:

$$h\nu \rightarrow e^- + h^+ \quad (1.14)$$

$$O_2 + [*] \rightarrow O_2* \quad (1.15)$$
$$O_2* + e^- \rightarrow O_2^{\bullet -*} \quad (1.16)$$
$$CH_3NH_3PbI_3 + O_2^{\bullet -*} \rightarrow HO_2^{\bullet *} + PbI_2 + CH_3NH_2 + I^- \quad (1.17)$$
$$HO_2^{\bullet *} \rightarrow 1/2\ H_2 + O_2 + [*] \quad (1.18)$$
$$h^+ + CH_3NH_3PbI_3 \rightarrow CH_3NH_3PbI_2^+ + [*] + I^{\bullet} \quad (1.19)$$
$$CH_3NH_3PbI_2^+ + [*] + I^- \rightarrow CH_3NH_3PbI_3 \quad (1.20)$$
$$I^{\bullet} \rightarrow 1/2\ I_2 \quad (1.21)$$

There are multiple ways that this reaction can proceed from step 1.17 onward, depending on the rates at which different ROS and the specific products form. However, all variations result in the same ratelaw that is sublinear in oxygen and concentration of electrons, provided that step 1.17 (proton abstraction from MA + by $O_2^{\bullet -}$) is the rate-determining step. Notably, without illumination, these degradation processes proceed much more slowly, underscoring the critical role of light in driving ROS formation and accelerating material breakdown.

In addition to the degradation pathways driven by ROS, the stability of perovskite materials is further compromised by the phenomenon of phase segregation. This issue is particularly pronounced in mixed-halide perovskites, where external stressors such as light exposure and thermal effects induce the spontaneous demixing of halide ions. In this phenomenon different halide ions (e.g., iodide and bromide) separate under photoexcitation [34]. This results in a heterogeneous distribution of compositions and local bandgaps, which undermines the uniformity of optoelectronic properties. This phase segregation compromises device performance and stability by inducing regions with varying light absorption and charge transport characteristics, posing a significant hurdle for practical applications. Since the valence band of $MAPb(I_{1-x}Br_x)_3$ is dominated by the contribution of halide p orbitals [35], specifically the hybridization of Br 4p orbitals with I 5p and Pb 6s orbitals, as well as the crystal structure transition from tetragonal to pseudocubic [36]. The formation of iodide-enriched domains can stabilize holes, potentially providing the driving enthalpy for halide segregation under short-term light illumination (*Figure 1.12a*). When these trapped holes are filled, entropy and lattice strain can cause the phase-segregated material to relax back to a well-mixed state. This light-induced, reversible structural change has been attributed to the self-trapping of photogenerated holes in $PbBr_2$. Additionally, the presence of iodide-rich domains, which have a smaller bandgap, lowers the energy of excitons and could further drive halide segregation. The structural and spectroscopic changes observed under photoexcitation suggest that photogenerated excited states play an important role in the transformation mechanism. It is not yet clear whether electrical excitation can induce similar changes. Yang et al. [34] demonstrated that the light-induced modification of optical properties is reversible after dark storage for hours at room temperature, suggesting a two-step process where sub-bandgap states are first photogenerated and, if exposed to more photons, lead to light-induced metastable states that cause a red-shift in photoluminescence (PL). This instability reduces the bandgap and creates additional traps that degrade device performance. Hoke et al. [37] observed the formation of a new low-energy PL feature upon light soaking of $MAPb(I_{1-x}Br_x)_3$ and other mixed-halide perovskites (*Figure 1.12b*). This spectral change is consistent with photo-induced halide segregation. In the case of $MAPb(I_{1-x}Br_x)_3$ solar cells, the red-shift in PL upon light illumination indicates a reduction in the electronic bandgap and quasi-Fermi level splitting, reducing their achievable V_{OC}'s. Huang et al. [38] examined $MAPb(I_{1-x}Br_x)_3$ stability under prolonged

illumination. It was found that with prolonged exposure, electric fields generated in the I-rich domains cause significant structural deformation and eventually lead to the breaking of Pb–I bonds. Bond breaking and the loss of N-containing ions, I-rich domains decompose into PbI_2 and Br-rich perovskite regions. The decomposition leads to irreversible morphological and absorption band edge changes, demonstrating that phase segregation is not completely reversible for long time illumination.

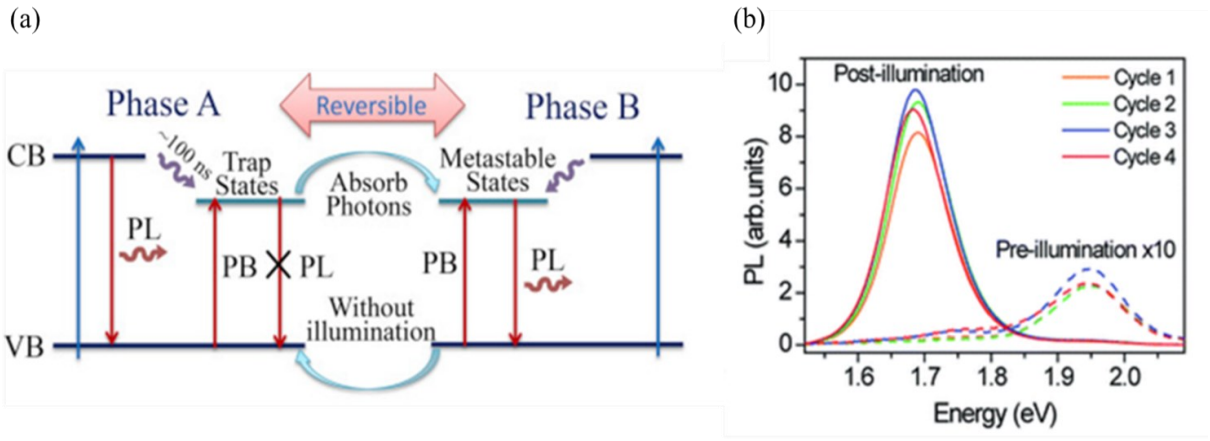

Figure 1.12 (a) Schematic of the proposed mechanism for photo-induced trap formation through halide segregation [34]. Photogenerated holes or excitons may stabilize the formation of iodide-enriched domains which then dominate the photoluminescence. (b) PL spectra of $MAPb(I_{1-x}Br_x)_3$ thin film after sequential cycles of illumination for 2 minutes (457 nm, 15 mW cm^{-2}) followed by 5 minutes in the dark [36].

1.6 Full Inorganic Perovskites.

Cesium lead trihalide ($CsPbX_3$) perovskite has garnered significant attention as a promising alternative to the organic-inorganic halide counterparts, based on MA^+ and FA^+ cations, in PSCs. All-inorganic perovskites, particularly $CsPbX_3$-based solar cells, demonstrate improved stability and possess a tunable optical bandgap ranging from 1.6 to 3.0 eV by varying the halogen composition. This tunability enables precise light management, making them well-suited for indoor applications [39] and for use as sub-cells in perovskite-silicon and perovskite tandem PSCs [40,41]. These configurations hold substantial potential for exceeding the S-Q limit of single-junction solar cells, thereby achieving higher PCE, which is a critical aspect for advancing solar technology (*Figure 1.13*).

Among the all-inorganic perovskites, $CsPbI_3$ stands out due to its narrow bandgap (E_g = 1.6-1.7 eV), making it an excellent candidate for solar energy harvesting. $CsPbI_3$ is one of the earliest known ternaries plumbohalides, originally discovered by Møller [43], and is characterized by adopting a distinct "perovskitoid" structure, unlike its well-known analogs $CsPbBr_3$ and $CsPbCl_3$, which crystallize in a regular perovskite structure. However, its black phase (α-$CsPbI_3$), which is essential for optimal performance, suffers from poor stability at RT, rapidly transforming into a non-perovskite yellow phase (δ-$CsPbI_3$).

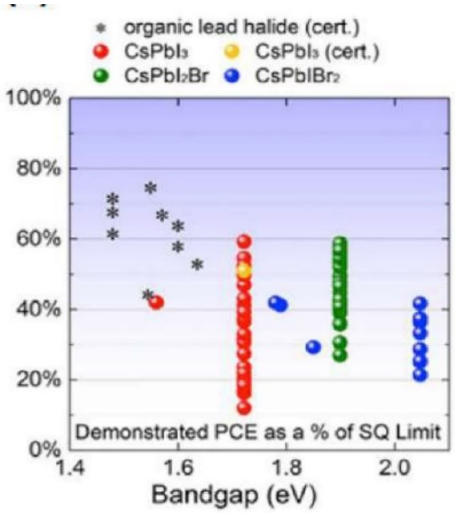

Figure 1.13 Demonstrated efficiencies of state-of-the-art organic and reported inorganic perovskite solar cells as a percentage of S-Q limits [42].

This phase instability remains a major obstacle to achieving higher efficiency and broader application of $CsPbI_3$-based solar cells [42]. The black α-phase, with a $Pm\bar{3}m$ space group, is stable only at temperatures above 645 K. Arthur Marronnier et al. [44] demonstrated that $CsPbI_3$ can temporarily retain its metastable perovskite structure at RT after being cooled from high temperatures.

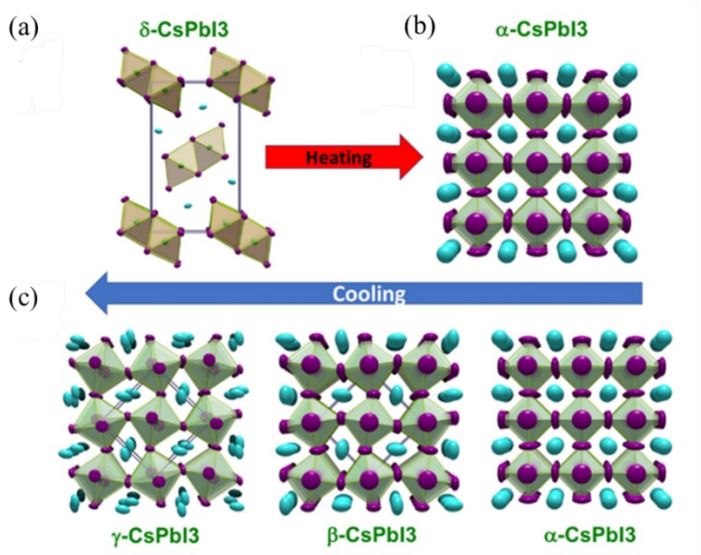

Figure 1.14 Structural phase transitions in $CsPbI_3$ versus temperature.(a) Initial yellow perovskitoid phase (δ-$CsPbI_3$)converts to (b) black perovskite phase (α-$CsPbI_3$) as the temperature exceeds the transition temperature. (c) Uponcooling, the black perovskite phase is retained and can be undercooled below the transition temperature, where the typical perovskite distortions (tetragonal β-$CsPbI_3$, orthorhombic γ-$CsPbI_3$) can be observed all the way to room temperature. These phases are metastable and transform to the thermodynamic δ-$CsPbI_3$ upon standing [44].

Using high-resolution synchrotron XRD, they showed that upon heating, $CsPbI_3$ transitions from the yellow δ-phase to the black α-phase. Upon cooling, however, it does not immediately revert to the δ-phase. Instead, the cubic α-phase first distorts into a tetragonal β-phase (P4/mbm) at 510 K, and then transforms into an orthorhombic γ-phase (Pbnm) at 325 K, which remains stable at RT (*Figure 1.14*).

The undesirable phase transition occurs because the Cs^+ cation is relatively too small to hold the framework of share-cornered lead-halide octahedra and t is outside the ideal range between 0.9 and 1, and therefore the perovskite structure is prone to distortion. The structural phases of $CsPbI_3$ are associated with distinct energy gaps, each influencing its optical and electronic properties. The yellow δ-$CsPbI_3$ phase, stable at room temperature, exhibits a wide energy gap (~2.82 eV), typically unsuitable for photovoltaic applications. In contrast, the black phases (α-, β- and γ-), feature an optimal direct band gap: α-$CsPbI_3$ ~1.62 eV, the γ- $CsPbI_3$ exhibits a slightly narrower band gap (~1,68 eV) compared to the β- $CsPbI_3$ (~1.72eV) due to increased structural distortions, which influence the electronic states [45]. The formation of energy (E_f) is a key parameter for evaluating the relative stability of materials. For $CsPbI_3$, as shown in Equation 1.22:

$$E_f = E(CsPbI_3) - E(CsI) - E(PbI_2) \quad (1.22)$$

as calculated by Sutton et al. [46], the trend $E_f(\alpha) > 0 \geq E_f(\beta) > E_f(\gamma) > E_f(\delta)$, indicating that the yellow δ-phase, with the lowest E_f, is the most thermodynamically stable phase at RT. This conclusion aligns with experimental observations, which show that the δ-phase is preferred under ambient conditions. In contrast, the α-phase has an endothermic formation process, making it metastable and prone to transition to other, more energetically favorable phases. Among the black photoactive polymorphs, the orthorhombic γ-phase is thermodynamically the most stable due to its exothermic formation energy. Studies combining room-temperature solution calorimetry and differential scanning calorimetry revealed the formation enthalpies (ΔH) for the α- and δ-phases of $CsPbI_3$ $\Delta H\alpha = -2.83 \pm 0.90$ and $\Delta H\delta = -16.93 \pm 0.87$ kJ/mol. The phase transition from δ to α is associated with an enthalpy change of 14.10±0.24 kJ/mol and an entropy change of 23.78 J/(mol·K). These values confirm the metastable nature of the α-phase at standard environmental conditions, primarily due to its high vibrational entropy.

1.7 Perovskite Solar Cells (PSCs).

1.7.1 Devices architectures.

Since 2009, the PCE of PSCs has increased from approximately 3.8% to nearly 27%, approaching the S–Q limit (33.7% at 1 sun) [47]. The performance of perovskite solar cells is heavily reliant on their architecture, which in turn influences the choice of materials, deposition techniques, and the compatibility between the device's components. To date, two main types of architectures have been developed for perovskite solar cells: mesoscopic and planar structures. In the mesoscopic architecture, the perovskite may be deposited as a thin layer that adequately covers the oxide scaffold, with the pores of the scaffold filled with a charge-transporting material, or it may form an additional layer on top of the fully infiltrated oxide scaffold (*Figure 1.15a*). The mesoporous structure is conventionally used using mesoporous TiO_2, which is sensitized by the perovskite upon exposure to light. Mesoporous TiO_2 is coated on top of planar TiO_2, and it acts as a scaffold for the growth of perovskite [48]. In contrast, the planar heterojunction architecture (PHJ) is simpler and can be designed in either a conventional configuration or an inverted configuration, depending on the direction of the electric current [49] (*Figure 1.15b,c*). In comparison to mesoporous, planar structure does not require a high temperature processing condition. Therefore, planar structures are more advantageous in being

used in thin film flexible PSC [50]. In PSCs, the internal electric field is created by a potential difference at the interfaces between the perovskite active layer and two specialized materials called extraction layers. This architecture, referred to as p-i-n (or n-i-p), depending on the polarity), places an intrinsic perovskite layer between an n-type electron transport layer (ETL) and a p-type layer hole transport layer (HTL). The p-type layer, characterized by a low Fermi level, facilitates the extraction of holes, while the n-type layer, with a high Fermi level, enables the extraction of electrons [51]. The placement of HTL and ETL defines the device architecture. In the n-i-p of PSCs, the device structure follows the arrangement: TCO/ETL/perovskite/HTL/metal (front contact). In contrast, in the p-i-n, the structure is organized as: TCO/HTL/perovskite/ETL/metal (front contact). In the p-i-n configuration, hole transport layers (HTLs) can include p-type metal oxides such as NiO_x, polymeric materials like poly(triarylamine) (PTAA), Poly(3,4-ethylenedioxythiophene) polystyrene sulfonate (PEDOT: PSS) and self-assembled monolayer-based compounds such as (2-(3,6-Dimethoxy-9H-carbazol-9-yl)ethyl]phosphonic Acid (MeO-2PACZ). The perovskite layer is typically deposited on top of the HTL, often using solution methods or thermal evaporation. Electron transport layers (ETLs), such as C_{60} or PCBM, are then deposited on top of the perovskite layer.

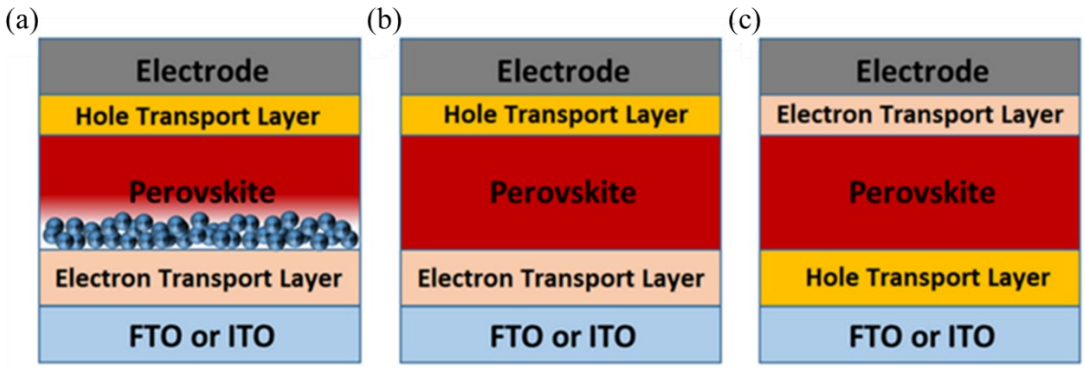

Figure 1.15 Schematic demonstration of different-structured PSCs with all the essential layers: a) n–i–p mesoporous structure; b) n–i–p planar structure; and c) inverted p–i–n planar structure [32].

The regular-type perovskite solar cells (PSCs) consist of an n-type metal oxide blocking layer (BL), with or without (planar or heterostructured/mesoporous) a metal oxide scaffold such as mp-TiO_2, Zn_2SnO_4, ZnO, Y:TiO_2, SnO_2, $BaSnO_3$, Al_2O_3, SiO_2@Al_2O_3, or Au@TiO_2, etc., sensitized with perovskite material. This configuration may or may not include an organometallic halide perovskite over-layer. The hole transport materials (HTMs) commonly used include spiro-OMeTAD, PTAA, P3HT, CuSCN, and CuI. The counter electrodes are typically made of materials such as Au, Ag, Al, etc. [52].

1.7.2 *Importance of Interfaces in planar PSCs.*

In the architecture of perovskite solar cells, the interfaces between different layers play a crucial role in determining device performance, particularly in terms of charge extraction and stability. The n-i-p and p-i-n configurations have distinct interface characteristics that significantly affect the charge transport and recombination behavior.

In the n-i-p architecture, the ETM is positioned at the front of the perovskite layer, with the HTM placed at the back. The interfaces of interest in this configuration are the ETM/perovskite

and perovskite/HTM interfaces. At the ETM/perovskite interface, the energy level alignment is critical for efficient electron extraction. The conduction band minimum (CBM) of the perovskite should be higher than that of the ETM to facilitate electron transfer. Similarly, at the perovskite/HTM interface, proper alignment of the valence band maximum (VBM) of the perovskite with the HOMO of the HTM ensures effective hole extraction (*Figure 1.16a*). However, challenges such as energy level mismatches, lattice mismatches, and interfacial defects can lead to charge recombination at these interfaces, which can degrade efficiency [53]. Additionally, the use of compact ETMs like TiO_2, SnO_2, or ZnO typically enhances electron extraction in the reverse scan direction, but hysteresis due to ion migration within the perovskite layer remains a significant issue. In contrast, the p-i-n architecture places the HTM at the front, with the ETM at the back, creating the HTM/perovskite and perovskite/ETM interfaces in a reversed order compared to the n-i-p configuration (*Figure 1.16b*). This structural difference alters the energy alignment and transport characteristics.

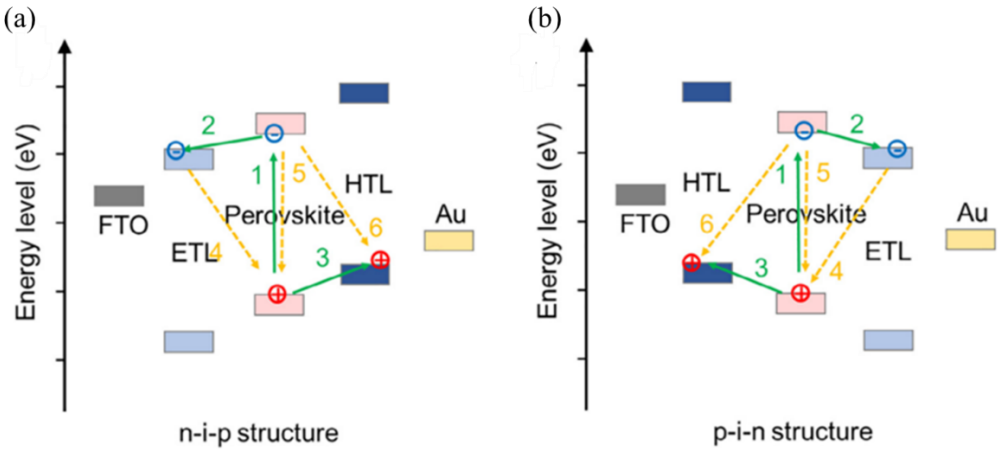

Figure 1.16 The typical charge carrier transfer process of (a) n-i-p and (b) p-i-n structured PSCs: 1. Photo-generation of electron-hole pairs in the perovskite absorber layer, 2. Electron extraction and transport process, 3. Hole extraction and transport process. 4, 5, 6 are undesired charge recombination processes taking place in working devices [54].

The HTM's HOMO must align properly with the VBM of the perovskite to allow efficient hole extraction at the HTM/perovskite interface, while the ETM's CBM must be higher than that of the perovskite to facilitate electron extraction at the perovskite/ETM interface. One of the advantages of the p-i-n architecture is that it typically shows less hysteresis, especially when fullerene derivatives are used as the ETM. Fullerene-based materials help minimize recombination and charge accumulation at the interfaces, providing more stable charge extraction and reducing the effects of ion migration in the perovskite layer [55]. In 2013, Jeng et al. [56] were the first to use fullerene in PSCs, employing a C_{60}/perovskite PHJ that achieved a PCE of 3.9%. Since then, fullerene has played a crucial role in advancing this technology due to its unique structural properties and excellent electronic characteristics. The interfaces in both the n-i-p and p-i-n configurations are vital for optimizing charge dynamics and minimizing recombination. In the n-i-p structure, achieving high performance often requires addressing hysteresis and improving the stability of the electron transport layer. In contrast, the p-i-n structure, with fullerene-based ETMs, tends to mitigate these issues, offering a more stable interface configuration and improved overall performance. The careful design and engineering

of these interfaces, including the choice of materials, their energy level alignments, and defect passivation strategies, are essential for enhancing both the efficiency and long-term stability of PSCs, regardless of the architecture.

1.8 Additives Engineering.

Depending on the specific additive composition as well as the processing route, the use of additives can affect perovskite crystallization and film formation, defect passivation in the bulk and at the surface/interface, and/or interface tuning of structure and energetics. Additives can modulate the crystal growth kinetics, influencing the size, orientation, and uniformity of perovskite grains. Controlling these factors, it is possible to reduce non-radiative recombination losses, enhance charge carrier lifetimes, and improve the overall efficiency of devices. Defect passivation plays a critical role in mitigating charge trapping and recombination at defect sites, which are often caused by vacancies, interstitials, or other structural imperfections. Additives, such as halide salts, Lewis bases or acids, ionic liquids and polymers can interact with these defect sites, neutralizing their detrimental effects and thus enhancing material stability and device longevity. The addition of a Lewis acid in perovskite can form a Lewis adduct with the undercoordinated halides and PbI_3^- through coordinate bonding or ionic bonding, eliminating the corresponding defects or traps and reducing undesired nonradiative recombination for longer carrier lifetimes (e.g., metal cations, fullerene derivatives). Lewis bases usually function as electron donors, which can bind to the positively charged undercoordinated Pb^{2+} ions, forming a Lewis adduct and passivating the defects [57]. Typical examples of Lewis-base additives are based on the donor (D) type such as O-donor, S-donor, and N-donor.

Low-cost and green polymer, like ethyl cellulose (EC), was also used recently as an additive to enlarge crystal grain size and decrease defect density [58]. These improvements are attributed to the EC additives with hydrogen-bonding interactions with perovskites, leading to passivation of defect traps at the GBs. The long chain of EC also acts as a scaffold for maintaining the perovskite structure, which suppresses the lattice strain induced by annealing during the film fabrication process. In 2018, Giuri et al. [59] studied the effect of biopolymer starch as an additive in perovskite materials, demonstrating that the –OH groups of the polymer interact with the precursors, forming a stable sol-gel network. This delays crystallization, improving the film morphology with larger grains and enhanced thermodynamic stability. In photovoltaic devices, the composite achieved an efficiency of 18.8%, with high reproducibility, despite the insulating nature of the starch.

Additive modification to the existing perovskite layer in a device stack is also often found useful to improve device efficiency and stability to significantly affect the perovskite/CTL interface with enhanced cell performance. One of the most common methods to modify the perovskite/CTL interface is the incorporation of a thin layer of 2D perovskite film on top of 3D perovskites. The hybrid 3D/2D perovskite films often exhibit longer carrier lifetimes and lower defect densities. The 2D interfacial layer is normally introduced as a postgrowth treatment of 3D perovskite with an isopropyl alcohol solution containing bulky organic cations that normally react with PbI_2 to form 2D perovskites [60]. Examples include butylammonium iodide, octylammonium iodide (OAI), cyclopropyl ammonium iodide, pentafluorophenylethylammonium iodide and diethylenetriamine. This strategy is mainly used to form a wide-bandgap semiconductor on top of the perovskite surface, which not only

eliminates the deep level traps at the grain surface but also forms a heterojunction to further hinder nonradiative recombination. The energy offset at this junction may create an electronic barrier to hinder the charge transfer across the perovskite grain and between the perovskite and the charge transport layer.

1.9 Motivation.

PSCs have shown remarkable performance, but they still face significant challenges related to stability and long-term efficiency.

This thesis first explores the use of biomaterials, studying their potential for stabilizing and enhancing performance of wide-band gap perovskite Chapter 3. It then examines the use of innovative materials in full-inorganic solar cells, with a focus on TTH as an interface material Chapter 4. Finally, the interface engineering through plasma treatments is explored, which, being low-energy processes, also contribute to reducing the environmental impact of the production process Chapter 5.

The goal of this thesis is to make a significant contribution to the optimization of perovskite solar cells, promoting more sustainable technological solutions ready for industrial applications, fusing biomaterials, innovative materials, and eco-friendly techniques such as plasma.

1.10 References.

[1] Solar Cells and Light Management: Materials, Strategies and Sustainability. Francesco Enrichi, Giancarlo Righini. Chapter 1 page 5-7.

[2] Pseudo-halide anion engineering for α-$FAPbI_3$ perovskite solar cells. J. Jeong, M. Kim, J. Seo, H. Lu, P. Ahlawat, A. Mishra, Y. Yang, M. A. Hope, F. T. Eickemeyer, M. Kim, Y. J. Yoon, I. W. Choi, B. P. Darwich, S. J. Choi, Y. Jo, J. H. Lee, B. Walker, S. M. Zakeeruddin, L. Emsley, U. Rothlisberger, A. Hagfeldt, D. S. Kim, M. Grätzel, J. Y. Kim. Nature 592 (2021) 381.

[3] Recent progress in perovskite solar cells. M.Khalaji Assadi, S. Bakhoda, R. Saidur, H. Hanaei. Renewable and Sustainable Energy Reviews 81 (2018) 2812–2822.

[4] Promises and challenges of perovskite solar cells. Juan-Pablo Correa-Baena, Michael Saliba, Tonio Buonassisi, Michael Grätzel, Antonio Abate, Wolfgang Tress, Anders Hagfeldt. Science 358 (2017) 739–744.

[5] https://creativecommons.org/licenses/by-sa/4.0/

[6] Nanostructured Heterojunction Crystalline Silicon Solar Cells with Transition Metal Oxide Carrier Selective Contacts. Thesis for: Ph.D. Maksym Plakhotnyuk.

[7] The Physics of Solar Cells J. Nelson. Imperial College. World Scientific Publishing Co., 2003.

[8] Characterizing the Efficiency of Perovskite Solar Cells and Light-Emitting Diodes. Su-Hun Jeong, Jaehyeok Park, Tae-Hee Han, Fei Zhang, Kai Zhu, Joo Sung Kim, Min-Ho Park, Matthew O. Reese, Seunghyup Yoo and Tae-Woo Lee. Joule. 4 (2020) 1206–1235.

[9] Approaching the Shockley-Queisser limit: General assessment of the main limiting mechanisms in photovoltaic cells Alexis Vossier, Federico Gualdi, Alain Dollet, Richard Ares and Vincent Aimez. AIP Publishing LLC. 117 (2015) 015102/8.

[10] National Renewable Energy Laboratory (NREL), Best Research-Cell Efficiency Chart https://www.nrel.gov/pv/cell-efficiency.html

[11] An introduction to solar cell technology. Kiran Ranabhat, Leev Patrikeev, Aleksandra Antal'evna Revina, Kirill Andrianov, Valerii Lapshinsky, Elena Sofronova. Journal of Applied Engineering Science 14 (2016) 405.

[12] Towards high efficiency thin film solar cells. Guifang Han, Sam Zhang, Pablo P. Boix, Lydia Helena Wong, Lidong Sun, Shui-Yang Lien. Progress in Materials Science. 87 (2017) 246-291.

[13] Perovskite solar cells: an emerging photovoltaic technology. Nam-Gyu Park. Materials Today 18 (2015) 65-72.

[14] A general approach to high-efficiency perovskite solar cells by any antisolvent. Alexander D. Taylor, Qing Sun, Katelyn P. Goetz, Qingzhi An, Tim Schramm, Yvonne Hofstetter, Maximillian Litterst, Fabian Paulus & Yana Vaynzof. Nature Communications 12 (2021) 1878.

[15] The emergence of perovskite solar cells. Martin A. Green, Anita Ho-Baillie & Henry J. Snaith. Nature Photonics 8 (2014) 506–514.

[16] Solid-state principles applied to organic−inorganic perovskites: new tricks for an old dog. Kieslich, G.; Sun, S.; Cheetham, A. K. Chem. Sci. 5 (2014) 4712−4715.

[17] The laws of crystal chemistry. V. M. Goldschmidt. Naturwissenschaften,14 (1926) 477–485.

[18] Stabilizing Perovskite Structures by Tuning Tolerance Factor:Formation of Formamidinium and Cesium Lead Iodide Solid-StateAlloys. Zhen Li, Mengjin Yang, Ji-Sang Park, Su-Huai Wei, Joseph J. Berry and Kai Zhu. Chem. Mater. 28 (2016) 284−292.

[19] An extended Tolerance Factor approach for organic–inorganic perovskites. Gregor Kieslich, Shijing Sun and Anthony K. Cheetham. Chem. Sci. 6 (2015) 3430-3433.

[20] Emerging Characterizing Techniques in the Fine Structure Observation of Metal Halide Perovskite Crystal. Kongchao Shen, Jinping Hu, Zhaofeng Liang, Jinbang Hu, Haoliang Sun, Zheng Jiang and Fei Song. Crystals 8 (2018) 232.

[21] Synthesis and crystal chemistry of the hybrid perovskite $(CH_3NH_3)PbI_3$ for solid-state sensitised solar cell applications. Tom Baikie, Yanan Fang, Jeannette M. Kadro, Martin Schreyer, Fengxia Wei, Subodh G. Mhaisalkar, Michael Graetzel and Tim J. White. J. Mater. Chem. A, 1 (2013) 5628–5641.

[22] Analysis of Multivalley and Multibandgap Absorption and Enhancement of Free Carriers Related to Exciton Screening in Hybrid Perovskites. Even. J.; Pedesseau, L.; Katan, C.. J. Phys. Chem. C. 118 (2014) 11566−11572.

[23] Theoretical Treatment of $CH_3NH_3PbI_3$ Perovskite Solar Cells. Sining Yun, Xiao Zhou, Jacky Even, and Anders Hagfeldt. Angew. Chem. Int. Ed., 56 (2017) 15806 – 15817.

[24] The Relation between Rotational Dynamics of the Organic Cation and Phase Transitions in Hybrid Halide Perovskites. Sudeep Maheshwari, Magnus B. Fridriksson, Sayan Seal, Jörg Meyer and Ferdinand C. Grozema. J. Phys. Chem. C 123 (2019) 14652−14661.

[25] A close examination of the structure and dynamics of $HC(NH_2)_2PbI_3$ by MD simulations and group theory. Carignano, M. A.; Saeed, Y.; Aravindh, S. Assa; Roqan, I. S.; Even, J.; Katan, C. Physical Chemistry Chemical Physics 18 (2016) 27109-27118.

[26] Chemical management for colorful, efficient, and stable inorganic-organic hybrid nanostructured solar cells. Jun Hong Noh, Sang Hyuk Im, Jin Hyuck Heo, Tarak N Mandal, Sang Il Seok. Nano Lett. 13 (2013)1764-9.

[27] Electron-Hole Diffusion Lengths Exceeding 1 Micrometer in an Organometal Trihalide Perovskite Absorber. Samuel D. Stranks, Giles E. Eperon, Giulia Grancini, Christopher Menelaou, Marcelo J. P. Alcocer, Tomas Leijtens, Laura M. Herz, Annamaria Petrozza, Henry J. Snaith. Science 342 (2013) 341.

[28] Role of the chemical substitution on the structural and luminescence properties of the mixed halide perovskite thin $MAPbI_{3-x}Br_x$ ($0 \leq x \leq 1$) films. Lahoucine Atourki, Erika Vega, Bernabé Marí, Miguel Mollar, Hassan Ait Ahsaine, Khalid Bouabid, Ahmed Ihlal. Applied Surface Science 371 (2016) 112–117.

[29] Interface energetics in organo-metal halide perovskite-based photovoltaic cells. Philip Schulz, Eran Edri, Saar Kirmayer, Gary Hodes, David Cahen and Antoine Kahn. Energy Environ. Sci. 7 (2014) 1377-1381.

[30] Review of recent progress in chemical stability of perovskite solar cells. Guangda Niu, Xudong Guo and Liduo Wang. J. Mater. Chem. A. 3 (2015) 8970.

[31] Investigation of $CH_3NH_3PbI_3$ Degradation Rates and Mechanisms in Controlled Humidity Environments Using Situ Techniques. J. Yang, B. D. Siempelkamp, D. Liu, T. L. Kelly, ACS Nano. 9 (2015) 1955.

[32] Stability Issues of Perovskite Solar Cells: A Critical Review. Shahriyar Safat Dipta and Ashraf Uddin. Energy Technol. 9 (2021) 2100560.

[33] Water-Accelerated Photooxidation of $CH_3NH_3PbI_3$ Perovskite. Timothy D. Siegler, Wiley A. Dunlap-Shohl, Yuhuan Meng, Yuhang Yang, Wylie F. Kau, Preetham P. Sunkari, Chang En Tsai, Zachary J. Armstrong, Yu-Chia Chen, David A. C. Beck, Marina Meila, and Hugh W. Hillhouse˘. J.A.C.S. 144 (2022) 5552−5561.

[34] Light induced metastable modification of optical properties in $CH_3NH_3PbI_{3-x}Br_x$ perovskite films: Two-step mechanism. Xiao Yang, Xiaoliang Yan, Wei Wang, Xiangxiang Zhu, Heng Li, Wanli Ma, ChuanXiang Sheng. Organic Electronics 34 (2016) 79-83.

[35] Unusual defect physics in $CH_3NH_3PbI_3$ perovskite solar cell absorber. Wan-Jian Yin; Tingting Shi; Yanfa Yan. Appl. Phys. Lett. 104 (2014) 063903.

[36] A halide exchange engineering for $CH_3NH_3PbI_{3-x}Br_x$ perovskite solar cells with high performance and stability. Weidong Zhua, Chunxiong Baoa, Faming Lia, Tao Yua, Hao Gaoa, Yong Yia, Jie Yanga, Gao Fua, Xiaoxin Zhoua, Zhigang Zou. Nano Energy. 19 (2016) 17-26.

[37] Reversible photo-induced trap formation in mixed-halide hybrid perovskites for photovoltaics. Eric T. Hoke, Daniel J. Slotcavage, Emma R. Dohner, Andrea R. Bowring, Hemamala I. Karunadasa and Michael D. McGehee. Chem. Sci. 6 (2015) 613-617.

[38] Effect of Light Illumination on Mixed Halide Lead Perovskites: Reversible or Irreversible Transformation. Weixin Huang, Seog Joon Yoon and Pitambar Sapkota. ACS Appl. Energy Mater. 1 (2018) 2859−2865.

[39] Ion–Dipole Interaction Enabling Highly Efficient $CsPbI_3$ Perovskite Indoor Photovoltaics. Kai-Li Wang, Haizhou Lu, Meng Li, Chun-Hao Chen, Ding- Bo Zhang, Jing Chen, Jun-Jie Wu, Yu-Hang Zhou, Xue-Qi Wang, Zhen-Huang Su, Yi-Ran Shi, Qi-Sheng Tian, Yu-Xiang Ni, Xing-Yu Gao, Shaik M. Zakeeruddin, Michael Grätzel, Zhao-Kui Wang and Liang-Sheng Liao. Adv. Mater., 35 (2023), 2210106.

[40] Untapped Potentials of Inorganic Metal Halide Perovskite Solar Cells**.** Anita Ho-Baillie, Meng Zhang, Cho Fai Jonathan Lau, Fa-Jun Ma and Shujuan Huang. Joule 3, (2019), 938–955.

[41] Efficient and Stable Graded $CsPbI_{3-x}$ Br_x Perovskite Solar Cells and Submodules by Orthogonal Processable Spray Coating. Jin Hyuck Heo, Fei Zhang, Chuanxiao Xiao, Su Jeong Heo, Jin Kyoung Park, Joseph J. Berry, Kai Zhu, and Sang Hyuk Im. Joule 5, (2021), 481–494.

[42] Stability of all-inorganic perovskite solar cells. Nabonswende Aida Nadege Ouedraogo, Yichuan Chen, Yue Xiao, Qi Meng, Chang Bao Han, Hui Yan, Yongzhe Zhang. Nano Energy 67 (2020) 104249.

[43] The Structure of Caesium Plumbo Iodide $CsPbI_3$. C.K. Møller. Mat. Fys. Medd. Dan. Vid. Sels. 32 (1959) 1.

[44] Anharmonicity and Disorder in the Black Phases of Cesium Lead Iodide Used for Stable Inorganic Perovskite Solar Cells. Arthur Marronnier, Guido Roma, Soline Boyer-Richard, Laurent Pedesseau, Jean-Marc Jancu, Yvan Bonnassieux, Claudine Katan, Constantinos C. Stoumpos, Mercouri G. Kanatzidis and Jacky Even. ACS Nano 12 (2018) 3477−3486.

[45] Temperature-dependence of the band gap in the all-inorganic perovskite $CsPbI_3$ from room to high temperatures. Jinyan Ning, Liangliang Zheng, Wenxin Lei, Shenghao Wang, Jinyang Xi and Jiong Yang. Phys. Chem. Chem. Phys. 24 (2022) 16003–16010.

[46] Cubic or orthorhombic? Revealing the crystal structure of metastable blackphase CsPbI 3 by theory and experiment. Sutton R.J., Filip M.R., Haghighirad A.-A., Sakai N., Wenger B., Giustino F., and Snaith H.J. ACS Energy Lett. 3 (2018) 1787–1794.

[47] Organometal Halide Perovskites as Visible-Light Sensitizers for Photovoltaic Cells. Akihiro Kojima, Kenjiro Teshima, Yasuo Shirai and Tsutomu Miyasaka. J. Am. Chem. Soc. 131 (2009) 6050–6051.

[48] Mesoporous perovskite solar cells and the role of nanoscale compact layers for remarkable all-round high efficiency under both indoor and outdoor illumination. F. Di Giacomo, V.

Zardetto, G. Lucarelli, L. Cinà, A. Di Carlo, M. Creatore, T.M. Brown. Nano Energy, 30 (2016) 460–469.

[49] Perovskite-based solar cells: impact of morphology and device architecture on device performance. Teddy Salim, Shuangyong Sun, Yuichiro Abe, Anurag Krishna, Andrew C. Grimsdale and Yeng Ming Lam. J. Mater. Chem. A. 3 (2015) 8943–8969.

[50] Device Optimization of PIN Structured Perovskite Solar Cells: Impact of Design Variants. Yousaf Hameed Khattak, Faisal Baig, Ahmed Shuja, Lahoucine Atourki, Kashif Riaz and Bernabé Marí Soucase. ACS Appl. Electron. Mater. 3 (2021) 3509−3520.

[51] High-Efficiency Perovskite Solar Cells. Jin Young Kim, Jin-Wook Lee, Hyun Suk Jung, Hyunjung Shin and Nam-Gyu Park. Chem. Rev. 120 (2020) 7867−7918.

[52] p-i-n/n-i-p type planar hybrid structure of highly efficient perovskite solar cells towards improved air stability: synthetic strategies and the role of p-type hole transport layer (HTL) and n-type electron transport layer (ETL) metal oxides. Sawanta S. Mali and Chang Kook Hong. Nanoscale 8 (2016) 10528–10540.

[53] Interface Engineering for Highly Efficient and Stable Planar p-i-n Perovskite Solar Cells. Yang Bai, Xiangyue Meng and Shihe Yang. Adv. Energy Mater. 8 (2018) 1701883.

[54] Charge-transport layer engineering in perovskite solar cells. Ming Cheng, Chuantian Zuo, Yongzhen Wu, Zhongan Li, Baomin Xu, Yong Hua, Liming Ding. Science Bulletin 65 (2020) 1237–1241.

[55] Fullerene-Based Inverted Perovskite Solar Cell: A Key to Achieve Promising, Stable, and Efficient Photovoltaics. Raneen Zahran and Zafer Hawash. Adv. Mater. Interfaces. 9 (2022) 2201438.

[56] $CH_3NH_3PbI_3$ Perovskite/Fullerene Planar-Heterojunction Hybrid Solar Cells. Jun-Yuan Jeng, Yi-Fang Chiang, Mu-Huan Lee, Shin-Rung Peng, Tzung-Fang Guo, Peter Chen and Ten-Chin Wen. Adv. Mater. 25 (2013) 3727–373.

[57] Additive Engineering for Efficient and Stable Perovskite Solar Cells. Zhang and Kai Zhu. Adv. Energy Mater. 10 (2020) 1902579.

[58] Extremely Low-Cost and Green Cellulose Passivating Perovskites for Stable and High-Performance Solar Cells. J. Yang, S. Xiong, T. Qu, Y. Zhang, X. He, X. Guo, Q. Zhao,S. Braun, J. Chen, J. Xu, Y. Li, X. Liu, C. Duan, J. Tang, M. Fahlman,Q. Bao, ACS Appl. Mater. Interfaces 11 (2019) 13491.

[59] Polymeric rheology modifier allows single-step coating of perovskite ink for highly efficient and stable solar cells. A. Giuri, S. Masi, A. Listorti, G. Gigli, S. Colella, C. E. Corcione and A. Rizzo, Nano Energy.54 (2018) 400.

[60] Enhancing moisture tolerance in efficient hybrid 3D/2D perovskite photovoltaics. T. M. Koh, V. Shanmugam, X. Guo, S. S. Lim, O. Filonik,E. M. Herzig, P. Müller-Buschbaum, V. Swamy, S. T. Chien,S. G. Mhaisalkar, N. Mathews, J. Mater. Chem. A. 6 (2018) 2122.

Chapter 2

Materials and methods.

2.1 Materials.

Unless otherwise stated, all materials were used as received without further purification.

2.1.1 Reagents.

Cesium Iodide (CsI, AnhydroBeads™, 99.999% trace metals basis, (Perovskite grade)), is purchased from Sigma Aldrich. Formammidinium Iodide (FAI) and Methylammonium iodide (MAI) ≥99% anhydrous are purchased Sigma Aldrich. Lead iodide (PbI_2) in pellets 99,9999% ultra dry is purchased from Thermo Fisher.

Dimethylammonium chloride (for synthesis) and β-carotene are purchased from Sigma-Aldrich are purchased Sigma Aldrich Polyhydroxybutyrate (PHB) in pellets was supplied by the company Egg Plant.

2.1.2 Solvents.

Chlorobenzene (CB), Dimethyl sulfoxide (DMSO), Dimethylformamide (DMF) and N-methyl-2-pyrrolidone (NMP) anhydrous 99.8% are purchased from Sigma Aldrich. 2-propanol 99.5%, anhydrous was purchased from Sigma Aldrich.

Toluene 99.8% anhydrous is purchased from Sigma Aldrich. Diethyl ether ≥99.0% anhydrous, ACS reagent, containing BHT as inhibitor is purchased from Sigma Aldrich.

2.1.3 Charge transports materials.

Poly(3,4-ethylenedioxythiophene)-poly(styrenesulfonate) (PEDOT:PSS) aqueous solution (PVP AI 4083) is purchased from Ossila. [2-(9H-carbazol-9-yl)ethyl]-phosphonic acid (2PACZ) and ((2-(3,6-Dimethoxy-9H-carbazol-9-yl)ethyl)phosphonic acid (MeO-2PACZ) are purchased from TCI and Ossila respectively.

[6,6]-Phenyl C_{61} butyric acid methyl ester (PCBM) and Fullerene C_{60} (sublimed, 99.99%) are purchased from nano-C. Bathocuproine (BCP) sublimated grade (purity>99,5%) is purchased from Ossila.

2.2 Kinetic Models of Perovskite Crystal Growth.

The perovskite crystal growth is a kinetic process of nucleation and crystallization, relying on LaMer and Ostwald ripening models. An in-depth understanding of the models is a prerequisite for modulating the all-inorganic perovskite film morphology. Perovskite crystal growth involves both nucleation and crystallization, driven by thermodynamic factors, especially the change in free energy (ΔG). Nucleation occurs when the solute concentration exceeds its solubility limit, and it can be either homogeneous or heterogeneous. In homogeneous nucleation, the total free energy (ΔG) is the sum of the surface free energy (ΔG_s) and the bulk

free energy (ΔG_v) (equation 2.1). The critical radius (r*) is the point at which nucleation becomes stable. If the nucleus size exceeds r*, the nucleus will grow; if it is smaller, it will dissolve back into the solution. In heterogeneous nucleation, nuclei form at specific sites (e.g., substrates), which lowers the energy barrier for nucleation (*Figure 2.1a*). After nucleation, crystal growth proceeds through two mechanisms: diffusion-controlled growth and surface reaction.

$$\Delta G = \Delta G_V + \Delta G_S \tag{2.1}$$

$$J = 4\pi r^2 D \frac{d[C]}{dx} \tag{2.2}$$

In diffusion-controlled growth, solute molecules diffuse from the solution to the nucleus surface, as described by Fick's law [1], as shown in equation 2.2 where J, r, D, and C refer to the total flux of monomers, the particle radius, the diffusion coefficient, and the monomer concentration at a distance from the surface (x), respectively. In surface reaction-controlled growth, monomers are consumed at the particle surface as the crystal grows. Both nucleation and growth processes play a critical role in determining the morphology and quality of the perovskite films. The LaMer mechanism describes nucleation and crystal growth in three stages: (I) monomer accumulation without nucleation; (II) nucleation triggered at a critical concentration (C_{min}), accelerating until a peak (C_{max}); and (III) crystal growth as monomer concentration drops below C_{min}, ending near the solubility limit (C_s). A short nucleation phase and gradual growth yield high-quality films with larger grains and fewer defects, enhancing PSC performance and stability (*Figure 2.1b*). The Ostwald ripening mechanism explains perovskite grain growth through competitive particle growth in solutions.

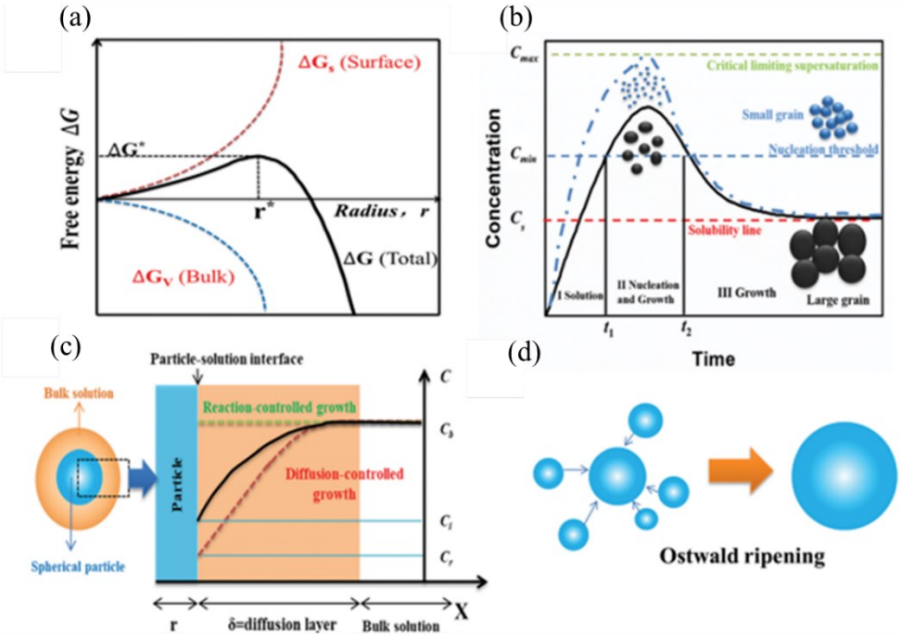

Figure 2.1 (a) Schematic representation of the classical free energy diagram for homogeneous nucleation as a function of particle radius. (b) LaMer diagram for monodispersed particle formation. (c) Schematic illustration of the diffusion layer near the surface of a nanocrystal and monomer concentration as a function of distance (x). (d) Schematic diagram of Ostwald ripening [1].

Larger particles grow at the expense of smaller ones due to differences in surrounding monomer concentrations, driven by thermodynamic principles. This process leads to the formation of larger grains over time, influencing the film morphology and quality as shown in *Figure 2.1d*.

2.3 Perovskite film formation for optoelectronic applications

Precursors for metal halide perovskites, such as Pb(II) halides (e.g., PbI_2, $PbBr_2$, $PbCl_2$) and organic halides (e.g., CH_3NH_3I, $HC(NH_2)_2I$), are Lewis acids that interact with Lewis bases to form redox products or adducts linked by dative bonds. The intermediate adduct phase formed in these Lewis acid–base reactions plays a key role in homogeneous perovskite crystal growth. This phase facilitates the removal of Lewis bases, slowing the rate of perovskite formation and allowing for better crystal quality.

Commonly used Lewis bases in perovskite synthesis include polar aprotic small molecules, such as DMSO, urea and NMP, which form molecular adducts with the perovskite precursors. These solvents, along with others like DMF and γ-butyrolactone (GBL), strongly coordinate with Pb^{2+} centers, influencing solubility and crystallization. Solvent-solute coordination, determined by factors such as donor number (DN), polarity, and dielectric constant, significantly impacts perovskite film quality by competing with iodide ions for Pb^{2+} coordination.

Among deposition methods, solvent-engineering is widely used to produce high-quality perovskite films. In this method, the perovskite precursor solution is spin-coated, followed by antisolvent treatment to extract the host solvent and trigger crystallization. The interaction between the solvent and antisolvent, often governed by dipole-dipole forces, plays a critical role in modulating film morphology [2]. Literature highlights the importance of solvent coordination with Pb^{2+} and the diffusion of antisolvent into the precursor, demonstrating that small variations in solvent properties can profoundly affect crystallization dynamics and the final crystal structure.

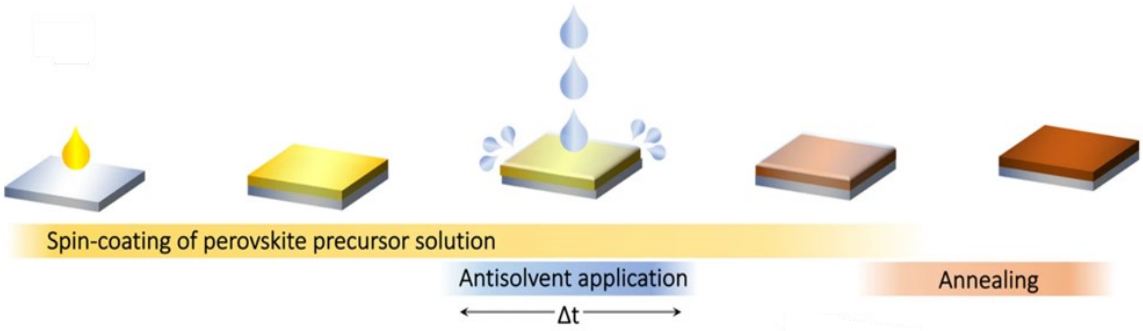

Figure 2.2 Schematic depiction of the perovskite layer fabrication process [2].

When an antisolvent is added to a solution, it immediately reduces the solubility, creating local supersaturation conditions. This leads to precipitation or crystallization. The precipitation method is rapid and efficient. Antisolvent treatment on the perovskite layer, a one-step process, has become one of the most successful and widely used techniques to improve perovskite layer quality in PSCs [3,4].

Unlike typical organic-inorganic perovskite films, the solution deposition of $CsPbI_3$ perovskite thin films does not use an antisolvent but relies on unassisted natural nucleation. Therefore, three crucial factors are essential: (1) regulating the colloid size and chemical phase in the

precursor solution, (2) minimizing the critical nucleation energy of intermediate phases during wet film condensation, and (3) accelerating perovskite nucleation kinetics while ensuring sufficient grain growth time. These factors are vital for controlling crystal nucleation and growth to achieve high-quality $CsPbI_3$ films. An ideal unassisted solution deposition requires rapid condensation of uniformly distributed nuclei with an appropriate packing density, quick in-situ transformation from the intermediate phase to the perovskite phase, and an extended grain growth period to allow these nuclei to grow into continuous, smooth, and dense polycrystalline thin films [5].

2.4 Perovskites Solutions.

2.4.1 $MAPb(I_{1-x}Br_x)_3$ Perovskite Solution.

The perovskite solutions are obtained by preparing mother solutions of $MAPbI_3$ 1 M (MAI:PbI_2 = 1:1) and $MAPbBr_3$ 1 M (MABr:$PbBr_2$ = 1:1) employing equivalent molar concentrations of DMSO and DMF as solvent, which are then stoichiometrically mixed together for the $MAPb(I_{1-x}Br_x)_3$ formulations ($MAPb(I_{0.8}Br_{0.2})_3$ and $MAPb(I_{0.7}Br_{0.3})_3$). A 1 mM stock solution of β-carotene in toluene is prepared and used depending on the approach. All solutions are stored in an N_2-filled glovebox after the preparation and covered with aluminum foil.

2.4.2 $DMAPbI_3$ powder synthesis

$DMAPbI_3$ precursor is prepared by dissolving PbI_2 (4.62 g) in DMF (10 mL) and then adding HI (3.6 mL), followed by stirring at 50°C overnight to ensure complete reaction. To remove excess HI, the precursor is then washed in absolute ethanol to obtain the light-yellow precipitate. The obtained powder is dried in vacuum at 65°C for 12 h and stored in a nitrogen glovebox [6,7].

2.4.3 $CsPbI_3$ Perovskite Solution.

CsI and $DMAPbI_3$ powder in a molar ratio 1:1 are dissolved in 1 mL DMF to obtain a final concentration of 0.6M, followed by stirring for 1h at 60°C. To regulate the crystallization process of the $CsPbI_3$ perovskite films, DMACl is incorporated into the precursor solutions in a concentration of 2,28mg/ml [8].

2.4.4 $FAPbI_3$ and PHBs Perovskite Solution.

172mg FAI, 461mg PbI_2 and 26mg CsI are mixed in 96,3uL NMP and 590,71uL DMF, followed by stirring for 1h at 60°C. The polyhydroxybutyrate (PHB) is dissolved at a concentration of 1 mg/mL in DMF, and the necessary amount of this stock solution was subsequently added to the perovskite solution to achieve final concentrations of 0.5 mg/mL and 0.1 mg/mL.

2.4.5 $MAPbI_3$ Perovskite Solution.

$MAPbI_3$ solution was prepared in DMF, with 1:1:1 mol of MAI, PbI_2 and anhydrous DMSO and stirred for 1h at room temperature.

2.4.6 TTH.

TTH was synthesized according to procedure reported in literature [9].

2.5 Device fabrication.

For all the devices pre-patterned ITO glasses are washed with detergent solution (Semico Clean 56, Furuuchi chemical), water, and isopropanol, followed by drying with an air gun and performed UV-Ozone treatment before the HTL deposition.

2.5.1. p-i-n device for $MAPb(I_{1-x}Br_x)_3$.

A p-i-n device architecture is developed using 15 × 15 × 1.1 mm ITO patterned glass substrates, 2PACZ as the HTL, the perovskite as the photoactive layer, $PC_{60}BM$ as the ETL, BCP as the buffer layer and Ag as the cathode top electrode. Except for the Ag all materials are deposited by spin coating in an N_2-filled glovebox (<0.1 ppm [O_2], <0.1 ppm [H_2O]) with the following parameters: 3000 rpm for 30 s followed by 100°C × 10 min annealing for a 1 mM solution of 2PACZ in 2-propanol, a dynamic washing step with 2-propanol and 100 °C × 10 min annealing, perovskite deposition as described above, and 1000 rpm for 60 s for 25 mg/mL chlorobenzene PCBM solution and 6000 rpm for 20 s for 0.5 mg/mL 2-propanol BCP solution. 60 nm Ag was thermally evaporated (Lesker Co. instrument) in high vacuum (5×10^{-6} mBar) as the cathode top electrode, with a deposition rate of 0.6 A/s.

2.5.2 p-i-n device for $CsPbI_3$.

The PEDOT:PSS hole transport layer is fabricated from an aqueous dispersion which is filtered through a 0.45 μm PVDF filter and then spin coated on the ITO substrate in air, using a spin program of 3500rpm for 40s and annealed at 80°C form 1 min and 120°C for 30min, then cooled to room temperature. Subsequently, the glass/ITO substrates with PEDOT:PSS deposited are transferred into a nitrogen-filled glove box. Cesium Lead Iodide solution is spin-coated on PEDOT:PSS and processed at 3000 rpm for 30 s without dripping. The obtained films are subsequently annealed onto a hot plate at 210 °C for 1 min and then cooled to room temperature. PCBM (10 mg/ml in CB) or TTH (0.75 mg/ml in CB) are spin-coated at 2000 rpm for 45 seconds, dried in N_2 glove box at room temperature without annealing for 20 minutes. The perovskite-coated samples are moved under N_2 to a vacuum deposition chamber, where 20 nm of C_{60} (deposition rate 0.01 nm s^{-1}) and 8 nm of BCP (deposition rate 0.01 nm s^{-1}) are deposited by thermal evaporation. The top electrode is prepared by depositing 110 nm of Ag through a shadow mask. The deposition rate for Ag was first set as 0.005 nm s^{-1} to reach 5 nm, then raised to 0.01 nm s^{-1} to reach 20 nm, and finally raised to 0.08 nm s^{-1} to reach the target thickness.

2.5.3 p-i-n device for $FAPbI_3$.

The MeO-2PACZ hole transport layer is fabricated from a 1mg/ml solution in ethanol and then spin coated on the ITO substrate in air, using a spin program of 3000rpm for 30s and annealed at 100°C form 10 min, then cooled to room temperature. Subsequently, the glass/ITO substrates with MeO-2PACZ deposited are transferred into a nitrogen-filled glove box. FAPI solution is spin-coated on MeO-2PACZ and processed at 5000 rpm for 17 s with dripping at 7s with diethyl ether. The obtained films are subsequently annealed onto a hot plate at 100 °C for 1 min and 165°C for 10 min. The perovskite-coated samples are moved under N_2 to a vacuum deposition chamber, where 20 nm of C_{60} (deposition rate 0.01 nm s^{-1}) and 8 nm of BCP (deposition rate 0.01 nm s^{-1}) are deposited by thermal evaporation. The top electrode is prepared by depositing 110 nm of Ag through a shadow mask. The deposition rate for Ag is first set as 0.005 nm s^{-1} to

reach 5 nm, then raised to 0.01 nm s^{-1} to reach 20 nm, and finally raised to 0.08 nm s^{-1} to reach the target thickness.

2.6 Films Characterizations.

Scanning Electron Microscopy (SEM)

The topographical and cross-sectional images are recorded by field emission scanning electron microscope (FEG-SEM) JEOL 3100F) operated at 5 kV. The SEM is recorded from films deposited on top of the ITO substrate.

Attenuated Total Reflectance - Fourier Transform Infrared Spectroscopy (ATR-FTIR).

A vacuum Bruker Vertex 70v Fourier transform infrared spectrometer is used to register the infrared absorption spectra of perovskite thin films deposited on glass in the range 400− 4000 cm^{-1} over 32 scans with a resolution of 4 cm^{-1}. Spectra are collected in attenuated total reflectance mode utilizing an ATR module equipped with a single reflection diamond ATR crystal (refractive index of 2.4). ATR-FTIR spectra are corrected in baseline.

X-Ray Diffraction (XRD).

The XRD spectra of perovskite films are measured with a PAN analytical X'Pert-PRO Materials Research Diffractometer using graphite-monochromated Cu Kα radiation (λ = 1.5405 Å).

X-ray Photoelectron Spectroscopy (XPS).

XPS analyses are performed with a Scanning XPS Microprobe (PHI 5000 Versa Probe II, Physical Electronics) equipped with a monochromatic Al Kα X-ray source (1486.6 eV), operated at 15 kV and 24.8 W, with a spot of 100 μm. Survey (0-1200 eV) and high-resolution spectra (C1s, O1s, N1s, I3d, Pb4f) are recorded in FAT (Fixed Analyser Transmission) mode at a pass energy of 117.40 eV and 29.35 eV, respectively. The analyser energy resolution, evaluated on the FWHM Ag 3d5/2 photoemission line, is 0.7 eV for a pass energy of 29.35 eV. A dual beam charge neutralizer, with a flux of low energy electrons (∼1 eV) combined with very low energy positive Ar^+ ions (10 e V), is used as the internal standard for surface charging compensation. The hydrocarbon component of C1s spectrum is used as internal standard for charging correction and it is fixed at 284.8 eV. All spectra are collected at an angle of 45° with respect to the sample surface. Atomic concentrations are determined from the high-resolution spectra after subtracting a Shirley-type background, using the Scofield sensitivity factors set in the MultiPak (Physical Electronics) data processing software.

Ellipsometry.

Ellipsometry measurements are performed on the glass/perovskite layers, pre and post plasma treatment, with the J.A. Woollam Co. M-2000 Ellipsometer, at three angles of incidence (50˚,55˚,60˚), in a wavelength range of 245-1690 nm. Data modelling is performed using the Complete EASE software (J.A. Woollam Company). The transparent region (λ > 800 nm) is fitted with the empirical Chauchy dispersion relation, using film thickness measured with the profilometer and the refractive index, as input data. The Cauchy model is parameterized by a B-spline model, extended to all wavelengths. The Kramers-Kronig consistency of the B-spline parametrization is enforced, before using the Gen-Osc model, composed of a Tauc-Lorentz,

three Psemi Triangle and a gaussian oscillators. To model the surface, an effective medium approximation (EMA) is adopted as a composite material consisting of perovskite and voids. This model accounts for the roughness and porosity often present on the perovskite layer surface [10].

Time resolved and steady state photoluminescence (PL) spectroscopy.
PL spectra were recorded by using a Fluorolog® -3 spectrofluorometer (HORIBA Jobin-Yvon, Edison, NJ, USA), equipped with a 450 W xenon lamp as the exciting source and double grating excitation and emission monochromators. The PL emission spectra are recorded at ambient temperature by using an excitation wavelength of 486 nm.

Ultraviolet-visible absorption spectroscopy
The absorption spectra are analyzed with a PerkinElmer spectrophotometer (Lambda 1050) in the 400−850 nm range, and the optical energy gap is determined by a Tauc plot method.

2.7 Devices Characterizations.

Solar cell characterization.
The current voltage (J-V) curves are measured using a Keithley 2612 source meter under AM 1.5 G (1000 Wm^{-2}) provided by a Solar Simulator Abet, Xenon short-arc lamp Ushio 150 watts, in the air at a temperature around 25°C and without encapsulation. Each curve is generated using 123 data points from a starting potential of 1.2 V to a final potential of -0.02 V (reverse scan; vice versa for the forward scan) using a scan rate of 10 mVs^{-1}. The active area of the cell is 0.121 cm^2. The operation stability was evaluated by Maximum Power Point Tracking under continuous illumination of 1 sun.

Electrochemical Impedance Measurements (EIS)
EIS are performed by applying 20 mV of a voltage perturbation at different frequencies from 1MHz to 0.1Hz in a PGSTAT-30 from Autolab and under 1 sun illumination at different applied potential, from 0 to 1.2 volts. A Xe lamp is used to illuminate the PSC controlling the light intensity with neutral density filters, at 1 sun (100 mW/cm2) in a logarithmic scale. The AC voltage perturbation is fixed at 20 mV under open-circuit conditions. The integration time is fixed at 0.125 s and the number of cycles is equal to 1. Each frequency spectrum is measured ranging between 1 MHz and 0.1 Hz. The recombination resistance is calculated by using the equivalent circuit previously reported [11].

Incident-photon-to current conversion efficiency (IPCE)
Measured using a QEPVSI-b Oriel measurement system and measured in DC mode.

2.8 Advanced techquinques.

Plasma Treatment.
Glass substrates and glass/perovskite layers are treated using a home-made parallel plate stainless steel capacitive reactor evacuated by a rotary pump. The upper shower electrode, 150

mm wide, is connected to a radiofrequency (RF, 13.56 MHz) power supply (Cesar Dressler) through a manual impedance matching unit. The lower electrode, 150 mm wide, is connected to the ground and set 30 mm apart from the upper RF electrode and acted as a sample holder. The chamber pressure is monitored by a pressure transducer (Baratron MKS Instruments) insensitive to gas composition and the gas flow rate is set using an electronic mass flow controller (MKS Instruments). The glass substrates are treated with an oxygen plasma to increase their hydrophilicity. The power delivered to the upper electrode is set to 30 W and the chamber pressure is fixed at 130 mTorr. The O_2 (Air Liquide) flow rate Is set to 10 sccm and the plasma treatment Is performed for 10 s. For the treatment of perovskite surfaces the power delivered Is set to the minimum that allows the ignition of a stable discharge, to explore the mildest conditions for the plasma treatment. The RF power is set to 12, 15, 8 and 10 W for the treatment of perovskite with Ar, N_2, H_2 (hydrogen generator CINEL RC100) and O_2 plasma, respectively. The chamber pressure Is fixed at 500 mTorr and the gas flow rate is set to 20 sccm. The plasma treatment is performed from a minimum of 2 s to a maximum of 60 s.

Laser-mediated photostability.
Laser-mediated photostability is probed by irradiating the sample at a wavelength of 500 nm, by laser pulses of 7 ns (width) and an average power of 8.4 mW, at a repetition frequency of 20 Hz. Each sample is pumped for 120 min. PL spectra are acquired by exciting the sample at 430 nm, at steps of 20 min, and at an average light intensity of 2.4 mW. The measurements are conducted at room temperature in ambient air.

2.9 References.

[1] Crystallization kinetics modulation and defect suppression of all-inorganic $CsPbX_3$ perovskite films. Junjie Ma, Minchao Qin, Pengwei Li, Liyuan Han, Yiqiang Zhang and Yanlin Song. Energy Environ. Sci. 15 (2022) 413–438.

[2] A general approach to high-efficiency perovskite solar cells by any antisolvent. Alexander D. Taylor, Qing Sun, Katelyn P. Goetz, Qingzhi An, Tim Schramm, Yvonne Hofstetter, Maximillian Litterst1, Fabian Paulus and Yana Vaynzof. Nature Communications 12 (2021) 1878.

[3] Antisolvents in Perovskite Solar Cells: Importance, Issues, and Alternatives. Subrata Ghosh, Snehangshu Mishra, and Trilok Singh. Adv. Mater. Interfaces (2020) 2000950.

[4] One-step synthesis at room temperature of low dimensional perovskite single crystals with high optical quality. Marco Cinquino, Laura Polimeno, Giovanni Lerario, Milena De Giorgi, Anna Moliterni, Vincent Olieric, Antonio Fieramosca, Sonia Carallo, Rosanna Mastri, Vincenzo Ardizzone, Lorenzo Dominici, Dario Ballarini, Cinzia Giannini, Daniele Sanvitto, Aurora Rizzo, Luisa De Marco. Journal of Luminescence 221 (2020) 117079.

[5] Tailoring Crystallization Dynamics of $CsPbI_3$ for Scalable Production of Efficient Inorganic Perovskite Solar Cells Nannan Sun, Sheng Fu, You Li, Lei Chen, Jaehoon Chung, Muhammad Mohsin Saeed, Kshitiz Dolia, Amirhossein Rahimi, Chongwen Li, Zhaoning Song and Yanfa Ya. Adv. Funct. Mater. (2023) 2309894.

[6] Unveiling Property of Hydrolysis-Derived $DMAPbI_3$ for Perovskite Devices: Composition Engineering, Defect Mitigation, and Stability Optimization. Yunhe Pei, Yang Liu, Faming Li,Sai Bai, Xian Jian, Mingzhen Liu. iScience 15 (2019) 165-172.

[7] A Versatile Molten-Salt Induction Strategy to Achieve Efficient $CsPbI_3$ Perovskite Solar Cells with a High Open-Circuit Voltage >1.2 V. Yuqi Cui, Jiangjian Shi, Fanqi Meng, Bingcheng Yu, Shan Tan, Shan He, Chengyu Tan,Yiming Li, Huijue Wu, Yanhong Luo, Dongmei Li and Qingbo Meng. Adv. Mater. 34 (2022) 2205028.

[8] Cs_4PbI_6-Cl Nucleation Seeds Assisted Highly Oriented Inorganic $CsPbI_3$ Perovskites for Efficient Perovskite Solar Cells. Shuang Li, Junming Qiu, Rongshan Zhuang, Qisen Zhou, Mingxu Zhang, Mubing Yu, Yong Hua and Xiaoliang Zhang. ACS Appl. Energy Mater 6 (2023) 3514−3524.

[9] Dark State of the Thiele Hydrocarbon: Efficient Solvatochromic Emission from a Nonpolar Centrosymmetric Singlet Diradicaloid. Angela Punzi, Yasi Dai, Carlo N. Dibenedetto, Ernesto Mesto, Emanuela Schingaro, Tobias Ullrich, Marinella Striccoli, Dirk M. Guldi, Fabrizia Negri, Gianluca M. Farinola, and Davide Blasi. J. Am. Chem. Soc., 145 (2023) 20229−20241.

[10] A review of characterization of perovskite film in solar cells by spectroscopic ellipsometry. H. Li, C. Cui, X. Xu, S. Bian, C. Ngaojampa, P. Ruankham,A. P. Jaroenjittchai. Sol. Energy, 212 (2020), 48.

[11] An Equivalent Circuit for Perovskite Solar Cell Bridging Sensitized to Thin Film Architectures.Yoo, S.-M.; Yoon, S. J.; Anta, J. A.; Lee, H. J.; Boix, P. P.; Mora-Seró, I. Joule, 3 (2019) 2535-2549.

Chapter 3

Bio-derived materials integration in perovskite solar cells.

In this chapter I explore the use of bio-derived materials with different scopes and playing different roles in perovskite-based photovoltaic devices.
In the first part, I report on different uses of β-carotene in a p-i-n device architecture: as an interlayer between the hole transport layer and the perovskite (referred to as the "β-filter") and by incorporating β-carotene into the toluene used as an antisolvent during the perovskite deposition process (referred to as the "β-antisolvent"). β-carotene acts as an antioxidant and a scavenger of reactive species, capturing and neutralizing molecules like superoxide anion ($O_2^{\bullet -}$) and other free radicals. This antioxidant property of β-carotene contributes to the enhanced stability of the perovskite material by reducing oxidative degradation.
The second and third section focus on the very promising polyhydroxyalkanoate family, both used as additives in the perovskite layer or as flexible substrate.
The objective of the chapter is to shine light on the potential biomaterials in perovskite solar cells, reporting different examples of device integration.

3.1 State of the art and premises.

Biologically derived materials (biomaterials) in PSCs hold significant promises for enhancing key aspects of device performance, including charge transport, flexibility, long-term stability, and overall sustainability. Their integration into specific layers of PSCs offers solutions to common challenges in solar cell technology, such as enabling low-temperature, anti-solvent-free processing, and providing added functionalities like flexibility, transparency, and adaptability to unrestrictive operational conditions [1,2]. Biomaterials also play a crucial role in reducing embodied energy, improving sustainability, and fostering circular economy strategies through their low-cost, environmentally friendly, and regenerative properties. Furthermore, they contribute to defect passivation, boosting PCE and enhancing the long-term stability of PSCs, especially when applied to charge transport layers or interfacial layers between the electron transport layer and the active materials [3]. By incorporating biomaterials, PSCs can achieve improved performance and a more sustainable production process, advancing toward a bio-based economy that aligns with circular economy principles [4] (*Figure 3.1*).

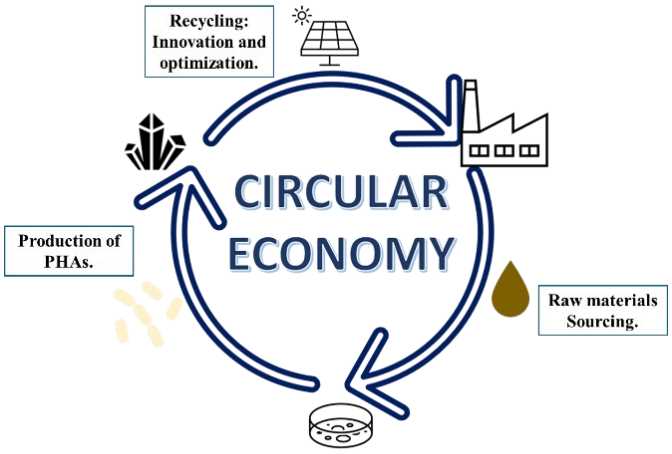

Figure 3.1 Circular Economy for PHB. The process emphasizes waste reduction, resource efficiency, and the regeneration of natural systems, embodying the principles of the circular economy.

3.1.1 Beta-carotene.

Carotenoids are among the most abundant pigments in nature, found in most organisms, including humans, though only plants and microorganisms can synthesize them. Best known for their bright colors, carotenoids have diverse and well-documented functions: they serve as light-harvesting pigments in photosynthetic organisms, covering a unique region of the visible spectrum (380–520 nm) inaccessible to other pigments. Additionally, they efficiently quench singlet oxygen and reactive radicals, interrupting oxidative reaction chains [5].

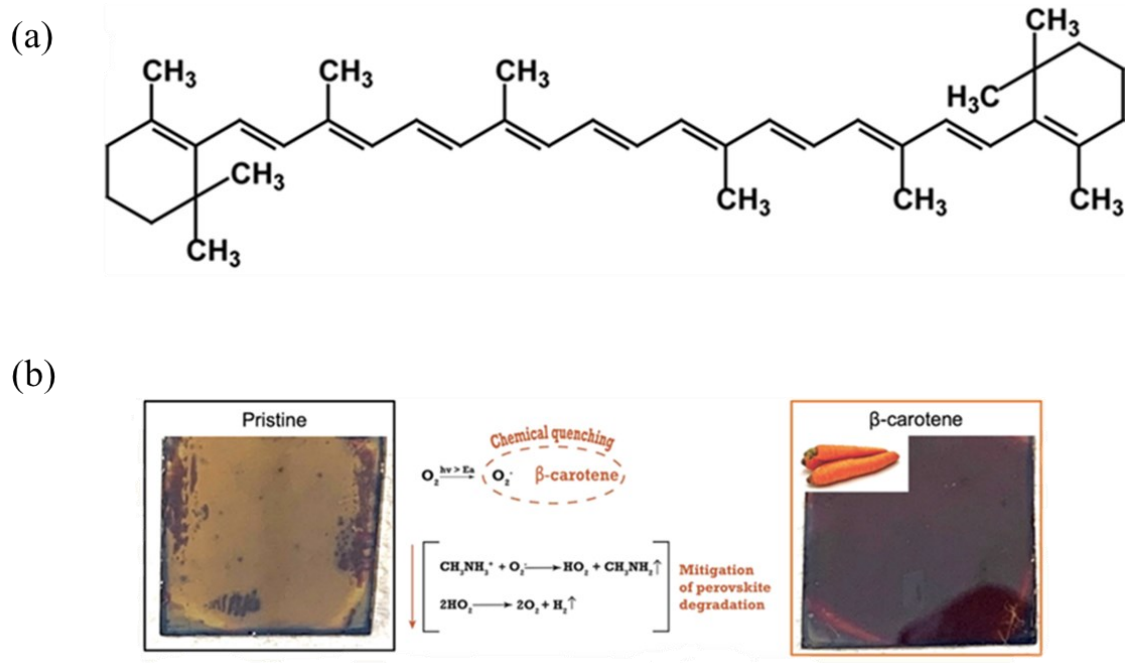

Figure 3.2 (a) Structure of β-carotene consists of eight isoprene units, with conjugation extends to the terminal β-ionylidene rings. (b) Mechanism of chemical quenching between reactive oxygen species generated under illumination and β-carotene.

The unmatched functional diversity of carotenoids arises from their unique molecular structure, a backbone of alternating single and double carbon bonds, forming a conjugated π-electron

system responsible for their spectroscopic and photophysical properties. β-Carotene, one of the most studied carotenoids, shares this characteristic structure, which gives it its distinctive orange color and contributes to its ability to absorb light efficiently in the 400–500 nm range (*Figure 3.2*). These properties enable β-carotene, like other carotenoids, to generate charge carriers upon light excitation and to quench triplet or singlet states through energy or charge transfer, making it particularly useful in the field of renewable energy. β-carotene has shown promise in dye-sensitized solar cells (DSSCs), where it improves light absorption efficiency [6] and in organic field-effect transistors (OFETs) [7]. Other carotenoids have been tested in perovskite solar cells (PSCs) [8], but β-carotene is being tested for the first time in the present work, underscoring the innovative potential of this carotenoid not only in biology but also in the advancement of solar energy technologies.
To leverage the protective properties of β-carotene, in this work it is used to enhance the stability of $MAPb(I_{1-x}Br_x)_3$ (x=0,2) perovskite materials [9]. By incorporating β-carotene as an interlayer in PSCs, degradation caused by reactive species like superoxide (O_2^-) is mitigated, improving the materials' longevity and device performance (*Figure 3.2b*).

3.1.2 Polyhydroxyalkanoates (PHAs).
Polyhydroxyalkanoates (PHAs) are a family of microbial polyesters which comprise of a large family of thermoplastic high-molecular-weight polymers. They are produced by a variety of prokaryotic microorganisms under unbalanced nutrition conditions such as carbon and energy storage materials [10], PHAs accumulate within bacterial cells as intracellular granules (φ ≅ 0.5 μm). These granules can constitute up to 90% of the bacterial dry weight. The exact composition of PHAs varies depending on the bacterial species synthesizing them and the composition of the culture medium. Materials within the PHA family can differ significantly in their chemical structure. The general structure of the repeating unit of PHA is represent here in *Figure 3.3a*, where *n* can be greater than zero and provides the number of repeating units in the polymer chain and *R* represents a functional group in the structure, varying on the type of PHA. PHA and its homopolymer, polyhydroxybutyrate (PHB) are biodegradable and environmentally sustainable biopolymers, hold the potential to replace plastics linear use and dispose practices with a fully circular life-cycle for plastics (*Figure 3.3b*) [4].

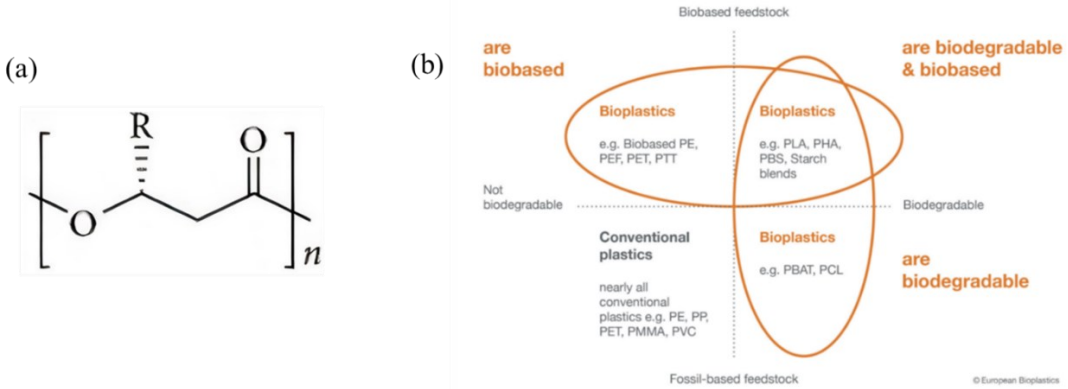

Figure 3.3 (a) Structure of poly-(R)-3-hydroxybutyrate (PHB). (b) Polymers' classification based on their biodegradability and bio-based content [11].

PHB was identified in 1926 by Lemoigne at the Pasteur Institute as a component of the microorganism *Bacillus megaterium,* is a hydrophobic with high crystallinity and melting

temperature, good resistance to organic solvents, and high values of elastic modulus and tensile strength comparable to those of polypropylene (PP), a commercial polymer. However, its elongation at break is significantly lower, ranging between 5% and 10% for PHB compared to 400% for PP. This results in the material's high brittleness and low deformability, and it has a glass transition temperature (Tg) that is too high [12]. Furthermore, its melting temperature is very close to its degradation temperature, making processing with conventional thermoplastic polymer techniques challenging, if not impossible. In literature, PHB is primarily used to produce membranes, owing to its mechanical properties, environmental sustainability, and ease of functionalization. Its application as membranes extends to diverse fields, including filtration, biomedical scaffolding, and even separation technologies in industrial processes.

Table 1 Chemical-Physical specifications of PHB (Egg Plants).

Specific Gravity	1.25
Melt Flow Index	8-15
Yield Stress (MPa)	31-36
Tensile Strength (MPa)	38
Elongation at Break (%)	3.2
Young's Modulus (MPa)	1600-2100
Flexural Modulus (MPa)	2500-3200
Vicat Softening Temperature (°)	164
Izod Impact (J/m)	50-65
Heat Deflection Temperature (°)	135-145
DSC Melting Point (°)	175-180

In this work, the PHB used was supplied by the company *Egg Plant*. They obtain the PHB through bacterial fermentation (using *Haloferax mediterranei*) as an intracellular product from the wastewater of dairy industries. The wastewater undergoes a cascading filtration process that separates solids from liquids. The liquid can be reused, while the organic component undergoes enzymatic hydrolysis, releasing flavonoids (which are valuable in the cosmetic industry) and other organic materials. This organic material is then fermented to produce PHB. Bacterial fermentation is a highly scalable process, with high potential for implementation in the large-scale production of PSC modules. The chemical-physical specifications of the PHB, essential for characterizing its properties and assessing its suitability for experimental purposes, are reported in Table 1.

3.2 Experimental results: β-carotene for Improved Photostability in Wide-Band-Gap Perovskite Solar Cells.

As previously mentioned, β-carotene is used in these two approaches: (i) as an interlayer between the hole transport layer and the perovskite (referred to as the "β-filter") and (ii) incorporated into the toluene used as an antisolvent during the perovskite deposition process (referred to as the "β-antisolvent") on the wide band gap perovskite $MAPb(Br_{0.2}I_{0.8})_3$. The p-i-n device architecture and the fabrication conditions are detailed in Chapter 2.

3.2.1 Morphological Analysis.

$MAPb(Br_{0.2}I_{0.8})_3$ absorption spectra are analyzed, and the optical Eg of the perovskite is estimated using the Tauc plot method. The resulting value is approximately 1.74 eV, aligning closely with literature reports [13,14], with the presence of β-carotene showing a negligible

effect on the band gap (*Figure 3.4a*). Morphological analysis conducted using SEM reveal significant improvements in both perovskite films treated with β-carotene. Compared to the reference films (*Figure 3.4b,c*), the β-filter (*Figure 3.4d,e*) and β-antisolvent (*Figure 3.4f,g*) treated samples exhibit a more uniform and compact morphology with reduced pinholes and smoother surfaces. The good quality of the perovskite developed with the β-antisolvent and β-filter approaches was also confirmed by an X-ray diffraction analysis (*Figure 3.4h*), showing a complete crystallization process with sharp peaks characteristic of perovskite materials, which are critical for optimizing the overall quality and stability of the perovskite layer.

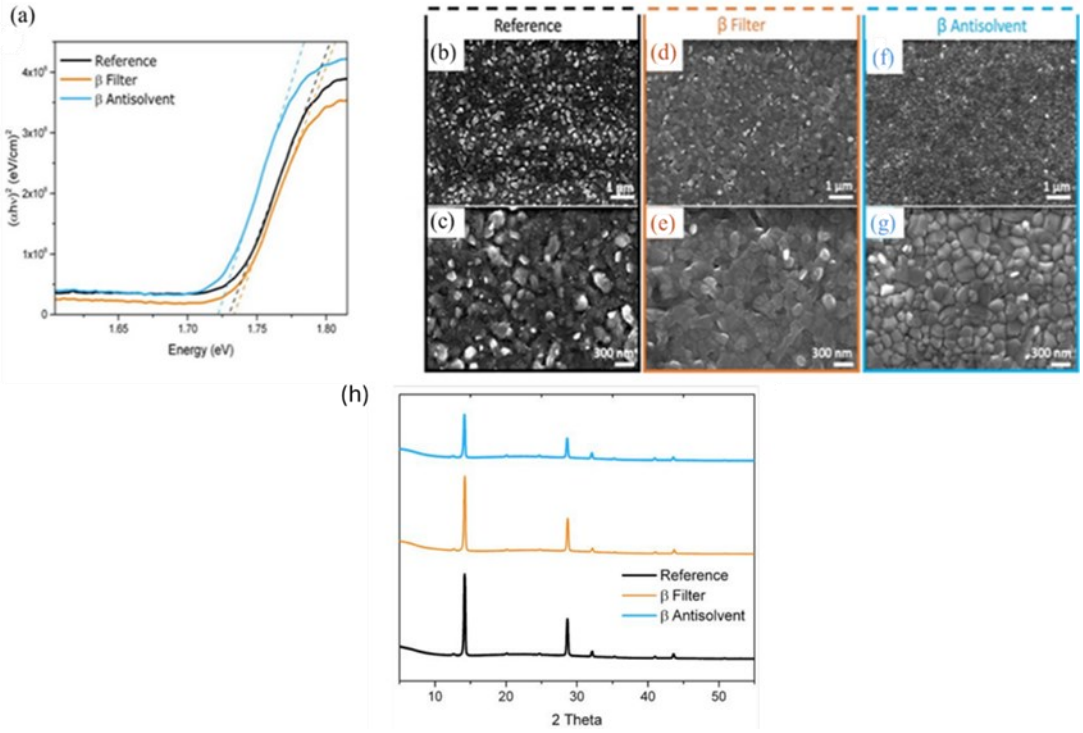

Figure 3.4 a) Energy Gap calculation. Tau plot method applied for the estimation of the optical energy gap. SEM images of reference perovskite film at (b) low and (c) high magnification, β-filter perovskite at (d) low and (e) high magnification, and β-antisolvent perovskite at (f) low and (g) high magnification. h) XRD pattern of reference and β additivated perovskite films.

3.2.2 Laser-Mediated Photostability.

The stability of the perovskite films under stress conditions is evaluated using a laser-mediated photostability (LMPS) test. Perovskite films are exposed to a pulsed laser source at a wavelength of 500 nm, with a frequency of 20 Hz, a pulse width of 7 ns, and an average power of 8.4 mW, under ambient conditions without encapsulation. Irradiation is performed for 2 hours, and photoluminescence (PL) spectra are recorded every 20 minutes using excitation at 430 nm with a power intensity of 2.4 mW. Analysis of the PL spectra highlighted significant differences between reference perovskite samples and those incorporating β-carotene. Unlike mixed-halide perovskites, which typically exhibit a red shift in the PL emission peak after light exposure, according to the mechanism described in Section 1.5, the reference samples show a pronounced and irreversible blue shift (*Figure 3.5a*). This behavior can be attributed to the nature of the Pb−I and Pb−Br bonds [15,16]; the longer and weaker Pb−I bond is more

susceptible to disruption under illumination, leading to the formation of bromine-rich optical emitters and resulting in the observed blue shift.
In the presence of β-carotene, used as a filter or as an antisolvent, the perovskite is protected; in fact, the PL blue shift is remarkably reduced (*Figure 3.5b-c*).

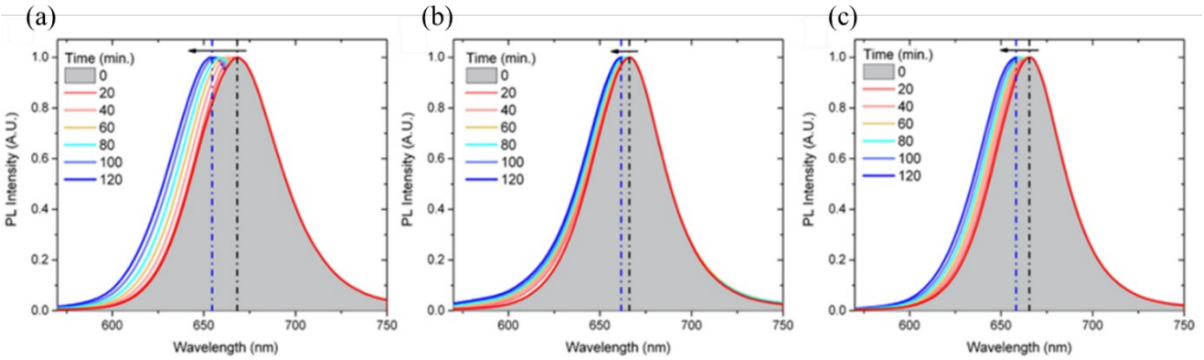

Figure 3.5 Laser-mediated photostability analysis of (a) reference, (b) β-filter, and (c) β-antisolvent perovskite under a 500 nm pulsed laser with PL spectra acquired at steps of 20 min.

The β-carotene possesses a chemical structure rich in C=C double bonds, which play a central role in the protection against photooxidation. Leading, in this context, to better stability of the perovskite material when exposed to laser irradiation in ambient air.

3.2.3 Advanced Characterization Techniques

To further study and validate the approach, a different stress tests are conducted, involving the exposure of perovskite films to a strong oxidizing environment rich in ozone (O_3) and superoxide anions (O_2^-). The impact on the perovskite samples is evaluated using ATR-FTIR, spectroscopic ellipsometry and TRPL. For this purpose, a UV-light bromograph is adapted to expose the samples to a treatment (referred to as UVO treatment), resulting in simultaneous exposure to UV, O_3, and O_2^-. It has been recently demonstrated that these conditions contribute to perovskite material degradation [17], as discussed in Section 1.5.

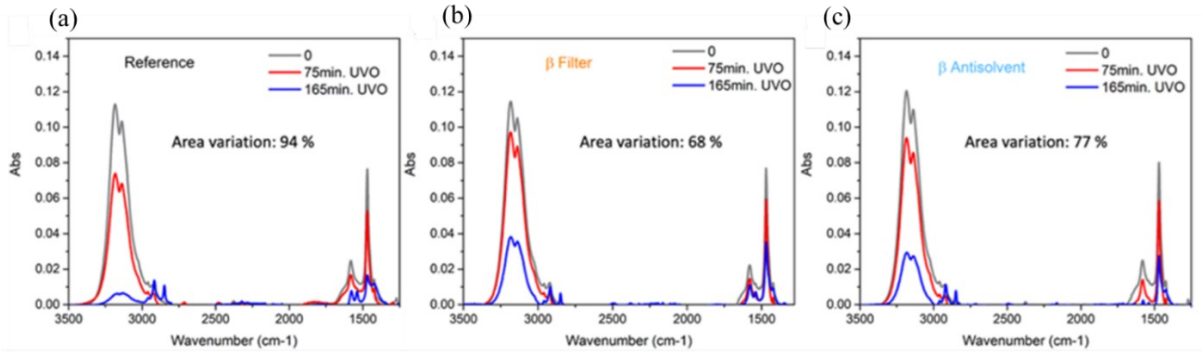

Figure 3.6 ATR-FTIR analysis. Spectra and area percentage reduction of (a) reference, (b) β-antisolvent, and (c) β-filter films deposited on glass exposed to UVO for 0, 75, and 165 min.

ATR-FTIR analysis is used to monitor the degradation process, with the signal related to N-H stretching and bending showing a decrease as methylammonium is lost. Comparing the ATR-FTIR of fresh samples and those subjected to the stress tests for 165 min, it is evident that the intensity of the band corresponding to the asymmetric 3184 cm^{-1} and symmetric 3139 cm^{-1}

vibrational stretching of N-H decreases rapidly in the case of the reference (*Figure 3.6a*) compared to the samples including β-carotene (*Figure 3.6b,c*). The signal loss confirms the extraction of a proton from the methylammonium cation by superoxide radicals ($O_2^{\bullet-}$), resulting in the formation of the hydroperoxyl radical ($HO_2^{\bullet}$). The percentage decreases of the area, from 0 to 165 min of stress test, beneath the asymmetric and symmetric vibrational stretching of N-H signals, are calculated for all samples, resulting in 94%, 68%, and 77% for the reference, β-filter, and β-antisolvent, respectively. Furthermore, the peaks of symmetric 1469 cm^{-1} and asymmetric 1579 cm^{-1} vibrational bending [18,19] after 165 min of the test are much less reduced in the case of the β-antisolvent and β-filter compared to the reference.

TRPL measurements are performed to examine the carrier lifetime of the reference, β-filter, and β-antisolvent perovskites, with the specific aim of assessing the optical quality of the films following exposure to oxidizing agents. The TRPL spectra for the samples at 0 minutes, after 75 minutes, and after 165 minutes of UVO treatment. For the reference perovskite, a significant reduction in carrier lifetime is observed after just 75 minutes, followed by a sharp decline after 165 minutes (*Figure 3.7a*). In contrast, the β-filter and β-antisolvent perovskites display markedly different behavior. The β-filter perovskite shows a slightly prolonged TRPL signal after 75 minutes of exposure (*Figure 3.7b*) compared to the reference, but this advantage diminished after 165 minutes, resulting in a decline like that of the reference. This behavior is likely because the β-carotene layer is located beneath the perovskite film, leaving the surface unprotected against oxidizing agents. By comparison, the β-antisolvent perovskite demonstrate a remarkable outcome. Even after 165 minutes of continuous UVO stress (*Figure 3.7c*), it maintains strong resistance, with its optical properties only slightly affected, as evidenced by the minimal TRPL decay.

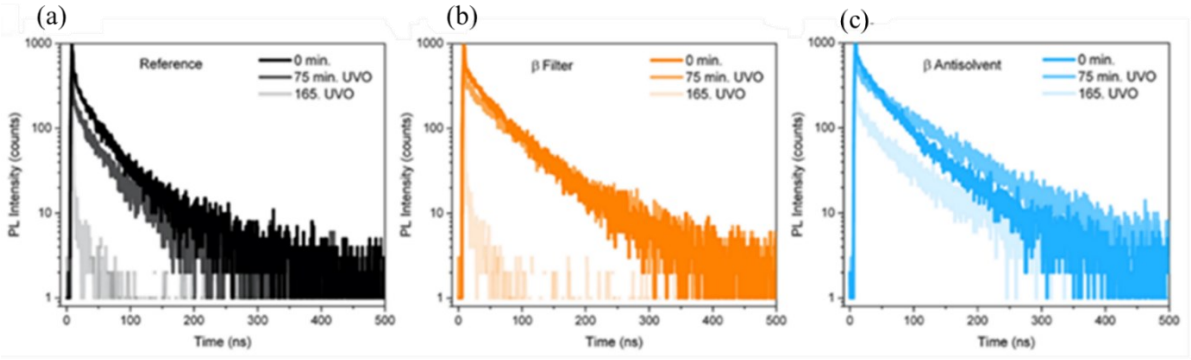

Figure 3.7 TRPL and decay analysis conducted throughout UVO: (a) reference, (b) β-filter, and (c) β-antisolvent perovskite films PL analyzed at 0 min and after 75 and 165 min of UVO stress test.

3.2.4 Device Integration.

Following the improvement in material stability, the integration of the devices is carried out to assess whether the β-filter and β-antisolvent approaches could also be compatible with achieving a high PCE. The impact of the β- carotene deposition layer on device characteristics is investigated using a p–i–n cell stack: glass/indium tin oxide (ITO)/2PACZ/MAPb($Br_{0.2}I_{0.8}$)$_3$/PCBM/BCP)/silver (Ag). The choice of the p-i-n architecture, offers several key advantages, some of which have been discussed in Section 1.7. This configuration enhances charge extraction and reduces non-radiative recombination losses at critical interfaces, ultimately leading to higher V_{OC} and greater PCE [20].

The results demonstrate satisfactory performance, surpassing those of reference devices containing $MAPb(Br_{0.2}I_{0.8})_3$, as summarized in Table 2, which presents both the highest-performing results and the average values from 40 devices.

Table 2 Photovoltaic Performance of p-i-n Devices Based on Reference, β-Filter, and β-Antisolvent Perovskites[a].

$MAPb(Br_{0.2}I_{0.8})_3$	FF	Voc (V)	Jsc (mA/cm^2)	PCE (%)
Reference	78 ± 2	1.14 ± 0.05	18 ± 2	16 ± 2
	81.1	**1.201**	**18.85**	**18.36**
β Filter	78 ± 2	1.15 ± 0.03	20 ± 1	18 ± 1
	78	**1.201**	**21.73**	**20.26**
β Antisolvent	78 ± 2	1.15 ± 0.03	20 ± 2	17.6 ± 1.3
	79	**1.195**	**21.1**	**19.91**

[a] For each kind of device, the average values (first lines) and best performances (second lines) are given. Values are from 40 devices of different batches.

A PCE approaching 20% and a V_{oc} value of 1.2 V are achieved with both β-antisolvent and β-filter device configurations. The V_{oc} and FF values remain largely unchanged with the inclusion of β-carotene, while an increase in short-circuit current is observed, as clearly illustrated by the J–V curves (*Figure 3.8a*). The PCE values obtained, free from hysteresis, represent some of the highest results reported for a mixed halide (I-Br) perovskite with a bandgap of 1.74 E_g [21].

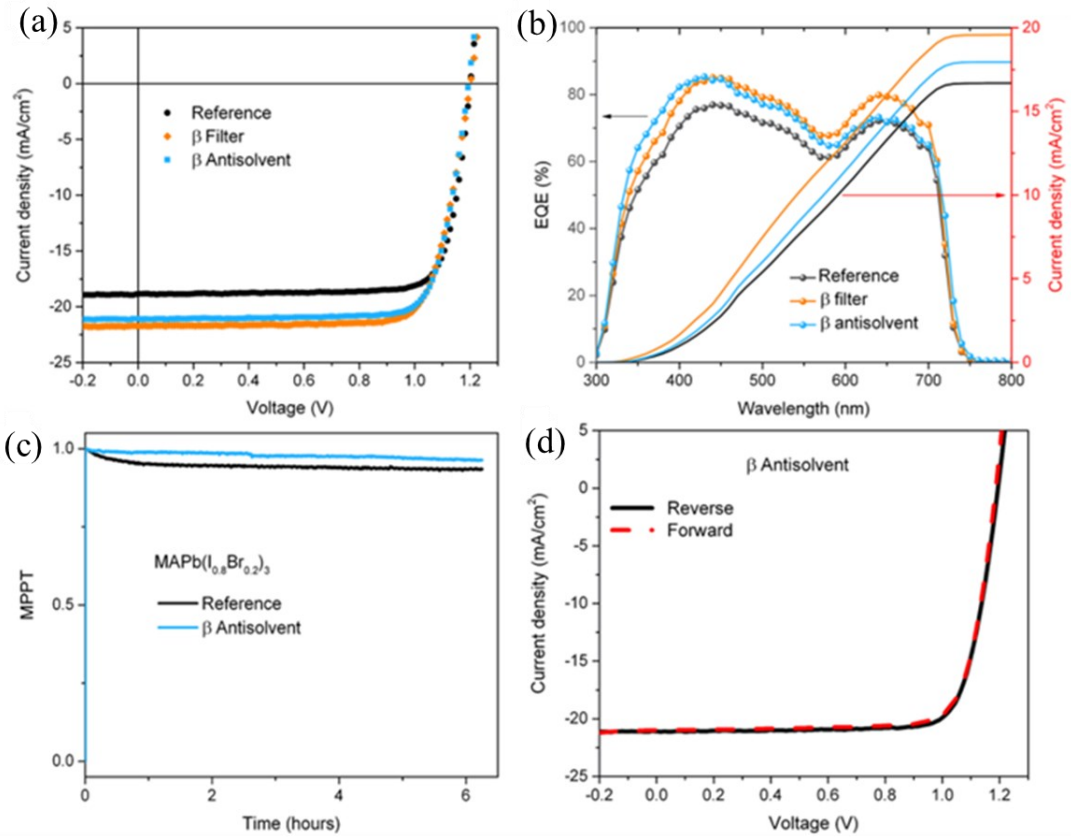

Figure 3.8 (a) J–V curves of reference, β-filter, and β-antisolvent perovskite-based devices acquired in reverse condition and (b) their EQE spectra with integrated currents. (c) MPPT of reference- and β-antisolvent-based devices. (d) J–V scans in both reverse and forward conditions of β-antisolvent.

To further verify the photocurrent enhancement, EQE spectra are recorded (*Figure 3.8b*) revealing the well-matched current density to the J_{sc} from J–V curves for all devices. Moreover, the iodide PSCs feature higher absorption at the long-wavelength region and confirms by the EQE analysis of all samples [22]. The combination of β-carotene's broad absorption spectrum in the blue and green regions with its luminescent down-shifting (LDS) properties could offer potential benefits for enhancing photovoltaic devices. β-carotene absorbs high-energy photons and re-emits light at longer wavelengths, which may improve the light absorption across a wider spectral range [23]. This dual effect, acting both as a spectrophotometric filter and through LDS, could lead to an increase in EQE across the entire spectral range. This approach might contribute to improved charge generation and overall device performance, as suggested by recent studies on multifunctional luminescent down-shifting films [24].The higher J_{sc} values can be attributed to the improved morphology of the β-carotene-modified perovskite films, which exhibit larger, cohesive grains and fewer pinholes compared to the reference perovskite films. It is well established that a more uniform and less defective perovskite morphology plays a crucial role in reducing current leakage and enhancing the J_{sc} values of the resulting solar cells [25]. To the best of our knowledge these hysteresis-free, the PCE values are among the highest values reported for a mixed halide (I-Br) perovskite with a band gap of 1.74 eV [26]. Measurements of the maximum power point tracking (MPPT) are also conducted to check the device stability under working operations. The β-antisolvent perovskite has a better performance compared to the reference perovskite, also showing an extraordinary absence of hysteresis (*Figure 3.8c,d*).

3.3 Experimental results: PHB as additive for perovskite growth and integration in pin solar cells.

We introduce PHB into the perovskite solution, to explore its use as an additive in the active layer of perovskite. The aims are multiple: to assist the crystal growth facilitating the deposition process and improve the mechanical properties of the film due to the polymer's action, and secondly, to passivate the grain boundary defects of the absorber material, improving its optoelectronic properties and consequently the conversion efficiency of the final device. PHB is an ideal candidate due to the presence of -COOH groups [27], which, as highlighted in previous literature on $MAPbI_3$ as a passivating agent [28]. Furthermore, the hydrophobic alkyl chain of PHB ensures greater resistance to humidity and prevents the decomposition of perovskite in the air.

The goal of the work is to introduce it into the precursor salt perovkite solution ($FAPbI_3$, FAPI) so that there can be an interaction, leading to the formation of a macromolecular adduct between the C=O group, Pb^{2+}, and NH^{3+}, resulting in a reduction of trap states. This procedure requires optimization in terms of solvents, given the poor solubility of PHB in the common solvents used for perovskites, as well as optimization in terms of its mass percentage in the solution.

3.3.1 Morphological Analysis.

PHB is tested at two concentrations: 0.1mg/mL and 0.05 mg/mL in perovskite solution. The SEM images (*Figure 3.9*) of the FAPI films with and without the PHB additive reveal important insights into the effects of PHB on the perovskite film's morphology. The FAPI reference film,

lacking PHB, displays a significant void density, suggesting the presence of surface defects and porosity.

In contrast, the FAPI-PHB0.05 shows a noticeable improvement in its morphology. The film has fewer defects and larger grains compared to the reference, suggesting that the PHB additive is playing a crucial role in passivating surface defects, particularly at the grain boundaries, and enhancing the crystalline growth. The larger grain sizes are indicative of more ordered crystal formation, which can lead to better film quality. At this lower concentration, PHB likely interacts with the perovskite, stabilizing the FA^+ cation and helping to passivate defects, thus promoting more homogeneous and efficient crystal growth.

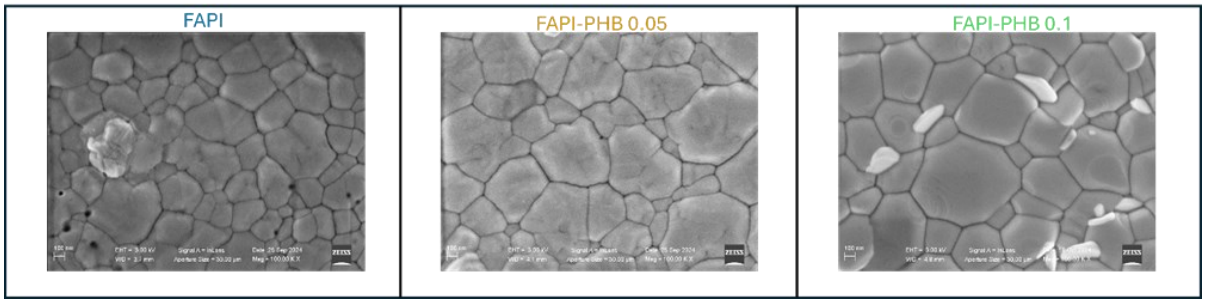

Figure 3.9 SEM images of FAPI films, morphological comparison of FAPI reference, FAPI-PHB0.05 and FAPI-PHB0.1.

However, at a higher concentration of PHB (0.1 mg/ml), the film becomes noticeably smoother, with even larger grains, but also shows the formation of white granules arranged vertically within the polycrystalline structure. These white granules could indicate the presence of a non-perovskite phase or PHB precipitates within the perovskite matrix. The vertical alignment of these granules suggests a preferred growth direction, which might interfere with the perovskite structure. At this higher concentration, PHB appears to saturate the perovskite film, potentially disrupting optimal crystal growth. The presence of these white granules may indicate that excessive PHB interferes with the crystalline structure, either through incomplete dissolution or the formation of incompatible phases within the perovskite matrix.

3.3.2 Optical properties.

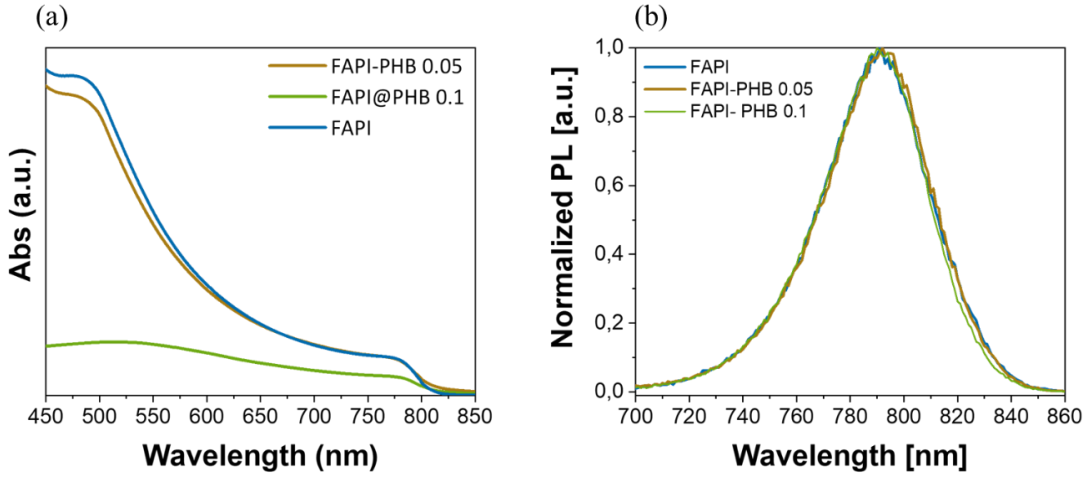

Figure 3.10 (a) UV-VIS absorption spectra and (b)Normalized PL of FAPI reference, FAPI-PHB0.05 and FAPI-PHB0.1.

Strong optical absorption is observed in the wavelength range of 450–850 nm. An estimation of the optical bandgap of FAPI films, was made using a plot of $(\alpha h\nu)^2$ vs hν (Tauc method), by extrapolation of the linear region of the absorption edge to the energy axis, with the intercept indicating a direct bandgap of 1.53 eV, which is in a good agreement with the previously reported literature values [29,30], revealing that the polymers did not affect the bandgap energy of these films (*Figure 3.10a*). To get more insight into the photophysical properties, the Urbach energies (E_u) of the perovskite films prepared without and with the PHBs are calculated according to the Urbach law [31] (equation 3.1):

$$\alpha = \alpha_0 exp\left(\frac{E-Eg}{E_U}\right) \tag{3.1}$$

where α is the absorption coefficient and E is the photon energy. E_u values of 9.47, 7.52, 13.1 meV were calculated for reference-FAPI, FAPI-PHB0.05, FAPI-PHB0.1 respectively. The E_u of the perovskite film is generally affected by the long-range structure disorder and defects of the films [32] in which the film with better crystallinity and fewer defects could result in smaller E_u values. Therefore, the decreased E_u value of the perovskite films, especially in FAPI-PHB0.05, could be ascribed to the improved crystallization with fewer defects in the film. The normalized PL spectra (*Figure 3.10b*) do not show any shift in emissions for PHB concentrations of 0.1 mg/ml, 0.05 mg/ml, and the reference FAPI sample, indicating that the addition of PHB at these concentrations does not significantly alter the bandgap or the intrinsic optical properties of the perovskite material.

The ATR-FTIR spectra (*Figure 3.11a*) of FAPI films, with and without the PHB additive, exhibit the characteristic stretching vibration of C=N from FA^+ at 1712 cm^{-1}. Additionally, the peaks observed at 3268 cm^{-1} and 3401 cm^{-1} correspond to the N–H stretching vibrations of FA^+ [33]. Notably, the film FAPI-PHB0.05 shows a more intense stretching peak of formamidinium compared to the reference FAPI film, while the FAPI-PHB0.1 exhibits the lowest intensity of all the peaks. These observations can be rationalized by considering the dual role of PHB as a defect passivator and a potential disruptor of lattice stability at higher concentrations.

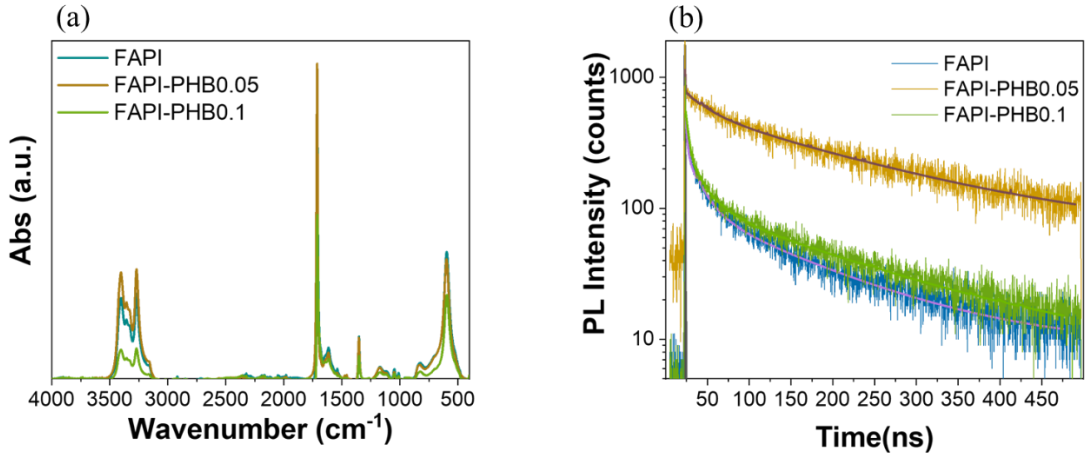

Figure 3.11 (a) ATR-FTIR analysis and (b) TRPL and decay analysis of FAPI-reference, FAPI-PHB0.05 and FAPI-PHB0.1.

At low concentrations (0.05mg/ml in perovskite solution), PHB likely interacts with the perovskite grain boundaries, passivating surface defects and stabilizing the FA^+ cations. This passivation improves the crystalline order (*Figure 3.9*), thereby amplifying the vibrational signal associated with the NH_2 stretching mode of FA^+ cations. In contrast, at higher concentrations (0.1mg/ml), PHB appears to saturate the surface and potentially disrupt the lattice structure. This can lead to a reduction in the mobility of FA^+ cations or a weakening of their interaction with the surrounding iodide octahedra. The diminished intensity of the stretching mode suggests that the FA^+ vibration becomes less pronounced, possibly due to the introduction of additional disorder or strain in the lattice. TRPL measurements are conducted on three perovskite samples: pure FAPI, FAPI-PHB0.05 and FAPI-PHB0.01 (*Figure 3.11b*). The average carrier lifetime is estimated for FAPI reference 60.5 ns, suggesting that rapid recombination might occur due to defects and grain boundaries. For the PHB 0.05 sample, the lifetime increases to 152 ns, which could indicate that PHB is passivating defects and stabilizing the FA^+ cations, potentially reducing recombination. However, for the PHB 0.1 sample, the carrier lifetime decreases to 105 ns, which might suggest that an excess of PHB could lead to the saturation of passivation sites or induce structural distortions, potentially limiting carrier mobility. These results imply that PHB at 0.05 mg/ml could be optimal for improving carrier lifetime, while higher concentrations might have a negative effect.

3.3.3 Device integration.

To assess the impact of the PHB polymer on the FAPI perovskite film at different concentrations, a p–i–n cell stack is constructed with the following layers: glass/ITO/MeO-2PACZ/$FAPbI_3$(-PHB)/C_{60}/BCP/Ag (*Figure 3.12a*).

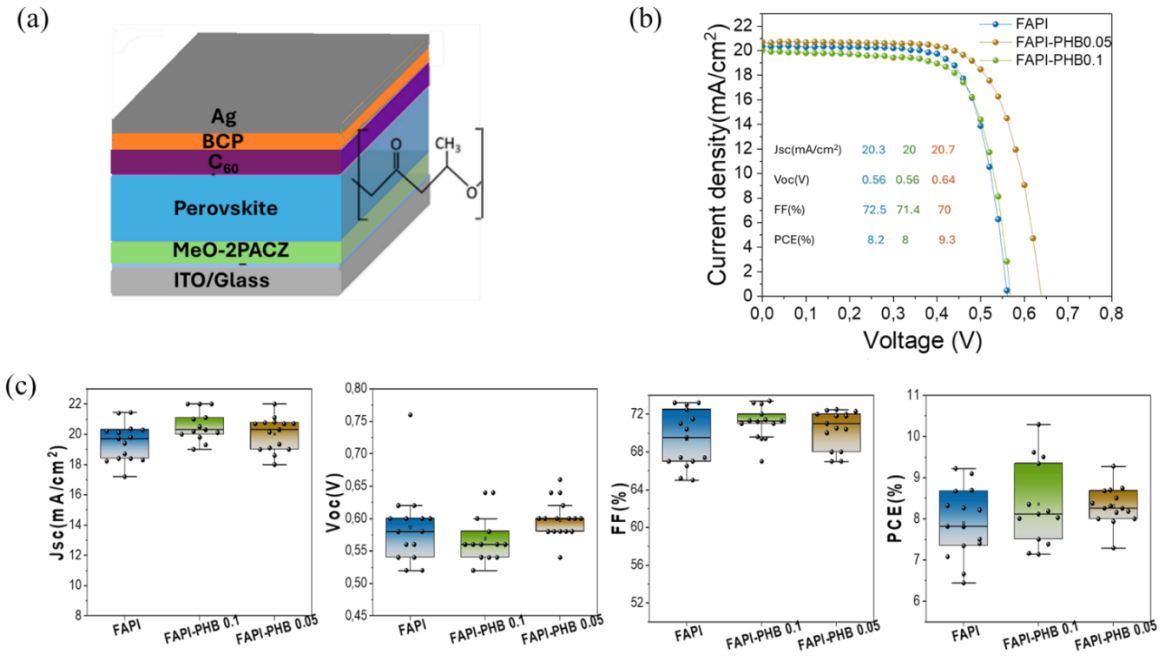

Figure 3.12 (a) Stack cell glass/ITO/MeO-2PACZ/$FAPbI_3$(-PHB)/C_{60}/BCP/Ag. (b) J-V curves and (c) statistical parameters of FAPI-reference, FAPI-PHB0.05 and FAPI-PHB0.1.

Figure 3.12b,c presents the J-V curves and the statistical analysis of photovoltaic performance across 14 devices. The devices were characterized without encapsulation, with RH of 40%.

Based on the statistical data, it is clear that the FAPI-PHB 0.05 device outperforms the reference, achieving the best photovoltaic performance with a PCE of 9.3%. Although this value is below the current state-of-the-art, it is important to highlight that the device is not yet fully optimized. This result indicates a promising potential for further improvement in efficiency with continued development and optimization of the materials and device architecture [34]. In contrast, for the FAPI-PHB0.1 device, the V_{oc} is the lowest value observed. This reduced V_{oc} can be attributed to the previously discussed structural and optoelectronic effects of the higher PHB concentration. The formation of white crystalline regions seen in SEM images (*Figure 3.9*) for PHB 0.1 could correspond to δ-phase perovskite or other secondary phases, which are non-photoactive and act as recombination centers, further lowering the Voc. In contrast, the FAPI-PHB 0.05 device benefits from improved grain size and reduced defects at grain boundaries, leading to better charge carrier lifetimes and reduced recombination losses, as indicated by TRPL measurements (*Figure 3.11b*).

To further confirm the beneficial effect of the PHB polymer as an additive, the same test is conducted using Cs-based perovskite. This approach aims to evaluate whether the positive impact of PHB observed in the FA-based perovskite could be generalized to other perovskite compositions. By extending the study to a fully inorganic perovskite, it was possible to assess the versatility of PHB in enhancing the structural and optoelectronic properties of different perovskite systems. As shown in *Figure 3.13a,b*, the incorporation of PHB at a concentration of 0.05 mg/ml has a beneficial effect on all photovoltaic parameters. The SEM image (*Figure 3.13c*) further corroborates this observation by revealing a more compact and uniform morphology of the perovskite film with PHB 0.05. Enhanced film quality likely reduces defect densities and improves charge transport across the active layer, thereby contributing to the overall superior performance of the device. These findings highlight the positive role of PHB as an additive in optimizing both the structural and optoelectronic properties of perovskite films.

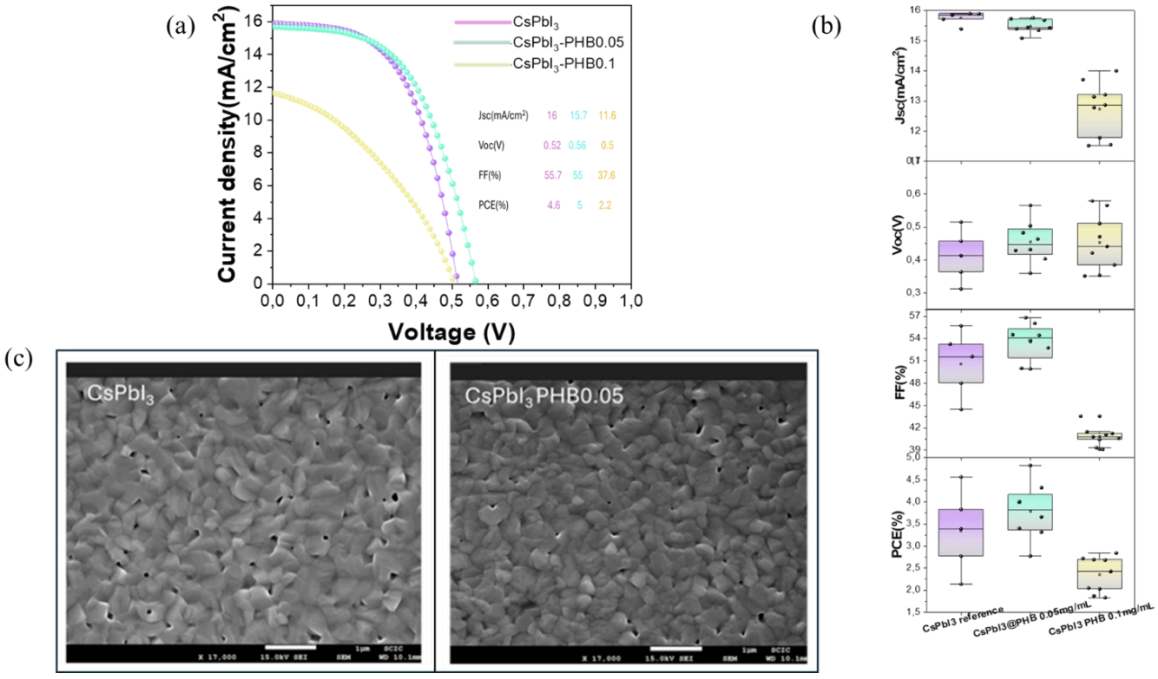

Figure 3.13 (a) J-V curves and (b) statistical parameters of $CsPbI_3$ reference, $CsPbI_3$-PHB0.05 and $CsPbI_3$-PHB0.1. (c) SEM images of $CsPbI_3$ reference and $CsPbI_3$-PHB0.05.

3.4 Experimental results: processing of PHB as flexible substrate for photovoltaic devices.

This section focuses on the use of PHB as a flexible substrate, to evaluate its synergistic effect both as a substrate and as a template for the FAPI perovskite. This approach aims to assess how PHB can enhance the properties of the perovskite material, benefiting from its mechanical flexibility while also promoting the growth of the perovskite crystals.

The films are prepared using the solvent-casting method. This approach involves dissolving a specific amount of polymer in a solvent, followed by the evaporation of the solution in a Petri dish. Typically, the dissolution process requires a certain amount of time, which depends on the intrinsic solubility of the polymer in the chosen solvent as well as the temperature and degree of mixing applied. The subsequent evaporation can occur at a temperature different from that used for dissolution. The most commonly used solvent for polymers belonging to the PHA family is chloroform ($CHCl_3$). In this solvent, the solubility, in terms of mg of polymer dissolved per mL of solvent, can reach quite high values, on the order of 50 mg/mL. This, combined with its low boiling point and high volatility, makes $CHCl_3$ an excellent solvent for preparing PHA-based films using the solvent-casting method. The first parameter to define is the diameter of the Petri (30mm in the work) dishes to be used, and therefore the area of the final film. The filling degree of the Petri dish is closely related to the amount of polymer required to obtain a film of a certain thickness, which also determines the evaporation time, as both depend on the solubility of the polymer in the chosen solvent. The choice of evaporation temperature is determined by the desired evaporation rate, which must ensure the formation of a homogeneous film without defects, considering its application as a possible flexible substrate.

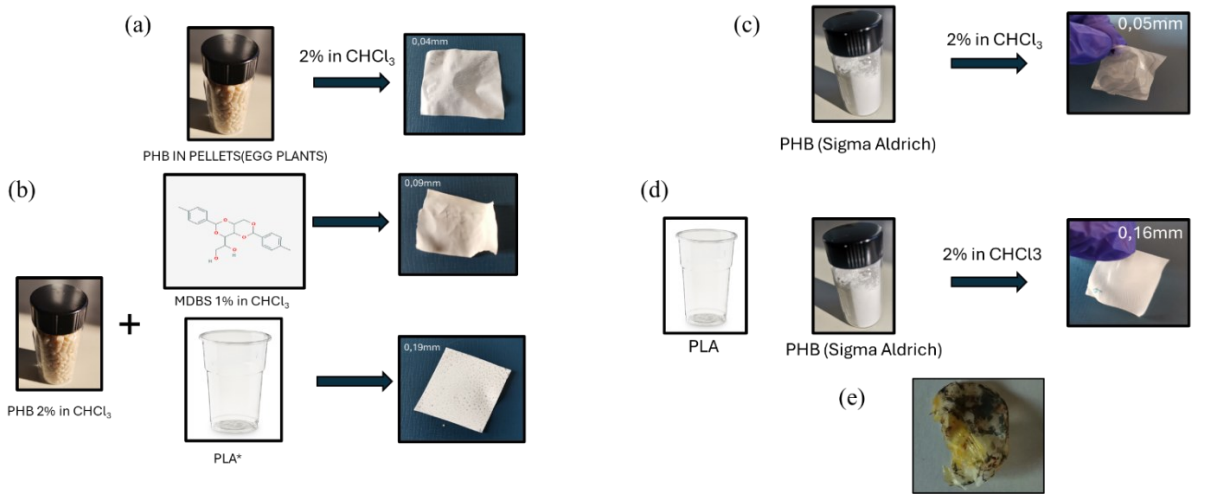

Figure 3.14 (a) Starting materials (pellets) and the resulting films with thicknesses of 0.04 mm, obtained through intermediate processing step (casting). (b) Starting materials (pellets) and the resulting films with thicknesses of 0.09 mm and 0.19mm (steps blending/casting) obtained with addition of MDBS and PLA respectively. (c) Starting materials (powder) and the resulting films with thicknesses of 0.05 mm, obtained through intermediate processing step (casting). (d) Starting materials (powder) and the resulting films with thicknesses 0.16mm (steps blending/casting) obtained with addition of PLA. (e) Perovskite deposition on flexible PHB substrate.

The initial deposition of PHB results in an opaque film that was not only too thin (0.04 mm) but also unsuitable for use as a flexible substrate, as it lacked the required transparency. To increase the thickness and improve the material's mechanical properties, blending techniques are explored. These included the addition of plasticizers, such as 1,3:2,4-Bis-O-(4-

methylbenzylidene)-D-sorbitol (MDBS), or incorporating the Polylactic Acid (PLA) biopolymer to enhance flexibility. Although this led to an increase in film thickness (0,09 and 0,19 mm respectively), it does not result in a significant improvement in transparency (*Figure 3.14a,b*).

To further investigate the film's properties, a comparison is made with a commercial PHB powder, which showed better overall film quality (*Figure 3.14c,d*). However, the film produced from commercial PHB was not homogeneous, mainly due to the dominance of the amorphous component of the polymer [35]. While this offered some improvement in the film's structural integrity, the lack of uniformity still posed a challenge for consistent film formation.

The rigid amorphous fraction in the PHB negatively influences the material's performance, which became particularly evident during the deposition of the perovskite layer. The PHB film shows signs of shrinkage upon the perovskite deposition process, indicating a lack of sufficient mechanical stability and thermal resistance (*Figure 3.14e*). This contraction further highlights the reduced mechanical and thermal properties of the PHB material, which are not suitable for the deposition steps required for the fabrication of high-quality photovoltaic devices. Thus, despite the improvements in thickness and substrate planarization, the poor thermal and mechanical stability of the PHB-based films render them unsuitable for flexible, high-performance devices.

3.5 Conclusions.

In this chapter a comprehensive strategy to enhance the stability and performance of different perovskites solar cells by employing bio-inspired and biocompatible additives: β-carotene and PHB is presented. Both additives demonstrate significant potential to improve the morphology, stability, and optoelectronic properties of perovskite films through distinct mechanisms.

The integration of β-carotene, inspired by natural photosynthetic processes, effectively mitigates perovskite degradation by scavenging oxidizing species generated during device operation. The β-antisolvent-treated perovskite has showed superior resistance to oxidative stress, as evidenced by enhanced charge carrier lifetimes, better preservation of the absorption spectrum observed through spectroscopic ellipsometry and has sustained molecular stability confirmed by ATR-FTIR analysis. These results indicate that the integration of β-carotene effectively counteracts the oxidative damage to the perovskite layer, leading to improved overall material robustness under harsh conditions. The β-antisolvent incorporation strategy improves perovskite stability, as evidenced by enhanced charge carrier lifetimes, preserved optical absorption, and sustained molecular integrity. Devices constructed with β-carotene-treated perovskite achieve a PCE of approximately 20%, marked by a high open-V_{oc} of 1.2 V, demonstrating the compatibility of this approach with high-performance solar cell fabrication.

Similarly, PHB as an additive and flexible substrate addresses challenges in perovskite film morphology and mechanical flexibility. At optimized concentrations (0.05 mg/mL), PHB enhances crystalline quality and reduces surface defects, leading to improved grain size, lower Urbach energy, and extended charge carrier lifetime. Devices incorporating FAPI-PHB0.05 achieve a PCE of 9.3%, surpassing the reference devices. However, higher PHB concentrations (0.1 mg/mL) induce non-perovskite phases, underscoring the need for precise optimization. PHB is also explored as a flexible substrate. The findings underscore the need for optimal PHB concentrations to balance crystallinity improvements and defect passivation without forming

unwanted phases. Future research should explore other PHA derivatives or crosslinking agents to further enhance the mechanical and optoelectronic properties of perovskite films, as well as investigate PHB's role in flexible solar cells under real-world conditions.

Together, these results highlight the complementary roles of β-carotene and PHB in addressing key limitations of perovskite solar cells. While β-carotene enhances chemical stability and device efficiency, PHB contributes to improved morphology and mechanical robustness. This dual approach reinforces the potential of leveraging bio-inspired and biodegradable materials to develop stable, efficient, and flexible perovskite-based photovoltaics. Future investigations should focus on exploring other synergistic bio-additives and further optimizing their integration into scalable device architectures.

3.6 References.

[1] Advances in stability of perovskite solar cells. Qamar Wali, Faiza Jan Iftikhar, Muhammad Ejaz Khan, Abid Ullah, Yaseen Iqbal, Rajan Jose. Org. Electron., 78 (2020) 105590.

[2] Nonfullerene electron transporting material based on naphthalene diimide small molecule for highly stable perovskite solar cells with efficiency exceeding 20%. S.-K. Jung, J.H. Heo, D.W. Lee, S.-C. Lee, S.-H. Lee, W. Yoon, H. Yun, S.H. Im, J.H. Kim, O.P. Kwon. Adv. Funct. Mater., 28 (2018) 1800346.

[3] The prospects of biologically derived materials in perovskite solar cells. Edwin T. Mombeshora, Edigar Muchuweni, Alexander J. Doolin, Matthew L. Davies, Bice S. Martincigh, Vincent O. Nyamori. Appl. Materials Today. 40 (2024) 102406.

[4] Life cycle assessment of recycling strategies for perovskite photovoltaic modules. Xueyu Tian, Samuel D. Stranks and Fengqi You. Nature Sustainability 4 (2021) 821–829.

[5] Ultrafast Dynamics of Carotenoid Excited States−From Solution to Natural and Artificial Systems. Tomáš Polívka and Villy Sundström. Chem. Rev. 104 (2004) 2021−2071.

[6] Utilization of natural carotenoids as photosensitizers for dye-sensitized solar cells. Eiji Yamazaki, Masaki Murayama, Naomi Nishikawa, Noritsugu Hashimoto, Masashi Shoyama, Osamu Kurita. Solar Energy. 81 (2007) 512-516.

[7] Biocompatible and Biodegradable Materials for Organic Field-Effect Transistors. Irimia-Vladu, M. Troshin, P.A.; Reisinger, M. Shmygleva, L. Kanbur, Y. Schwabegger, G. Bodea, M. Schwödiauer, R. Mumyatov, A. Fergus. Adv. Funct. Mater. 20 (2010) 4069– 4076.

[8] Learning From Plants: Lycopene Additive Passivation toward Efficient and “Fresh” Perovskite Solar Cells with Oxygen and Ultraviolet Resistance. Xinmeng Zhuang, Donglei Zhou, Shuainan Liu, Rui Sun, Zhichong Shi, Le Liu, Tianyuan Wang, Bin Liu, Dali Liu, and Hongwei Song. Adv. Energy Mater. 12 (2022) 2200614.

[9] Mimicking Natural Antioxidant Systems for Improved Photostability in Wide-Band-Gap Perovskite Solar Cells. Francesco Bisconti, Mauro Leoncini, Salvatore Gambino, Nadir Vanni, Sonia Carallo, Francesca Russo, Vincenza Armenise, Andrea Listorti, Silvia Colella, Salvatore Valastro, Alessandra Alberti, Giovanni Mannino and Aurora Rizzo. ACS Nano. 18 (2024) 1573−1581.

[10] Production of Polyhydroxybutyrate (PHB) and Factors Impacting Its Chemical and Mechanical Characteristics. Blaithín McAdam, Margaret Brennan Fournet, Paul McDonald and Marija Mojicevic. Polymers. 12 (2020) 2908.

[11] https://www.european-bioplastics.org/

[12] Synthesis, structure and properties of polyhydroxyalkanoates: Biological polyesters. Sudesh K., Abe H. and Doi Y. Prog. Polym. Sci. 25 (2020) 1503–1555.

[13] Prospects for metal halide perovskite-based tandem solar cells. Rui Wang, Tianyi Huang, Jingjing Xue, Jinhui Tong, Kai Zhu and Yang Yang. Nature Photonics. 15 (2021) 411–425.

[14] Optical and electronic properties of mixed halide (X = I, Cl, Br) methylammonium lead perovskite solar cells. Sekai Tombe, Getachew Adam, Herwig Heilbrunner, Dogukan Hazar Apaydin, Christoph Ulbricht, Niyazi Serdar Sariciftci, Christopher J. Arendse, Emmanuel Iwuoha and Markus C. Scharber. J. Mater. Chem. C. 5 (2017) 1714-1723.

[15] Effect of Light Illumination on Mixed Halide Lead Perovskites: Reversible or Irreversible Transformation. Weixin Huang, Seog Joon Yoon and Pitambar Sapkota. ACS Appl. Energy Mater. 1 (2018) 2859−2865.

[16] Tracking Iodide and Bromide Ion Segregation in Mixed Halide Lead Perovskites during Photoirradiation. Yoon S. J., Draguta S., Manser J. S., Sharia O., Schneider W.F., Kuno M., Kamat P. V. ACS Energy Lett. 1 (2016) 290−296.

[17] Unraveling the Light-Induced Degradation Mechanisms of $CH_3NH_3PbI_3$ Perovskite Films. Nickel, N. H.; Lang, F.; Brus, V. V.; Shargaieva, O.; Rappich, J. Adv. Electron. Mater. 3 (2017) 1−9.

[18] IR Spectroscopic Degradation Study of Thin Organometal Halide Perovskite Films. Darkhan Yerezhep, Zhansaya Omarova, Abdurakhman Aldiyarov, Ainura Shinbayeva and Nurlan Tokmoldin. Molecules 28 (2023) 1288.

[19] Interaction of Organic Cation with Water Molecule in Perovskite MAPbI3: From Dynamic Orientational Disorder to Hydrogen Bonding. Zhuan Zhu, Viktor G. Hadjiev, Yaoguang Rong, Rui Guo, Bo Cao, Zhongjia Tang, Fan Qin, Yang Li, Yanan Wang, Fang Hao, Swaminathan Venkatesan, Wenzhi Li, Steven Baldelli, Arnold M. Guloy, Hui Fang, Yandi Hu, Yan Yao, Zhiming Wang and Jiming Bao. Chem. Mater. 28 (2016) 7385−7393.

[20] Open-circuit and short-circuit loss management in wide-gap perovskite p-i-n solar cells. Pietro Caprioglio, Joel A. Smith, Robert D. J. Oliver, Akash Dasgupta, Saqlain Choudhary, Michael D. Farrar, Alexandra J. Ramadan, Yen-Hung Lin, M. Greyson Christoforo, James M. Ball, Jonas Diekmann, Jarla Thiesbrummel, Karl-Augustin Zaininger, Xinyi Shen, Michael B. Johnston, Dieter Neher, Martin Stolterfoht & Henry J. Snaith. Nature Communications (2023) 14:932.

[21] Device Performance of Emerging Photovoltaic Materials (Version 3). Osbel Almora, Derya Baran, Guillermo C. Bazan, Carlos I. Cabrera, Sule Erten-Ela, Karen Forberich, Fei Guo, Jens Hauch, Anita W. Y. Ho-Baillie, T. Jesper Jacobsson, Rene A. J. Janssen, Thomas Kirchartz, Nikos Kopidakis, Maria A. Loi, Richard R. Lunt, Xavier

Mathew, Michael D. McGehee, Jie Min, David B. Mitzi, Mohammad K. Nazeeruddin, Jenny Nelson, Ana F. Nogueira, Ulrich W. Paetzold, Barry P. Rand, Uwe Rau, Henry J. Snaith, Eva Unger, Lídice Vaillant-Roca, Chenchen Yang, Hin-Lap Yip, Christoph J. Brabec. Adv. Energy Mater. 13 (2023) 2203313.

[22] Humidity-Assisted Chlorination with Solid Protection Strategy for Efficient Air-Fabricated Inverted CsPbI3 Perovskite Solar Cells. Sheng Fu, Wenxiao Zhang, Xiaodong Li Jianming, Guan Weijie, Song Junfeng Fang. ACS Energy Letters (2021) 6-10.

[23] Spectroscopic studies of neutral and chemically oxidized species of β-carotene, lycopene and norbixin in CH_2Cl_2: Fluorescence from intermediate compounds. D.D.D.H Alwis, U.G. Chandrika, P.M. Jayaweera. Journal of Luminescence 158 (2015) 60–64.

[24] Recent studies of the photovoltaic device enhancement via multifunctional luminescent down-shifting films. Junhee Cho. Jpn. J. Appl. Phys. 62 (2023) SE0802.

[25] Modulated $CH_3NH_3PbI_{3-x}Br_x$ film for efficient perovskite solar cells exceeding 18%. Yongguang Tu, Jihuai Wu, Zhang Lan, Xin He, Jia Dong, Jinbiao Jia, Panfeng Guo, Jianming Lin, Miaoliang Huang and Yunfang Huang. Scientific Reports. 7 (2017) 44603.

[26] Device Performance of Emerging Photovoltaic Materials. Osbel Almora, Derya Baran, Guillermo C. Bazan, Christian Berger, Carlos I. Cabrera,Kylie R. Catchpole, Sule Erten-Ela, Fei Guo, Jens Hauch, Anita W. Y. Ho-Baillie,T. Jesper Jacobsson, Rene A. J. Janssen, Thomas Kirchartz, Nikos Kopidakis, Yongfang Li,Maria A. Loi, Richard R. Lunt, Xavier Mathew, Michael D. McGehee, Jie Min,David B. Mitzi, Mohammad K. Nazeeruddin, Jenny Nelson, Ana F. Nogueira,Ulrich W. Paetzold, Nam-Gyu Park, Barry P. Rand, Uwe Rau, Henry J. Snaith,Eva Unger, Lídice Vaillant-Roca, Hin-Lap Yip, and Christoph J. Brabec. Adv. Energy Mater. 13 (2023) 2203313.

[27] Thermal stability and performance enhancement of perovskite solar cells through oxalic acid-induced perovskite formation. M. Adil Afroz, N. Ghimire, K.M. Reza, B. Bahrami, R.S. Bobba, A. Gurung, A. H. Chowdhury, P.K. Iyer, Q. Qiao. ACS Appl. Energy Mater. 3 (2020) 2432−2439.

[28] Perovskite films passivated by poly[(R)-3-hydroxybutyric acid] for improved photovoltaic performance. Yifang Qi, Jing Qu, Jaiden Moore, Kristine Gollinger, Narendra Shrestha, Yongfeng Zhao, Nihar Pradhan, Jinke Tang, Qilin Dai. Organic Electronics. 104 (2022) 106487.

[29] Stabilization of Black Perovskite Phase in $FAPbI_3$ and $CsPbI_3$. Sofia Masi, Andrés Fabián Gualdrón Reyes, and Ivan Mora-Seró. ACS Energy Lett. 5 (2020) 1974−1985.

[30] Thermal Stability Analysis of Formamidinium–Cesium-Based Lead Halide Perovskite Solar Cells Fabricated under Air Ambient Conditions**.** Binita Boro, Snehangshu Mishra, Paulomi Singh, Basudev Lahiri, Shailendra Kumar Varshney, Trilok Singh. Energy Technol. 12 (2024) 2400034.

[31] The Long-Wavelength Edge of Photographic Sensitivity and of the Electronic Absorption of Solids. Urbach, F.. Phys. Rev. 92 (1953) 1324−1324.

[32] Life on the Urbach Edge. Ugur, E.; Ledinsky,́ M.; Allen, T. G.; Holovsky,́ J.; Vlk, A.; De Wolf, S. J. Phys. Chem. Lett. 13 (2022) 7702− 7711.

[33] The fabrication of formamidinium lead iodide perovskite thin films via organic cation exchange. Zhongmin Zhou, Shuping Pang, Fuxiang Ji, Bo Zhang and Guanglei Cui. Chem. Commun., 52 (2016) 3828—3831.

[34] Formamidinium Lead Iodide-Based Inverted Perovskite Solar Cells with Efficiency over 25% Enabled by An Amphiphilic Molecular Hole-Transporter. HuidongZhang, ShuoZhang, XiaoyuJi, JingwenHe, HuanxinGuo, SongranWang, WenjunWu, Wei-HongZhu and YongzhenWu. Angew.Chem. 136 (2024) e202401260.

[35] Processing and Thermomechanical Properties of PHA. Vito Gigante, Patrizia Cinelli, Maurizia Seggiani, Vera A. Alavarez, Andrea Lazzeri. 1th edition (2020) 9781003087663.

Chapter 4

Interface engineering of $CsPbI_3$-based solar cells.

Cesium lead triiodide ($CsPbI_3$) perovskite has garnered significant attention as a promising alternative to the organic-inorganic halide counterparts, based on MA and FA cations, in PSCs. Its appeal lies in the nonvolatile nature, thermal stability and photoelectric properties. With a relatively wide bandgap of 1.60–1.72 eV, all inorganic perovskites are particularly well-suited for indoor application [1] and as sub-cell in both perovskite-silicon and perovskite tandem PSCs [2,3]. These configurations hold substantial potential for exceeding the Shockley-Queisser limit of single-junction solar cells, thereby achieving higher PCE, which is a critical aspect for advancing solar technology. In this chapter I report the stabilization of the black beta phase of fully inorganic $CsPbI_3$ by using $DMAPbI_3$ (dimethylammonium lead iodide) as main reactant. This compound serves a dual role: as a DMA^+ additive to stabilize the black phase and as a lead source. So synthetized $CsPbI_3$ is integrated into an inverted device architecture, optimizing its performance. Main novelty is the incorporation of a diradicalic molecule, a novel interlayer, 2,2′,2″,2‴-((perchlorocyclohexa-2,5-diene-1,4-diyliene)bis(methanediylyldene))tetrakis-(1,3,5-trichlorobenzene) (TTH), that enhance device performance. At an optimized concentration of 0.75 mg/mL, TTH achieves a PCE of 8.12% by reducing interfacial recombination and promoting efficient charge separation through dipole formation in the excited state.

Through optical and electronic characterization, I find that TTH exhibits superior resistance to photobleaching compared to conventional interlayers, significantly improving device stability. Impedance spectroscopy reveals reduced recombination resistance and lower interfacial losses in TTH-treated devices, consistent with the observed improvements in Voc and FF. Additionally, the enhanced photocurrent in the short-wavelength region highlights TTH's ability to improve charge collection and minimize nonradiative losses.

4.1 State of the art and premises.

4.1.1 Doping Strategies for Enhancing $CsPbI_3$ Film Quality and Phase Stability.

In the early stages of research into $CsPbI_3$-based inorganic perovskite solar cells (PSCs), one of the major challenges was the lack of effective photovoltaic performance, primarily due to insufficient film thickness [4]. This issue arose from the low solubility of CsI in common solvents and the poor phase stability of $CsPbI_3$, as previously discussed. A breakthrough occurred in 2015 when Eperon et al. [5] demonstrated that incorporating HI as an additive in the precursor stabilized the black perovskite phase at room temperature, achieving a device efficiency of 2.9%. They proposed that HI improved the crystallization process by reducing grain size and accelerating crystallization, owing to its high surface energy. Moreover, the

presence of HI induced lattice strain, facilitating phase transitions at lower temperatures. Lowering the crystallization temperature offers significant benefits, including improved film quality and reduced defect formation, ultimately enhancing device performance. To further enhance the deposition of black-phase $CsPbI_3$ perovskite, the precursors "$HPbI_3$" and "$HPbI_x$" (also known as PbI_2·xHI) were developed. Recent studies revealed that this acidic additive reacts DMF via hydrolysis, forming formic acid (CH_2O_2) and dimethylammonium iodide ($(CH_3)_2NH_2I$, DMAI). It has been suggested that the previously reported "HI" additive and "$HPbI_3$" should instead be interpreted as DMAI and $DMAPbI_3$ (dimethylammonium lead iodide), respectively [6]. Building on these insights, Yong Wang et al. [7] confirmed that DMAI can serve as an additive to regulate $CsPbI_3$ inorganic perovskite crystallization. They revealed that substituting Cs^+ (r = 167 pm) with the larger DMA^+ ion (r = 230 pm) significantly affects the crystallization kinetics, crystal phases, and morphologies of the perovskite films.

Ke et al. [6] synthesized $Cs_{0.7}DMA_{0.3}PbI_3$ perovskite with a tolerance factor of 0.904 at a low temperature of under 100°C. Similarly, Meng et al. [8] prepared $DMA_{0.15}Cs_{0.85}PbI_3$ perovskite at an annealing temperature of 180°C, reporting that the resulting material exhibited a narrower Eg of 1.67 eV and superior phase stability compared to γ-$CsPbI_3$. A device using this material in a regular architecture achieved a champion PCE of 15.3% and demonstrated excellent stability for three months in dry air. Notably, they investigated the chemical composition and phase evolution of the mixed $DMA_{1-x}Cs_xPbI_3$ layer during thermal treatment. They showed that DMA^+ ions could be embedded into the crystal lattice to form intermediate states such as $DMA_{0.15}Cs_{0.85}PbI_3$ through a solid-state reaction between $DMAPbI_3$ and Cs_4PbI_6. Conversely, some researchers argue that DMAI can be completely removed without alloying into the $CsPbI_3$ crystal lattice under optimized conditions. Wang et al. [4] proven that DMAI acts as a volatile additive, rather than a dopant, and can entirely be eliminated from the final β-$CsPbI_3$ film with appropriate annealing processes. They showed that by carefully adjusting the excess DMAI molar ratio, it is possible to selectively stabilize two distinct $CsPbI_3$ polymorphs: the γ phase and the β phase. Specifically, a $CsPbI_3$:DMAI molar ratio of 0.5 or 0.7 stabilizes the γ phase, while increasing the ratio to 1.2 or 1.5 stabilizes the β phase. The apparent contradiction regarding the role of DMA^+ stems from differences in annealing temperature and humidity conditions. Since the sublimation temperature of DMAI is approximately 150°C, DMA^+ tends to alloy into the $CsPbI_3$ lattice at low temperatures but is removed at the commonly used annealing temperature of 210°C. Additionally, the sublimation rate of DMAI is highly dependent on moisture, volatilizing more rapidly in dry air compared to argon (*Figure 4.1a-b*) [9].

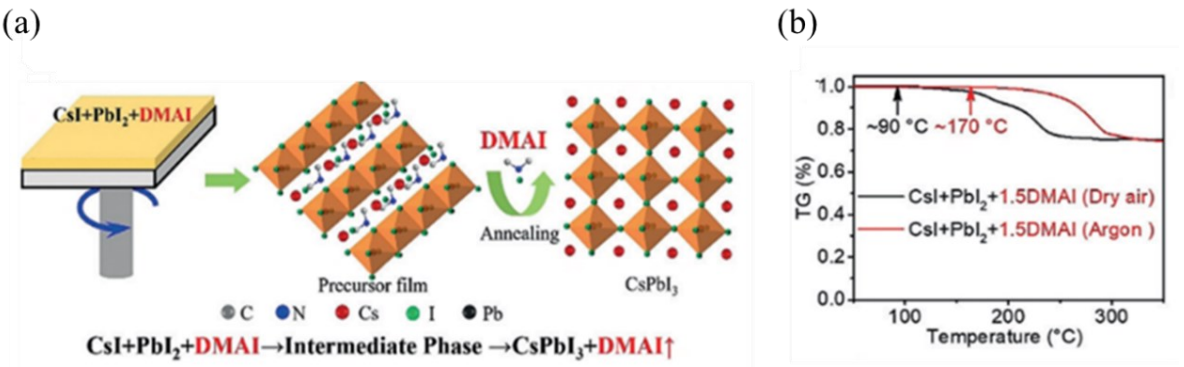

Figure 4.1 (a) Schematic mechanism for DMAI additive induced black phase $CsPbI_3$ formation. (b) TGA of the powder scratched from the precursor film of $CsI+PbI_2$+1.5DMAI under the argon and 5–10% RH dry air conditions, respectively [7].

4.1.2 Challenges and Opportunities in Inverted Inorganic Perovskite Solar Cells.

As discussed in the paragraph 1.7.1, there are various device architectures for perovskite materials, the most reported in the literature for inorganic perovskites being the regular architecture (n-i-p). The regular structure usually utilizes high-temperature sintered TiO_2 as the ETL and Spiro-OMeTAD with dopants such as 4-tert-butylpyridine and lithium salts as the HTLs. Despite the remarkable development, with efficiencies now exceeding 21% [10, 11, 12], this architecture has certain limitations such as the use of thermophobic HTLs, high processing temperatures of the electron transporting ETLs which limit their implementation in tandem solar cells. In contrast, the inverted p-i-n structure offers several key advantages over the n-i-p design:

- low energy cost due to the exclusion of high temperature annealing of the front layer;

-better air and humidity robustness owing to the dopant-free rear layer with enhanced hydrophobicity, compared with the conventional rear layer with corrosive and hygroscopic dopants of regular devices;

-more favorable with the promising application in a tandem structure for serving as a sub-cell.

These advantages of the inverted inorganic PSCs make them attract increasing attention and trigger a research fever of improving their efficiency [13]. The inverted inorganic PSCs are mainly focused on $CsPbI_3$ and $CsPbI_2Br$ due to their suitable bandgap (1.7 and 1.9 eV respectively) for application in photovoltaic field. The first inverted inorganic PSC was proposed by Snaith in 2015, showing an efficiency of 1.7% [5]. However, compared to the regular architecture, inverted inorganic PSCs exhibit relatively lower PCE and greater open-circuit voltage V_{oc} losses [14]. These challenges primarily stem from the limited availability of suitable charge transport materials. The lower wettability of p-type metal oxides and organic HTLs for inorganic perovskite film growth, compared to n-type metal oxides, and the high annealing temperatures required for inorganic perovskites make commonly used HTLs less than ideal for such applications.

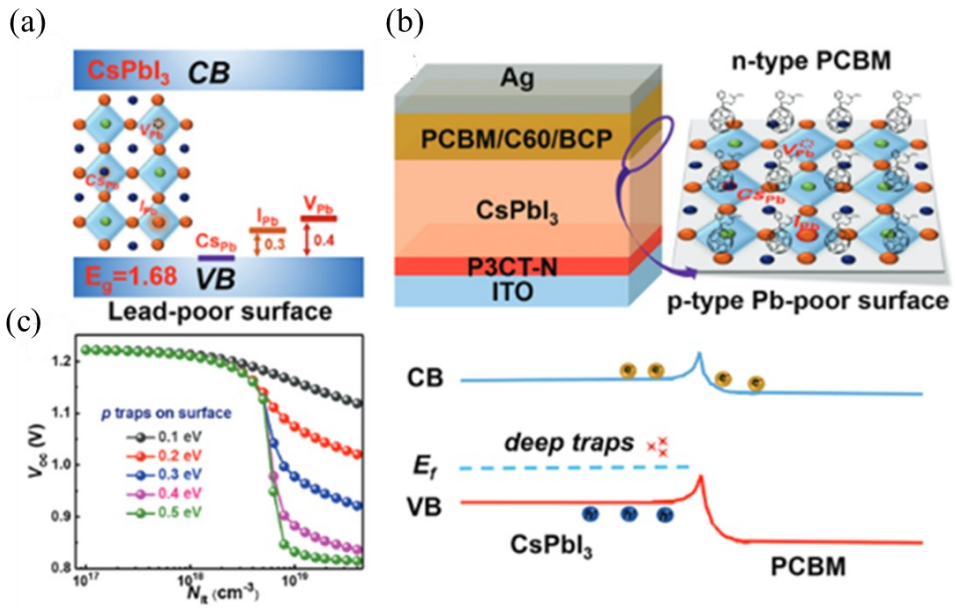

Figure 4.2 Illumination of intrinsically Pb-poor surface and influence. a) Theoretically simulated electronic states of lead-poor relevant traps in $CsPbI_3$ band energy levels. b) Schematic diagram of the hindered electronic transport at cathode interface for the lead-poor surface. c) Electric simulations of photovoltaic performances with various depth and density p-type traps on $CsPbI_3$ surface [16].

Additionally, the energy level mismatch between inorganic perovskites and both HTLs and ETLs further contributes to the lower efficiency of inverted devices. Consequently, the rational design and optimization of charge transport materials are essential to enhance charge extraction and support the formation of high-quality inorganic perovskite films [15]. As known, a device's Voc directly relates to the interfacial property, in addition to the intrinsic nature of bulk photoabsorbing layer. Combining with devices simulation, Neher et al. found that interfacial recombination was a main factor limiting device efficiency, especially V_{oc} in inverted PSCs [16].

Sheng Fu et al. [17,18] focused on the surface components analysis of $CsPbI_3$ films and found that the intrinsically lead-poor surface was spontaneously formed with the stoichiometric precursors. Trought density functional theory (DFT) simulations concluded that the traps relevant to Pb poor issues were p states, and the Pb vacancy (V_{Pb}), I–Pb inversion (I_{Pb}) and Cs–Pb inversion (Cs_{Pb}) traps featured the localized states. These p traps with deep energy level natures would pin the Fermi energy levels (E_f) around the valence band edge (VB) (*Figure 4.2a*), which resulted in poor electron transfer and serious nonradiative recombination at the $CsPbI_3$/PCBM interface (*Figure 4.2b*). Through simulations considering various *p*-type traps and their densities (N_{it}) on the $CsPbI_3$ surface, they concluded that at low trap densities (Nit $<1\times10^{18}$ cm^{-3}), the impacts on FF and V_{oc} were negligible. However, as N_{it} increased beyond $3\times10^{18}cm^{-3}$, both FF and V_{oc} declined sharply (*Figure 4.2c*). Additionally, the depth of the trap states played a critical role, with deeper traps causing more significant V_{oc} losses.

4.1.3 Molecular surface passivation for $CsPbI_3$.

Molecular passivation could partially ameliorate the localized states of V_{Pb} and I_{Pb} traps without healing the p-type surface, and presented the limited efficiency improvement with a large V_{oc} loss [19]. Previous studies have highlighted various promising interface engineering of inverted

inorganic PSCs aimed to minimize surface defect density, align energy levels, enhance charge transport efficiency, and shield the perovskite film from moisture ingress. Many materials were used for this purpose as interlayers between the perovskite layer and the charge transporting material on top, including organic molecules, quantum dots and organic halide ammonium salts. Recently, Li et al. [20] inserted a passivating dipole layer with high molecular polarity at the interface between inorganic perovskite and ETL. The induced strong interaction with both inorganic perovskite and C_{60} improved the energy alignment and accelerated the charge extraction. PCBM helps to passivate defects at the interface, which minimizes charge recombination and contributes to increased efficiency and stability of the device. It also improves the morphology of the interfacial region, leading to smoother and more uniform films, which are crucial for achieving high-performance devices. This alignment reduces the energy barrier, thereby improving charge extraction. This demonstrates that the inclusion of PCBM, as highlighted in prior studies, is a key strategy for optimizing the interface and enhancing the overall functionality of perovskite-based optoelectronic devices [21].

Free-radicals molecules have been proposed as additives for perovskites primarly serving as n-type dopants and acting as antioxidants. Recently, donor-acceptor trityl radicals bearing carbazole or aryl amine donor groups have been employed as effective HTLs due to their favourable charge transport properties and ability to passivate interfacial defects [22]. Simple trityl radicals, such as tris(2,4,6-trichlorophenyl)methyl radical (TTM, shown in Figure 4.5), exhibit suitable redox potentials for use as interlayers between the perovskite and the ETL [23]. Unfortunately, the lack of charge-transfer stabilization in the excited state makes these radicals highly photosensitive, limiting their use in photovoltaic devices. To address this issue, we propose the use of a polyhalogenated Thiele hydrocarbon, specifically the TTM-like Thiele hydrocarbon (TTH, shown in Figure 4.5), as an interlayer in the heterojunction between $CsPbI_3$ perovskite and C_{60}. TTH shares nearly identical redox properties with the TTM radical, and its HOMO and LUMO levels align closely with those of PCBM. However, unlike TTM, TTH offers exceptional photostability due to its singlet species nature.

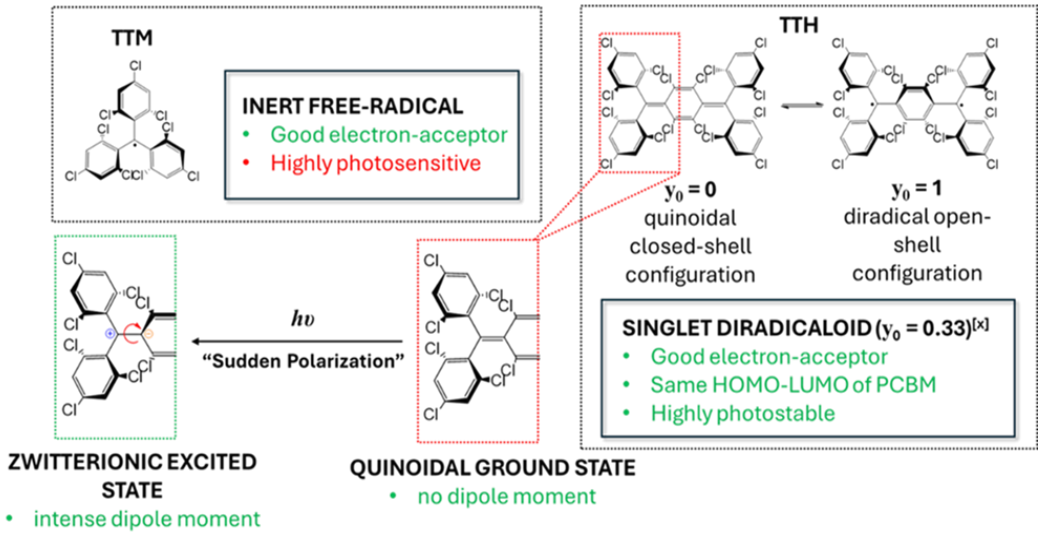

Figure 4.3 Excited-State Polarization. Molecular structure of TTM radical, TTH diradicaloid and pictorial representation of sudden polarization of the TTH in the excited, where the elongation and twisting of exocyclic double bonds induces a symmetry breaking of the molecule with the consequent formation of a charge separated state (zwitterion).

TTH belongs to the family of singlet diradicaloids, singlet species characterized by moderate degree of diradical character, described using the diradical index y_0, which ranges from zero (closed-shell species) to one (pure diradical) (*Figure 4.3*) [24].
In the case of TTH the y_0 exhibits a value of 0.33. Beyond their impressive photostability, polyhalogenated Thiele hydrocarbons exhibit remarkable photophysical properties, including efficient luminescence arising from a zwitterionic doubly excited state, driven by a sudden polarization process (the elongation and twisting of exocyclic double bonds induce the formation of a charge-separated state), as schematically shown in *Figure 4.3*. Although such derivatives have been suggested as emitting materials capable of surpassing the theoretical internal quantum efficiency limit of 0.25 for singlet species in electroluminescent devices [25], their potential use in PSCs has not yet been explored.

4.2 Experimental results and discussion.

4.2.1 $DMAPbI_3$ precursor synthesis.

The $DMAPbI_3$ precursor is synthesized by reacting PbI_2 and HI in DMF (details in Chapter 2), which serves as the starting material for Cs-based perovskite films (*Figure 4.4a*). The synthesized powder is characterized using ATR-FTIR and XRD measurements. The ATR-FTIR spectrum confirms the presence of N-H and C-H bonds (*Figure 4.4b*), showing clear signatures of the N-H stretching mode (3200–3450 cm^{-1}), the C-H stretching mode (3020–2725 cm^{-1}), and the C-H bending mode (1490–1350 cm^{-1}). The UV-Vis absorption spectra (*Figure 4.4c*) and XRD pattern (Figure 4.4d) confirm the successful formation of $DMAPbI_3$, identified as a hexagonal perovskite [26].

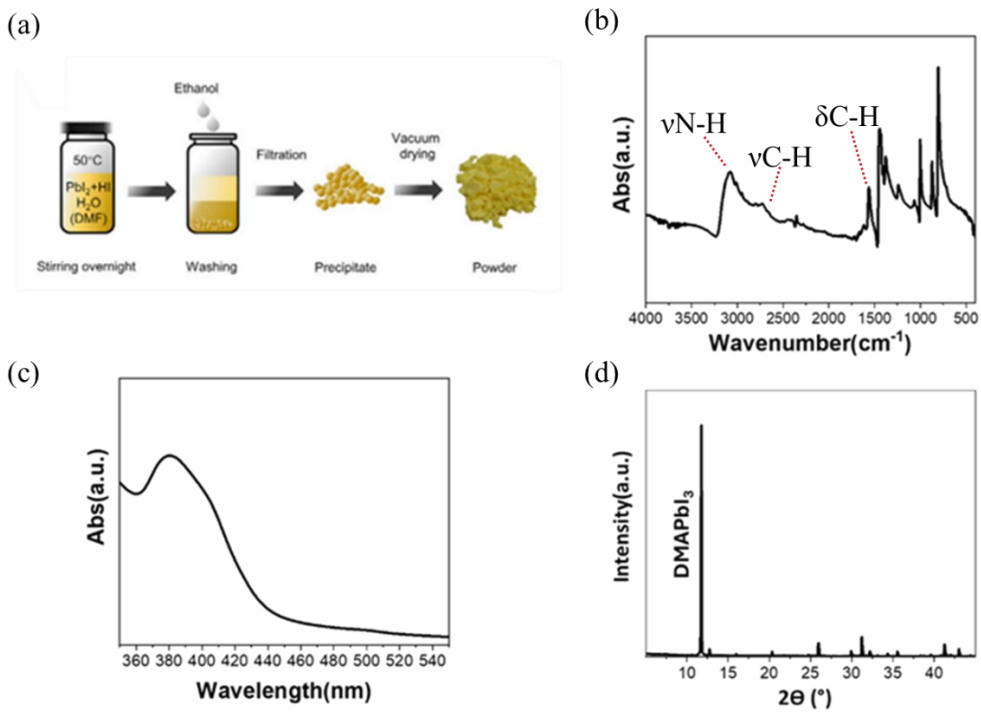

Figure 4.4 (a) Schematic mechanism of $DMAPbI_3$ formation. (b)ATR-FTIR of $DMAPbI_3$ powder (b)UV-VIS absorption spectra of DMAPbI3 powder. (c) XRD of $DMAPbI_3$.

The use of $DMAPbI_3$ allows for precise control over the stoichiometry during the formation of $CsPbI_3$. The resulting $CsPbI_3$ film undergoes thorough characterization, showing a UV-Vis

absorption onset at 730 nm (Figure 4.5a) and a PL emission maximum at 721 nm, values that align well with those reported in the literature [4,7]. XRD analysis provides information about the crystallographic structure, showing peaks corresponding to the (110) and (220) reflections of the β phase $CsPbI_3$ at 14.3˚ and 28.8˚ in the sample annealed for 60 s. The characteristic peak of $DMAPbI_3$ at 11.6° is not visible (*Figure 4.5b*).

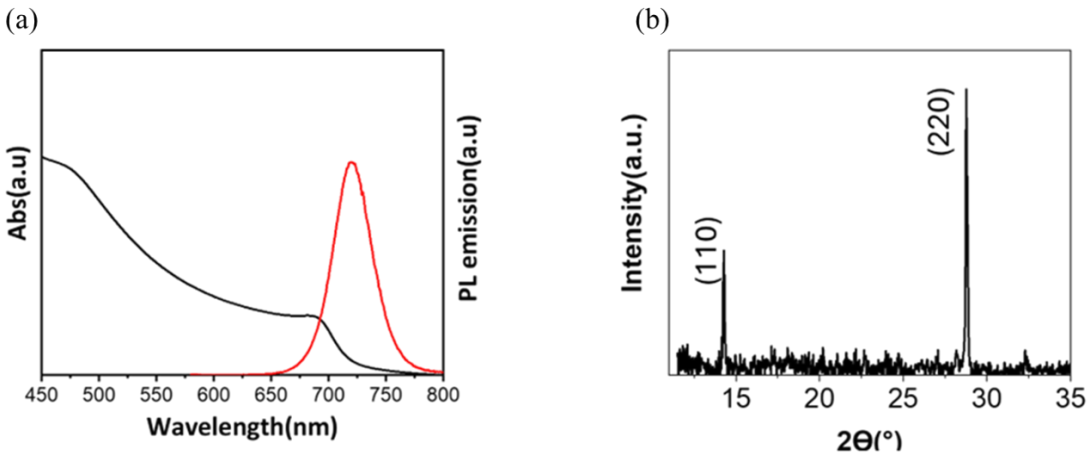

Figure 4.5 UV-VIS absorption spectra of $CsPbI_3$ thin film. (b) XRD diffraction pattern of $CsPbI_3$ thin film.

4.2.2 Optimization of reference device.

The p–i–n device stack fabricated in this work is: glass/indium tin oxide (ITO)/PEDOT:PSS/ $CsPbI_3$/C_{60}/bathocuproine (BCP)/silver (Ag). PCBM is considered as reference interlayer between C_{60} and $CsPbI_3$, playing a pivotal role in enhancing device performance thanks to a beneficial energy level alignment at the interface, facilitating more efficient electron transfer from the perovskite layer to the electron transport layer. PCBM is incorporated into the device architecture, and two additional concentrations—one higher and one lower than the value reported in the literature—were tested to identify the optimal concentration (*Figure 4.6a*), clearly elected 10 mg/ml as the concentration leading to the best PCE. The higher and lower concentrations likely lead to imbalances in charge transport and interfacial properties. The crystallization of good quality $CsPbI_3$ film is achieved by adding dimethylammonium chloride (DMACl) as additive in the precursor mixture, forming a low-solubility complex (Cs_4PbI_6-Cl) in the precursor, acting as a seed during solvent evaporation, and passivating the surface with residual DMA^+ (*Figure 4.6b*) [12]. As shown in *Figure 4.6c*, various concentrations of DMACl are tested within the perovskite film to optimize crystallization and surface passivation. Among these, a concentration of 4% w/v DMACl demonstrated the best PCE and is subsequently employed in further experiments. The incorporation of DMACl not affect the crystallization temperature, suggesting that the additive mainly influences the crystallization process by acting as a seed and surface passivator, rather than altering the crystallization temperature.

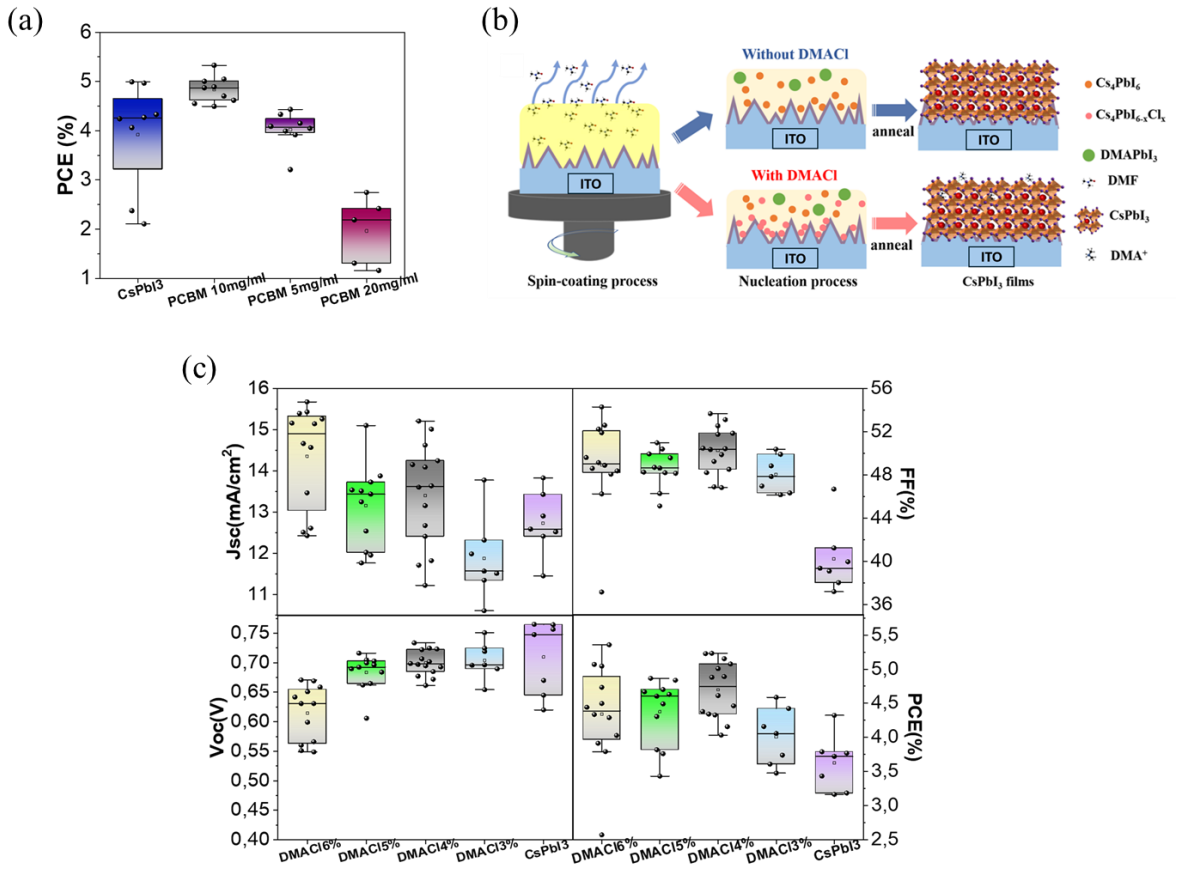

Figure 4.6 $CsPbI_3$ Film optimization (a) PCE obtained for PCBM used like interlayer at different concentration 20mg/ml, 10mg/ml and 5mg/ml in CB (b) Schematic illustration of the perovskite crystallization without and with DMACl additives [12]. (c) Statistical photovoltaic parameters obtained for DMACl incorporation in $CsPbI_3$ at different w/v% concentrations 6%; 5%, 4% and 3% and pristine $CsPbI_3$.

4.2.3 Morphological Analysis

As prepared $CsPbI_3$ film shows an absorbance onset at ~736 nm in *Figure 4.7a* indicating a band gap of 1.68 eV. The optical energy band gap has been calculated by Tauc's plot by plotting graph between (hv) vs $(\alpha h\nu)^2$ [7]. A typical cross-sectional SEM image of the device stack is shown in *Figure 4.7b*, revealing a perovskite film thickness of approximately 190 nm, with grain extending throughout the film. This film thickness is limited by the low molar concentration, which is due to the poor solubility of CsI in polar aprotic solvents [4,27]. In the SEM top-view (*Figure 4.7c*), it is evident that the addition of DMACl reduces pinholes and improves the uniformity of the film.

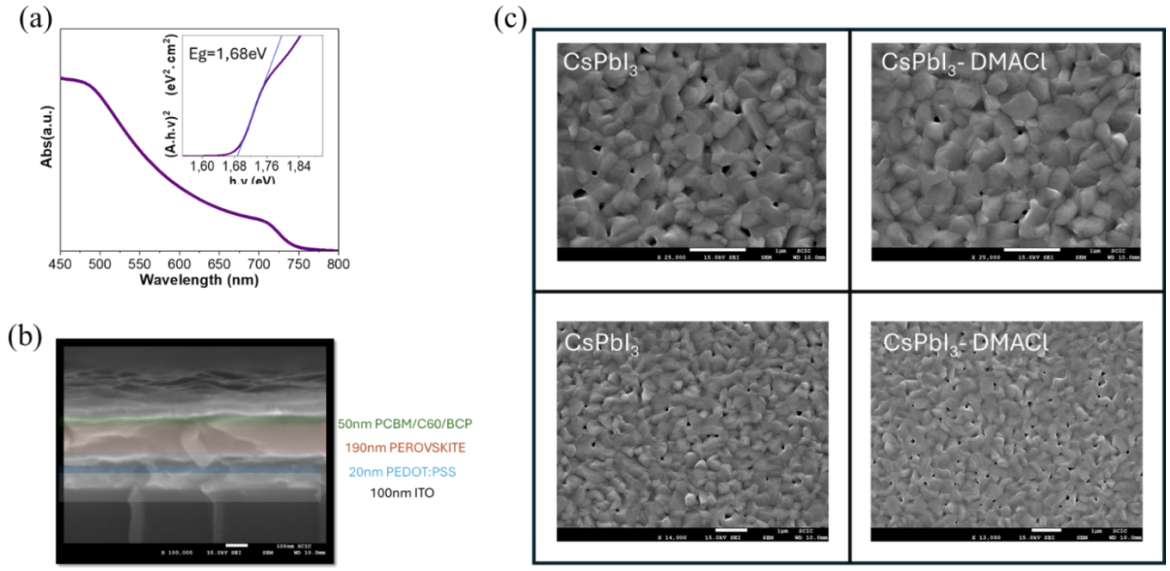

Figure 4.7 (a) UV-VIS Absorption spectra of the perovskite film and Tauc's plot to determine Energy gap of $CsPbI_3$ thin film. (b) The cross-section and surface SEM images of the stack cell (c) and SEM top view $CsPbI_3$ perovskite film without and with DMACl.

4.2.4 TTH Device integration.

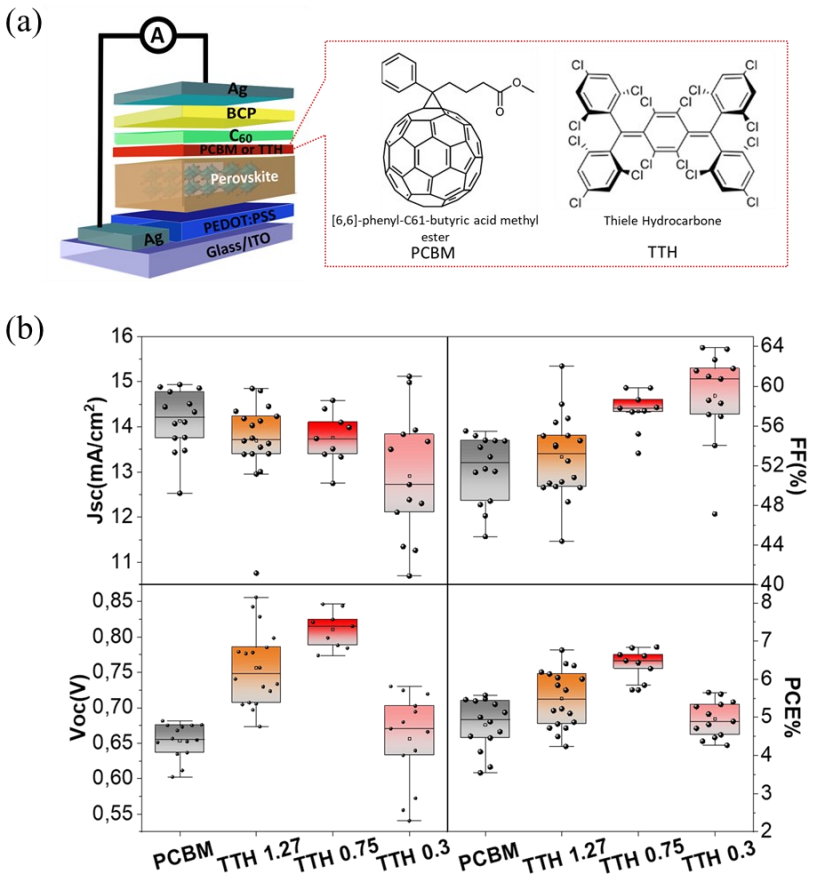

Figure 4.8 (a) Schematic illustration of device stck. (b) Statistical photovoltaic parameter of TTH integration at different concentrations 1.27mg/ml, 0,75mg/ml ,0,3mg/ml in CB compared to the reference PCBM.

The impact of the TTH deposition layer on device characteristics is investigated using a p–i–n cell stack: glass/indium tin oxide (ITO)/PEDOT:PSS/$CsPbI_3$/PCBM or TTH/C_{60}/bathocuproine

(BCP)/silver (Ag) (*Figure 4.8a*). To identify the optimal concentration of TTH in the device stack, a screening process was conducted directly on the devices. The photovoltaic performance statistics from this screening, shown in *Figure 4.8b*, highlight the influence of varying TTH concentrations in CB on device efficiency. The concentration of 0.75 mg/mL was found to yield the highest PCE and was subsequently selected for further use.

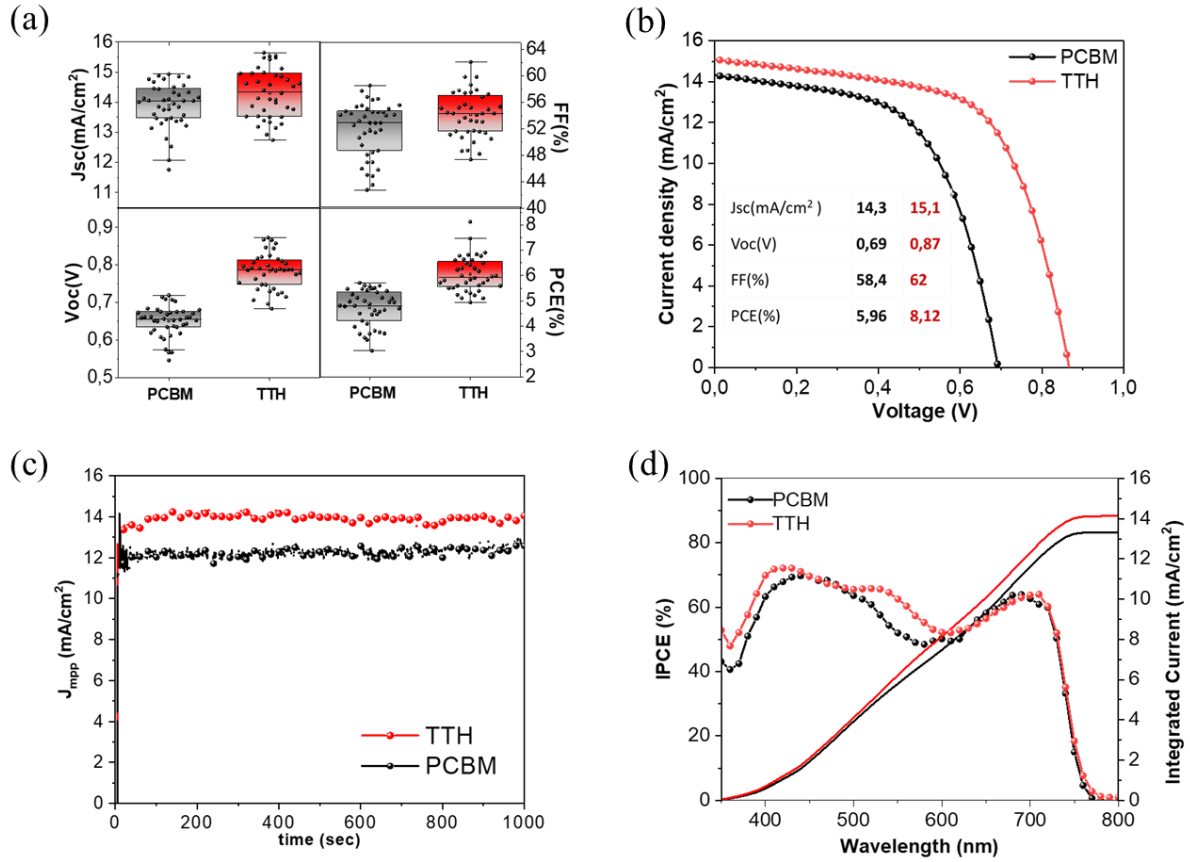

Figure 4.9 (a) Statistical photovoltaic parameters obtained from 40 devices for PCBM and TTH. (b) J–V curves of the sample PCBM (reference) and TTH p–i–n PSCs under 1-sun (100 mW/cm^2) illumination. (c) The stabilized power output under maximum power point (MPP) condition of the TTH and PCBM. (d) Comparison of the IPCE spectra with the integrated Jsc of 13.31 mA /cm^2 and 14.13 mA /cm^2 for the PCBM and the TTH, respectively.

The statistical photovoltaic parameters from 40 devices and the J–V curves of the champion device are presented in *Figure 4.9a,b*. The introduction of TTH layer remarkably increased the V_{oc} from 0.69V to 0.86V, together with an increase of all other parameters. The steady power output for this champion device sustains at 13.37mA/cm^2, measuring at the fixed voltage of 0.86 V close to the maximum power point (*Figure 4.9c*). To further verify the photocurrent enhancement, incident photon to current efficiency (IPCE) spectra are recorded (*Figure 4.9d*) revealing the well-matched current density to the J_{sc} from J–V curves with the integrated current density of 13.31 and 14.14 mA/cm^2 for the PCBM and TTH integrated devices. Moreover, the iodide PSCs feature higher absorption at the long-wavelength region [28]. The enhanced short-wavelength absorption (500-540nm) with TTH incorporated in the cell, indicates that this interlayer plays a crucial role in absorbing photons at that wavelength and contributing to the generation of electric current, both through its direct absorption and by enhancing charge collection efficiency at the interface. This could lead to an increase in the

overall efficiency of the solar cell, highlighting the formation of the dipole moment in the excited state of the diradicaloid.

4.2.5 Optoelectronic properties.

Polyhalogenated trityl radicals such as TTM suffer from severe photosensitivity, which is typically mitigated by coupling the radical core, acting as an electron-acceptor (A) moiety, with an electron-donor (D) group to generate a push-pull derivative. Under UV irradiation TTH remains stable, demonstrating its resistance to photoexcitation and the effectiveness of the push-pull strategy [24].

Upon incorporation of the perovskite into the device, the p-type surface with deep energy-level traps can lead to uneven band bending at the PCBM/$CsPbI_3$ interface, resulting in hindered electron transfer and significant nonradiative recombination [13, 18]. The undesirable electron-transfer dynamics would limit the efficiency improvement of inverted $CsPbI_3$ PSCs with low V_{oc} and FF. Under light excitation, TTH exhibits the same LUMO energy level as PCBM *Figure 4.10a,b*. The hypothesis that the dipole forms exclusively in the excited state can be supported by the analysis of the steady-state normalized PL spectra (*Figure 4.10c*) when the system is excited at 570 nm. In the current context, the excitation at this wavelength reveals the convolution of two distinct emission peaks: one corresponding to the perovskite (at 723 nm) and the other associated with TTH (at 681nm). This observation is significant because it suggests that the interaction between the two materials, likely through charge or energy transfer, only occurs in the excited state. This aspect justifies the observed increase in both V_{oc} and FF in the devices. The formation of the dipole can lead to improved polarization of the material, facilitating more efficient charge separation.

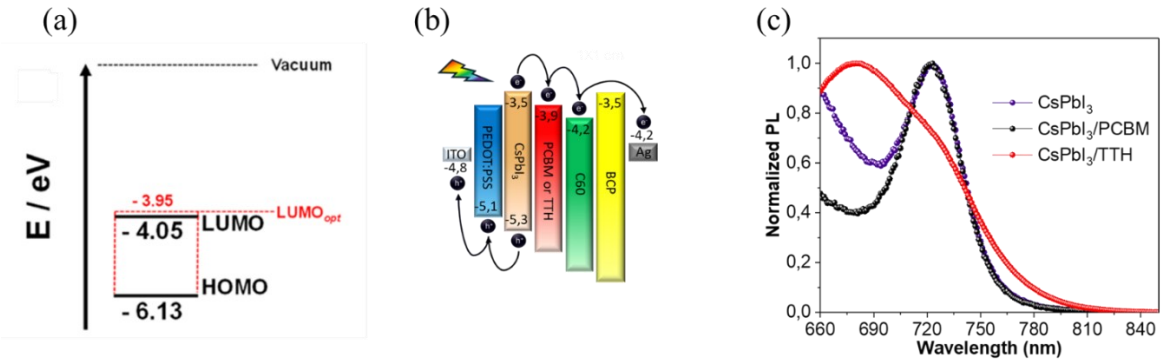

Figure 4.10 (a) Representation of the highest occupied molecular orbital (HOMO) and lowest unoccupied molecular orbital (LUMO) calculated through the empirical equations $E_{HOMO}= -[E_{(ox\ vs\ Fc/Fc+)} + 5.1\ V]$ and $E_{LUMO}=-[E_{(red\ vs\ Fc/Fc+)} + 5.1\ V]$. The $LUMO_{opt}$ energy level was estimated as follows: $LUMO_{opt} = HOMO + Eg_{opt}$, in which Eg_{opt} is obtained from the λ_{onset}. (b) Energy level diagram for the device. (c) Steady -state normalized PL spectra of ITO/PEDOT:PSS/$CsPbI_3$ and ITO/PEDOT:PSS/$CsPbI_3$/PCBM or TTH respectively.

4.2.6 Electrical characterization.

To further investigate the role and effect of TTH, impedance spectroscopy (IS) is measured at open-circuit conditions with different light intensities for TTH and PCBM based solar cells [29]. The Nyquist plots at V_{oc} of impedance spectra at 1 sun are represented in *Figure 4,11a*. As it is predictably observed in highly efficient PSCs, we detected principally two different semicircles, at low-frequency (LF) and high-frequency (HF) ranges. In the devices measured it

is observed a decrease in width of the arc when TTH is used which indicates a lower resistance or better transport due to the presence of TTH at interface with perovskite which will result in higher PCE. These data are modeled with an equivalent circuit previously reported shown in the inset in *Figure 4.11a* [30]. In particular, the recombination resistance, R_{rec}, see *Figure 4.11b*, is obtained by the fitting of impedance measurements, as the sum of the resistances of HF and LF arcs, considering transport-resistance negligible [31, 32]. In the presence of TTH layer the recombination resistance increases, which in turn implies a decrease of the nonradiative recombination rate. The recombination losses are effectively reduced by TTH, in line with the observed increase of the V_{oc}. This could be due to the improved interface matching which induces halide perovskite passivation, reduction of interfacial recombination and to the formation of the dipole at the excited state.

The lower surface recombination also contributes to the enhancement of photocurrent as observed in *Figure 4.11*. In addition, the low frequency capacitance observed for these samples decreases with the TTH (*Figure 4.11c*), in line also with the improved FF.

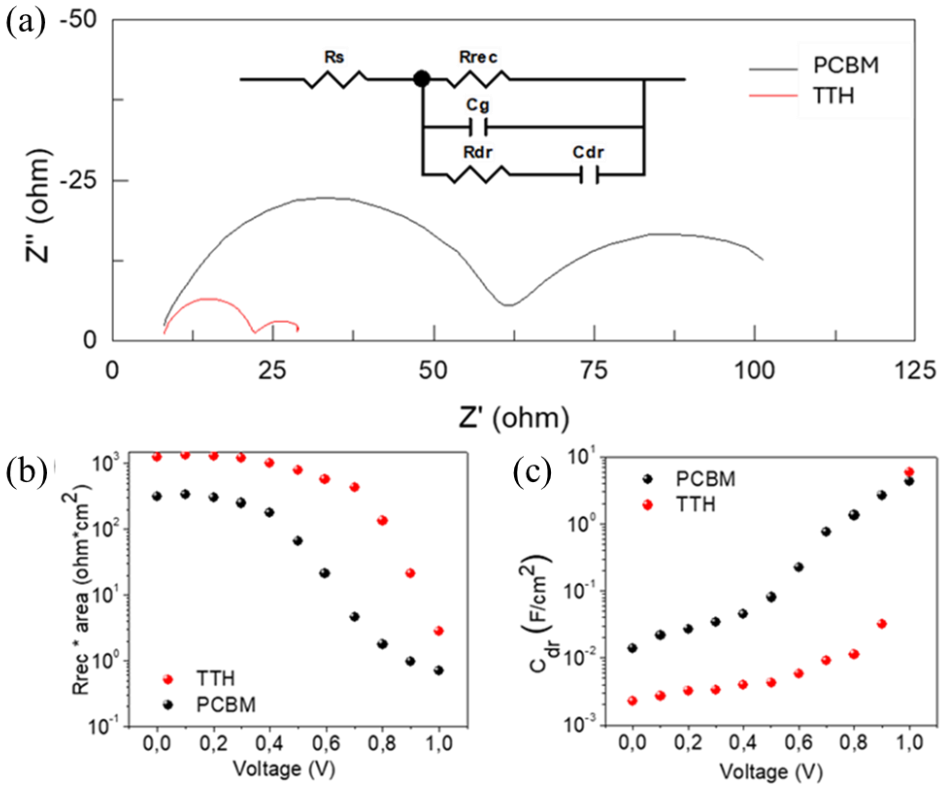

Figure 4.11 Electrical characterization. a) Nyquist plots at open-circuit voltage under 1 sun illumination intensity, b) equivalent circuit model composed of a series resistance, R_s, recombination resistance, R_{rec}, obtained as the sum of HF and LF arcs, considering the transport resistance negligible, which is in parallel to a HF capacitance, Cg, the geometrical capacitance, and in parallel with a RC branch (C_{dr} and R_{dr}), that splits the pattern in the HF and LF arcs [30];]b) Plot of recombination resistance (R_{rec}) versus applied voltage and c) plot of the capacitance (C_{dr}) versus applied voltage of devices based on PCBM and TTH as ETMs.

4.3 Conclusions.

In this chapter the significant potential of CsPbI3 PSCs for photovoltaic applications is highlighted, focusing on the incorporation of additives and interlayers to enhance device performance. The inclusion of PCBM as an interlayer between C_{60} and $CsPbI_3$ was confirmed to play a pivotal role in improving energy level alignment, reducing defects, and facilitating more efficient charge transfer at the interface. However, the introduction of TTH as a novel interlayer demonstrated even greater benefits, including enhanced V_{oc}, FF, and overall power PCE of 8.12%. The zwitterionic character of the excited state of TTH can induce an interfacial internal dipole moment that enhances material polarization and alters the electric field within the solar cell. This stronger electric field facilitates the separation of photogenerated charge carriers, effectively minimizing recombination losses and reducing resistive effects. The dynamic, light-responsive properties of TTH are thus critical for improving charge carrier dynamics in the device, leading to a noticeable increase in the V_{oc}.

The optimized TTH concentration (0.75 mg/mL) improved device performance by reducing interfacial recombination and enabling more efficient charge separation through the formation of a dipole in the excited state. Additionally, the optical and electronic characterization of TTH indicated its superior resistance to photobleaching compared to other radicals, supporting its potential as a stable and efficient interlayer.

Impedance spectroscopy revealed reduced recombination resistance and lower interfacial losses in devices incorporating TTH, aligning with the observed improvements in V_{oc} and FF. The enhanced photocurrent, particularly in the short-wavelength region, further underscored the role of TTH in improving charge collection and reducing nonradiative losses.

In conclusion, the integration of TTH into the PSC architecture provides a promising pathway for optimizing the efficiency, stability, and scalability of perovskite-based devices. These advancements make PSCs particularly suitable for energy harvesting applications, where their superior performance under low-light conditions can be leveraged for powering sensors, and other low-power electronics, driving innovation in sustainable indoor energy solutions.

4.4 References.

[1] Ion–Dipole Interaction Enabling Highly Efficient $CsPbI_3$ Perovskite Indoor Photovoltaics. Kai-Li Wang, Haizhou Lu, Meng Li, Chun-Hao Chen, Ding- Bo Zhang, Jing Chen, Jun-Jie Wu, Yu-Hang Zhou, Xue-Qi Wang, Zhen-Huang Su, Yi-Ran Shi, Qi-Sheng Tian, Yu-Xiang Ni, Xing-Yu Gao, Shaik M. Zakeeruddin, Michael Grätzel, Zhao-Kui Wang and Liang-Sheng Liao. Adv. Mater. 35 (2023) 2210106.

[2] Untapped Potentials of Inorganic Metal Halide Perovskite Solar Cells. Anita Ho-Baillie, Meng Zhang, Cho Fai Jonathan Lau, Fa-Jun Ma and Shujuan Huang. Joule 3 (2019) 938–955.

[3] Efficient and Stable Graded $CsPbI_{3-x}$ Br_x Perovskite Solar Cells and Submodules by Orthogonal Processable Spray Coating. Jin Hyuck Heo, Fei Zhang, Chuanxiao Xiao, Su Jeong Heo, Jin Kyoung Park, Joseph J. Berry, Kai Zhu, and Sang Hyuk Im. Joule 5 (2021) 481–494.

[4] Reduced-Dimensional a-$CsPbX_3$ Perovskites for Efficient and Stable Photovoltaics. Yuanzhi Jiang, Jin Yuan, Youxuan Ni, Jien Yang, Yao Wang, Tonggang Jiu, Mingjian Yuan and Jun Chen. Joule 2, (2018) 1356–1368.

[5] Inorganic caesium lead iodide perovskite solar cells. Giles E. Eperon, Giuseppe M. Paternò, Rebecca J. Sutton, Andrea Zampetti, Amir Abbas Haghighirad, Franco Cacialli and Henry J. Snaith. J. Mater. Chem. A. 3 (2015) 19688–19695.

[6] Myths and reality of $HPbI_3$ in halide perovskite solar cells. Weijun Ke, Ioannis Spanopoulos, Constantinos C. Stoumpos and Mercouri G. Kanatzidis. Nature communcitations. 9 (2018) 4785.

[7] The Role of Dimethylammonium Iodide in $CsPbI_3$ Perovskite Fabrication: Additive or Dopant? Dr. Yong Wang, Xiaomin Liu, Dr. Taiyang Zhang, Xingtao Wang, Miao Kan, Jielin Shi, Prof. Yixin Zhao. Angew. Chem. 131 (2019) 16844 – 16849.

[8] Chemical composition and phase evolution in DMAI derived inorganic perovskite solar cells. Meng H., Shao Z., Wang L., Li Z., Liu R., Fan Y., Cui G., and Pang S. ACS Energy Lett. 5 (2020) 263–270.

[9] Stabilizing $CsPbI_3$ perovskite for photovoltaic applications. Xue Tan, Shubin Wang, Qixian Zhang, Huicong Liu, Weiping Li, Liqun Zhu and Haining Chen. Matter 6 (2023) 691–727.

[10] Fluorine-Containing Passivation Layer via Surface Chelation for Inorganic Perovskite Solar Cells. Zhang, Hao; Xiang Wanchun; Zuo, Xuejiao; Gu Xiaojing; Zhang Shiang; Du Yachao; Wang Zhiteng; Liu Yali; Wu Haifeng; Wang Peijun; Cui Qingyue; Su Hang. Angewandte Chemie.62, (2023) e202216634.

[11] Highly Stable $CsPbI_3$ Perovskite Solar Cells with an Efficiency of 21.11% via Fluorinated 4-Amino-Benzoate Cesium Bifacial Passivation. Xu D., Wang J., Duan Y., Yang S., Zou H., Yang L., Zhang N., Zhou H., Lei X., Wu M. Advanced Functional Materials. 33 (2023) 2304237.

[12] Cs_4PbI_6-Cl Nucleation Seeds Assisted Highly Oriented Inorganic $CsPbI_3$ Perovskites for Efficient Perovskite Solar Cells. Shuang Li, Junming Qiu, Rongshan Zhuang, Qisen Zhou, Mingxu Zhang, Mubing Yu, Yong Hua and Xiaoliang Zhang. ACS Appl. Energy Mater 6 (2023) 3514−3524.

[13] Dual bulk and interface engineering with ionic liquid for enhanced performance of ambient-processed inverted $CsPbI_3$ perovskite solar cells. Kun Wang, Zeyuan Su, Yali Chen, Heng Qi, Ting Wang, Hao Wang, Youqian Zhang, Li Cao, Qian Ye, Fobao Huang, Yu Tong, Hongqiang Wang. Journal of Materials Science & Technology 114 (2022) 165–171.

[14] Understanding and Engineering the Perovskite/Organometallic Hole Transport Interface for High-Performance p−i−n Single Cells and Textured Tandem Solar Cells. Shaojie Yuan, Kaitian Mao, Fengchun Cai, Zhengjie Zhu, Hongguang Meng, Tieqiang Li, Wei Peng, Xingyu Feng, Weiwei Chen, Jiahang Xu, and Jixian Xu. ACS Energy Lett. 9 (2024) 3557−3566.

[15] Progress of inverted inorganic cesium lead halide perovskite solar cells. Kun Wang, Yu Tong, Li Cao, Sihong Yue, Yufeng Li, Chenxu Li, Mingyang Wu and Hongqiang Wang. Cell Reports Physical Science 4 (2023) 101726.

[16] Visualization and suppression of interfacial recombination for high-efficiency large-area pin perovskite solar cells Stolterfoht, M.; Wolff, C. M.; Márquez, J. A.; Zhang, S.; Hages, C. J.; Rothhardt, D.; Albrecht, S.; Burn, P. L.; Meredith, P.; Unold, T.; Neher, D.. Nat. Energy. 3 (2018) 847−854.

[17] Polishing the Lead-Poor Surface for Efficient Inverted $CsPbI_3$ Perovskite Solar Cells. Sheng Fu, Jiabo Le, Xueming Guo, Nannan Sun, Wenxiao Zhang, Weijie Song, and Junfeng Fang. Adv. Mater. 34 (2022) 2205066.

[18] In Situ Surface Sulfidation of $CsPbI_3$ for Inverted Perovskite Solar Cells. Xuemin Guo, Chunyan Lu, Wenxiao Zhang, Haobo Yuan, Hui Yang, Acan Liu, Zhengbo Cui, Wen Li, Yuyang Hu, Xiaodong Li, and Junfeng Fang. ACS Energy Lett. 9 (2024) 329−335.

[19] Surface-Defect Control via Designed Passivation for High-Efficiency Inorganic Perovskite Solar Cells. Xiaojing Gu, Prof. Wanchun Xiang, Prof. Qingwen Tian, Prof. Shengzhong (Frank) Liu. Angew. Chem. Int. 60 (2021) 23164 –23170.

[20] Inorganic wide-bandgap perovskite subcells with dipole bridge for all-perovskite tandems. Tiantian Li, Jian Xu, Renxing Lin, Sam Teale, Hongjiang Li, Zhou Liu, Chenyang Duan, Qian Zhao, Ke Xiao, Pu Wu, Bin Chen, Sheng Jiang, Shaobing Xiong, Haowen Luo, Sushu Wan, Ludong Li, Qinye Bao, Yuxi Tian, Xueping Gao, Jin Xie, Edward H. Sargent and Hairen Tan. Nature Energy. 8 (2023) 610–620.

[21] Exploring the Charge-Transport and Optical Characteristics of Organic Doublet Radicals: A Theoretical and Experimental Study with Photovoltaic Applications. Mariia Stanitska, Rasa Keruckiene, Gjergji Sini, Dmytro Volyniuk, Arunas Marsalka, Zhong-En Shi, Chung-Ming Liu, Yan-Ru Lin, Chih-Ping Chen and Juozas V. Grazulevicius. ACS Appl. Mater. Interfaces. 16 (2024) 41230−41243.

[22] Radical reinforced defect passivation strategy for efficient and stable $MAPbI_3$ perovskite solar cells fabricated in air using a green anti-solvent process. Pengfei Xie, Hui Xiao, Ying Qiao, Geping Qu, Jiangzhao Chen, Xiaoyuan Liu, Zong-Xiang Xu. Chemical Engineering Journal. 462 (2023) 142328.

[23] Organic radicals for the enhancement of oxygen reduction reaction in Li–O_2 batteries. A. Y. Tesio, D. Blasi, M. Olivares-Marín, I. Ratera, D. Tonti and J. Veciana.. Chem. Commun. 51 (2015) 17623-17626.

[24] Dark State of the Thiele Hydrocarbon: Efficient Solvatochromic Emission from a Nonpolar Centrosymmetric Singlet Diradicaloid. Angela Punzi, Yasi Dai, Carlo N. Dibenedetto, Ernesto Mesto, Emanuela Schingaro, Tobias Ullrich, Marinella Striccoli, Dirk M. Guldi, Fabrizia Negri, Gianluca M. Farinola and Davide Blasi. J. Am. Chem. Soc. 145 (2023) 20229−20241.

[25] Classification and quantitative characterisation of the excited states of π-conjugated diradicals. Lujo Matasović, Hugo Bronstein, Richard H. Friend and Felix Plasser. Faraday Discuss. 254 (2024) 107-129.

[26] A Versatile Molten-Salt Induction Strategy to Achieve Efficient $CsPbI_3$ Perovskite Solar Cells with a High Open-Circuit Voltage >1.2 V. Yuqi Cui, Jiangjian Shi, Fanqi Meng, Bingcheng Yu, Shan Tan, Shan He, Chengyu Tan,Yiming Li, Huijue Wu, Yanhong Luo, Dongmei Li and Qingbo Meng. Adv. Mater. 34 (2022) 2205028.

[27] Cesium lead halide perovskites with improved stability for tandem solar cells. Beal, R., Slotcavage, D., Leijtens, T., Bowring, A., Belisle, R., Nguyen, W., Burkhard, G., Hoke, E., and McGehee. J. Phys. Chem. Lett. 7 (2016) 746–751.

[28] Assisted Chlorination with Solid Protection Strategy for Efficient Air-Fabricated Inverted $CsPbI_3$ Perovskite Solar Cells. Sheng Fu, Wenxiao Zhang, Xiaodong Li Jianming, Guan Weijie, Song Junfeng Fang. Humidity- ACS Energy Letters. 6 (2021) 3661−3668.

[29] Impedance Spectroscopy Measurements in Perovskite Solar Cells: Device Stability and Noise Reduction. Didac Pitarch-Tena, Thi Tuyen Ngo, Marta Vallés-Pelarda, Thierry Pauporte, Iván Mora-Seró. ACS Energy Lett. 3 (2018) 1044.

[30] An Equivalent Circuit for Perovskite Solar Cell Bridging Sensitized to Thin Film Architectures. Yoo, S.-M.; Yoon, S. J.; Anta, J. A.; Lee, H. J.; Boix, P. P.; Mora-Seró, I. Joule 3 (2019), 2535-2549.

[31] Cesium lead halide perovskites with improved stability for tandem solar cells. Beal, R., Slotcavage, D., Leijtens, T., Bowring, A., Belisle, R., Nguyen, W., Burkhard, G., Hoke, E., and McGeheeJ. Phys. Chem. Lett. 7 (2016) 746–751.

[32] Impedance Spectroscopy Measurements in Perovskite Solar Cells: Device Stability and Noise Reduction. Didac Pitarch-Tena, Thi Tuyen Ngo, Marta Vallés-Pelarda, Thierry Pauporte, Iván Mora-Seró. ACS Energy Lett. 3 (2018) 1044.

Chapter 5

Plasma Treatment: A Sustainable Approach to hybrid Perovskite surface Engineering.

In this chapter I explore the effect of mild plasma treatments on the surface of MAPI perovskite and rationalize the effect on the surface chemistry and device performances.
Literature offers a fragmented and sometimes contradictory set of observations, a clear and comprehensive understanding of the effects of plasma treatments on perovskite surfaces remain elusive, leaving many promising research opportunities still unexplored. Four different gases are tested: Ar, H_2, N_2 and O_2. Ar plasma is chosen to explore the ion bombardment effect, excluding the chemical modification of the surface due to the absence of chemically active species in this plasma. H_2 plasma is chosen to explore the effect that a reducing environment can have on the perovskite surface. N_2 plasma is explored because of its potentially good affinity with a perovskite as $MAPbI_3$, containing nitrogen atoms. The O_2 plasma is explored for possible oxidative passivation of perovskite surface. This work provides a detailed understanding of the plasma-induced surface modifications, serving as a base for the development and engineering of plasma-controlled MAPI surfaces for efficient optoelectronic devices.

5.1 State of the art and premises.

5.1.1 Methylammonium lead iodide perovskite (MAPI)

MAPI has emerged as the most extensively studied material in the field of perovskite-based optoelectronics. Serving as the archetypal perovskite, it has been widely used as a model system to explore and understand the fundamental properties of hybrid perovskites. Among its distinctive features are a high absorption coefficient, an optimal direct bandgap of approximately 1.55 eV [1,2], remarkable charge carrier diffusion lengths, high ambipolar charge mobilities [3], and extended charge carrier lifetime [4]. These factors make $MAPbI_3$ not only a valuable tool for fundamental scientific research but also a key component for the development of high-performance optoelectronic devices. Despite the high PCE and excellent optoelectronic properties, MAPI-based PSCs suffer from poor structural and chemical stability because of the tendency of the MAPI to decompose into non-photoactive PbI_2 when exposed to environmental conditions such as ambient moisture and heat, as already been discussed in the

introductory section. Furthermore, the MAPI-based PSCs can undergo rapid performance degradation, especially under applied electric fields with illumination, because of ion migration and accumulation at the device interfaces.

The surface defects in perovskite materials are charged due to their ionic nature, distinguishing them from the dangling bonds typically found in traditional semiconductor materials like silicon. This difference necessitates distinct passivation strategies. To date, numerous materials have been explored for their ability to interact with these charged defects, acting as electron or hole acceptors to passivate the associated charge traps.

For instance, π-conjugated Lewis bases, a class of organic semiconducting molecules featuring Lewis base groups, have been introduced to effectively passivate Lewis acid traps, such as undercoordinated Pb ions and Pb clusters. However, many passivation molecules are effective only against specific types of defects. For example, phenyl-C_{61}-butyric acid methyl ester ($PC_{61}BM$) has been shown to effectively passivate certain lead-based defects, including Pb–I antisite defects and undercoordinated Pb atoms [5]. Despite this, the more complex and common deep traps on the surface of perovskite films, such as interstitial Pb (Pb_I), Pb clusters, and iodine-related defects (I_{MA}), remain challenging to address comprehensively. If the organic components, such as the MA cation and the I anion, were eliminated, the I_{MA} defect could potentially be removed. This would leave a lead-rich perovskite surface that could be effectively driven using well-known electron transport materials like fullerenes. Thermal annealing has been employed to remove methylammonium iodide (MAI) and adjust the film composition. However, $MAPbI_3$ tends to decompose easily during thermal annealing, and this decomposition can occur deep within the material, beyond the reach of the charge transport layer, leading to significant charge recombination issues [6].

5.1.2 Plasma technology.

The surface morphology and chemical composition of perovskite films are critical parameters that significantly impact the performance of PSCs. Several surface modification techniques have been explored to optimize these properties, including vacuum flash-assisted, gas-assisted, and plasma-assisted solution processes. Among these, plasma technologies have recently garnered attention for their unique capability to modify materials under diverse conditions.

Plasma-surface interactions, influenced by sheath voltage, power density, and plasma pressure, enable precise control over material properties [7,8]. Non-equilibrium ("cold") plasmas have become a focus of research due to their ability to achieve surface treatments and thin-film deposition in very mild conditions. In these plasmas, the primary energy carriers are electrons, while heavier particles (ions, gas atoms, and molecules) remain relatively "cold" [9]. Plasma treatment represents a sustainable and environmentally friendly approach to material modification, especially for halide perovskites like MAPI. Crucially, plasma-based processes produce minimal waste and consume relatively low energy, aligning with the principles of green chemistry and sustainable manufacturing. This makes plasma treatment an ideal choice for advancing the scalability and eco-friendliness of perovskite-based technologies, including solar cells and optoelectronic devices. The growing interest in plasma-assisted treatments for MAPI reflects the versatility and potential of this technology to enhance perovskite surface properties, paving the way for improved device performances. In this context, only a handful of reports has dealt with the interaction between plasma and perovskite materials. Masoud et al. [10] reported on the effect of ambient air plasma treatment on the properties of methylammonium

lead halide perovskite films. A remarkable change in the energy bands, depending on treatment time, was observed. Short plasma treatments ($\leq$ 5 s) led to a widening of the band gap, probably due to a higher carrier concentration, while longer plasma treatment (> 5 s) led to a narrowing of the band gap. In addition, short plasma treatments were able to increase perovskite crystallinity, as proved by XRD measurements, while long treatment times created a non-homogeneous etched surface. Xiao et al. [6] proposed the use of argon plasma as a tool to remove methylammonium and iodine ions to leave a lead-rich perovskite surface, which could be better passivated by electron transport materials, as fullerene derivatives. XPS measurements indicated a reduction of the carbon, nitrogen, and iodine superficial content and the formation of metallic lead. Furthermore, by using the thermal admittance spectroscopy, the Ar-plasma treated perovskite showed a lower trap density of states, which could probably help fullerenes to diffuse into the grain boundaries (GBs), to passivate the shallow trap located at the GBs, as well as passivate the deep trap at the surface. The resulting device showed an improved PCE of 18.4%, higher than the 16.3% of the untreated device. A different plasma was used by Kim et al. [11], namely an atmospheric hydrogen-plasma, to etch MAPI films. In this study, the plasma is not used to enhance the surface properties or for passivating purposes, but only to etch the perovskite surface, as an effective and economic way to pattern the material [12]. Plasma treatment times shorter than 180 s are found to etch the surface without altering the surface chemistry, while longer treatment times led to cluster formation and film decomposition.

5.2 Experimental Results and discussions.

MAPI surface is known for its dynamic nature, characterized by labile halide ions, ionic defects, and grain boundaries that significantly influence the material's optoelectronic properties (as discussed in Chapter 1). Plasma treatments offer a controlled approach to modifying these surface characteristics, enabling the potential to reduce surface defects, passivate trap states, or engineer specific functionalities. For instance, the treatment times are varied from a minimum of 2 to a maximum of 30 seconds, depending on the incidence of the specific gas. Ar plasma-induced ion bombardment primarily affects surface roughness and void fraction, while the H_2 plasma can chemically interact with halide ions, potentially stabilizing or restructuring the surface. N_2 plasma may preferentially interact with nitrogen-containing sites, subtly altering the defect landscape. O_2 plasma, on the other hand, is expected to promote oxidative reactions, leading to the formation of passivating layers such as PbO, which could enhance stability or, conversely, degrade the active surface depending on the exposure time.

5.2.1 Morphological analysis.

SEM is performed to investigate potential morphological changes on the surface of MAPI induced by plasma treatments. The analysis includes the pristine sample (*Figure 5.1a*) as a reference, as well as samples treated for 2 s, 10 s, and 30 s with different gases (*Figure 5.1b-d*). This comprehensive approach allows for the observation and comparison of surface modifications over varying treatment durations and under distinct plasma environments.

After just 2 seconds of Ar plasma treatment (*Figure 5.1b*), the grain boundaries of the perovskite no longer appear sharp, as in the pristine sample. Longer treatment times lead to the formation of nano-sized domains and the complete disappearance of the large perovskite grains (*Figure 5.1c-d*). SEM images of H_2 plasma-treated samples show a clear morphological change after only 2 s, with a significant reduction in grain size (*Figure 5.1b*). Similar results are reported by

Khachatryan et al. [8] when studying the etching effect of atmospheric pressure hydrogen plasma on MAPI films. In all H_2 plasma-treated samples, the grains become indistinguishable, highlighting the strong impact of hydrogen plasma on the perovskite surface (*Figure 5.1c*).

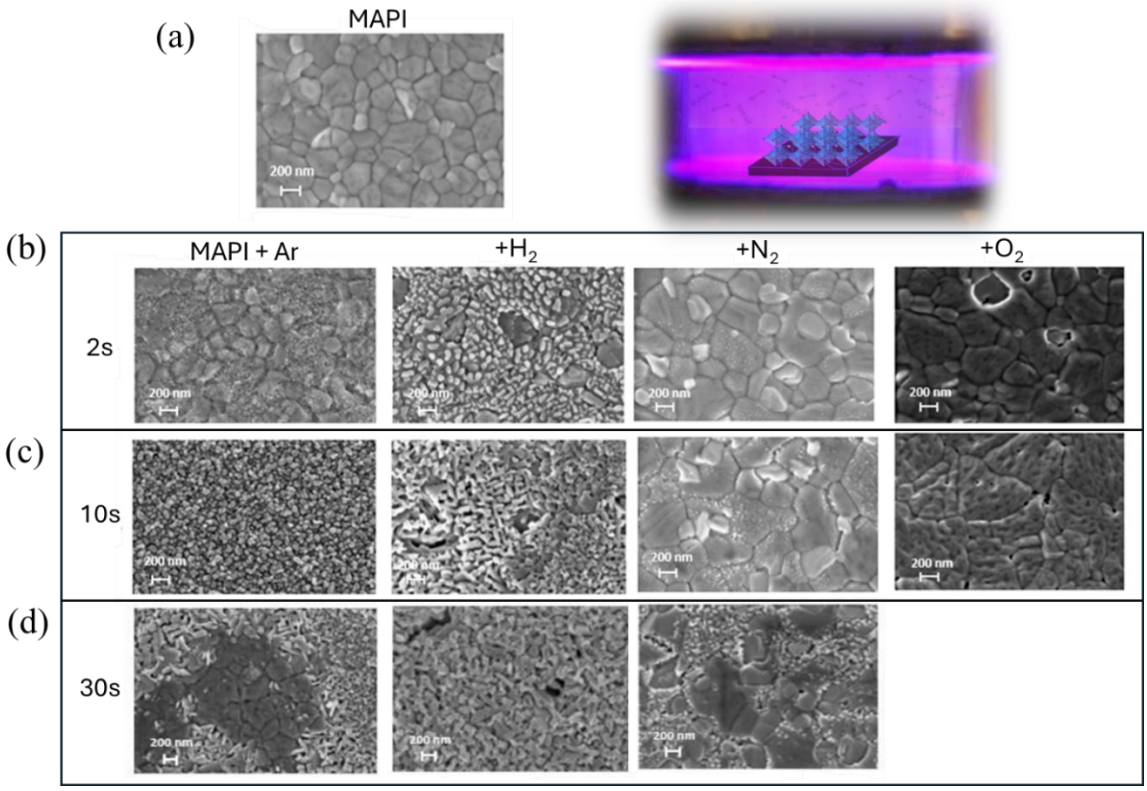

Figure 5.1 (a) SEM images of pristine MAPI and schematization of the sample treatment. (b)Samples treatment after 2 s with Ar, H_2 and O_2. (c) Samples treatment after 10 s with Ar, H_2 and O_2. (d) Samples treatment after 30 s with Ar and H_2 gases.

N_2 plasma, on the other hand, has a less drastic effect on the surface morphology. After 10 seconds of treatment, the perovskite grains are still well-defined, with only a minor modification observable, while an evident modification is detectable only for the sample treated for 30 s (*Figure 5.1d*). Interestingly, for the samples treated for 2 and 10 seconds, only some of the crystal grains show brighter spots on their surface, while others appear unaffected by the plasma. This suggests that certain crystal facets may be more vulnerable to the N_2 plasma environment than others, as reported for moisture-induced degradation on $FAPbI_3$ films [13]. Specifically, the (100) facet is more susceptible to degradation than the (111) facet. This could explain the observed variation in N_2/perovskite interactions, as the surface distribution of facets may vary from one film to another.

The SEM images up to 10 seconds of treatment show strong morphological changes on the perovskite surface for all gases. These changes cannot be attributed to thermal effects, as the plasma conditions (reactor type, RF input power, and pressure) typically result in a gas temperature not exceeding 50-60°C.

O_2 plasma exhibits peculiar behavior; after 2 seconds of treatment (*Figure 5.1b*), the surface appears selectively damaged, while the grains seem to melt after 10 seconds of treatment (*Figure 5.1c*). After the treatment, darker regions are homogeneously distributed across the surface, suggesting the localized removal of material.

5.2.2 Devices integration.

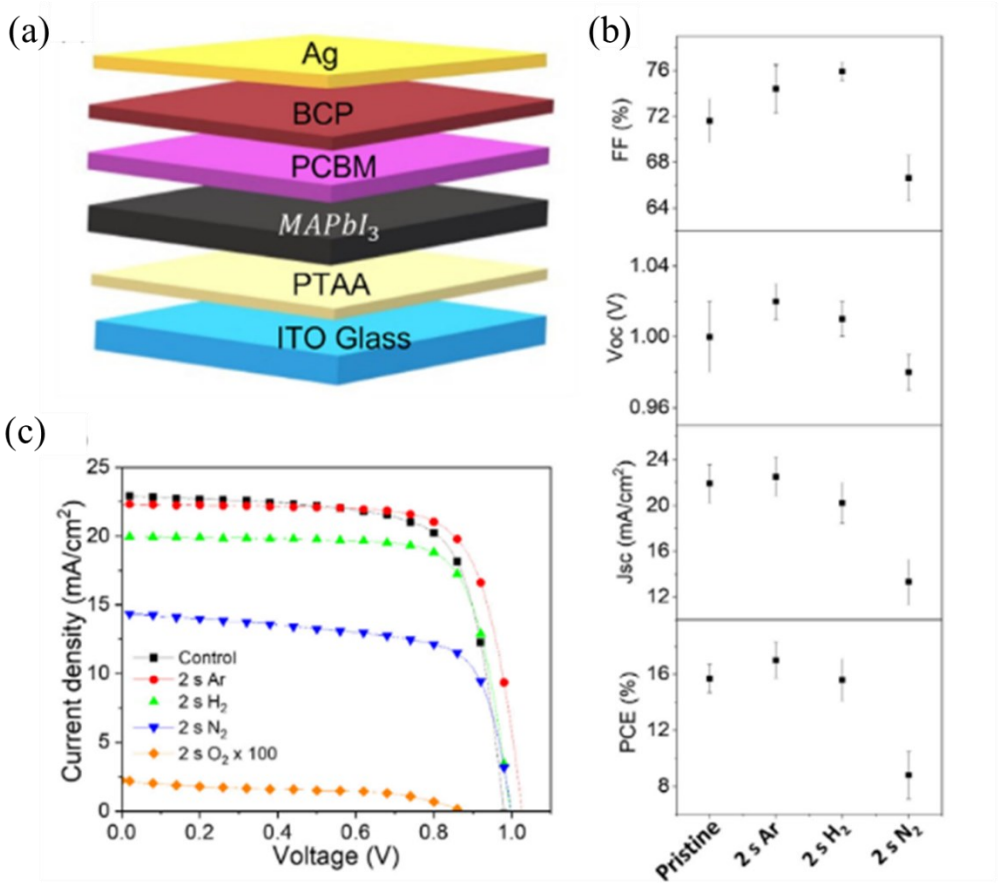

Figure 5.2 a) Device architecture; b) J-V curves of solar devices; c) device parameters and statistics for the reference and the plasma-treated films(oxygen-treated samples have been removed for clarity).

Plasma-treated perovskite films, along with untreated ones for comparison, are incorporated into photovoltaic devices with an inverted p–i–n architecture, as illustrated in *Figure 5.2a* (Chapter 2 for details). Based on morphological observations, only the 2 s plasma treatment is utilized for device fabrication, while longer exposures are excluded due to their pronounced impact on film morphology. Notably, increased surface roughness is observed after extended treatments, which could negatively influence device interfaces (refer to SEM images in *Figure 5.1c,d*).

The average values and standard deviations of the photovoltaic parameters are shown in *Figure 5.2b* and the J–V curves of the best-performing devices are presented in *Figure 5.2c*, while accounting for factors affecting device reproducibility. A comparison of the average PCE values reveale a slight yet statistically significant improvement in the performance of devices containing Ar plasma-treated films ($17.0 \pm 1.3\%$) compared to control devices ($15.7 \pm 1.0\%$). Devices with H_2 plasma-treated films exhibit similar performance to the controls ($15.6 \pm 1.5\%$), indicating the benign nature of H_2 plasma despite the significant morphological alterations.

An overall enhancement in the FF is observed in devices incorporating Ar- and H_2-treated films, which is attributed to the passivation of defects in the absorber material. Conversely, N_2 plasma-treated films result in reduced performance, with a PCE of $8.8 \pm 0.7\%$ and a significantly lower extracted current. In the case of O_2 plasma-treated devices, the current is nearly eliminated, and

the PCE drops to near zero. Despite the minimal morphological changes observed for films treated with N_2 and O_2, the decline in performance is likely due to surface modifications adversely affecting interface properties within the devices.

5.2.3 Optical characterizations.

The superficial nature of the modifications to the perovskite layer is demonstrated by the optical properties obtained through UV–VIS analysis (*Figure 5.3a*). All UV–vis spectra display consistent features, including an absorption onset around 780 nm, characteristic of MAPI perovskite [1,14]. The energy gap values derived from Tauc plots remain unchanged, confirming the preservation of the material's bulk optoelectronic properties.

Spectroscopic ellipsometry is used for a detailed analysis of the optical properties of both the surface layers and the bulk material separately. The absorption coefficient is determined through these measurements, and it is important to note that the adopted model, as described in Chapter 2, enables the separation of the optical properties of the bulk material from those of the surface layer, isolating the plasma effect. The trends of the absorption coefficient for the surface layer of all gases are shown in *Figures 5.3b.*

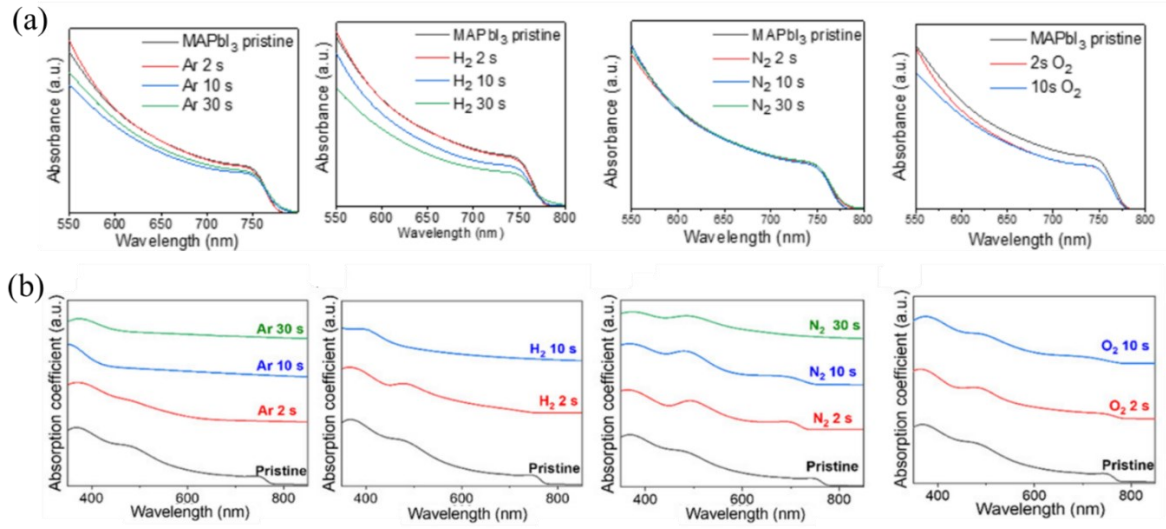

Figure 5.3 (a) UV-VIS absorption spectra and (b) Ellipsometry-derived surface layer absorption coefficient spectra of pristine MAPI and of samples after Ar; H_2 ;N_2 and O_2 plasma treatment.

For Ar plasma, the absorption spectra and the values of n and k as a function of wavelength for the pristine MAPI layer show the critical points at E_0 = 1.55 eV, E_1 = 2.5 eV, and E_2 = 3.4 eV, in agreement with ellipsometry analyses reported for MAPI [15, 16]. The surface layers exhibit lower absorption due to the presence of modeled voids, but they still show the same absorption peaks as the modeled bulk layers. The void fraction refers to the proportion of empty spaces (voids) within a material, in this case, the surface of the perovskite layer. These voids influence the optical properties of the material. Due to the crystal sizes being close to the wavelength used in the ellipsometric analysis, the void fraction in the EMA (Effective Medium Approximation) model is left unconstrained during the modeling to avoid the emergence of sub-bandgap absorption, along with a decrease in absorption relative to the E1 peak. With longer treatment times, sub-bandgap absorption increases, and the E1 peak is further suppressed, along with a decrease in the E2 peak. The E0 absorption is still present but

significantly reduced, and this is attributed to the reduction in crystal size following plasma exposure, along with an increase in roughness, highlighting the model's sensitivity in identifying surface modifications.

In the case of the N_2 plasma-treated films (*Figure 5.3b*), the intensity of E0, E1, and E2 obtained through ellipsometry measurements remains almost unchanged for 2 and 10 s, in accordance with the slight surface modifications observed in the SEM analysis. However, a slight blueshift in the bandgap is observed for the plasma-treated films compared to the pristine sample, presumably attributable to the chemical changes induced by the N_2 plasma. The sample treated for 30 s shows a sudden reduction in E0 absorption due to the reduction in crystal size and the increase in surface roughness, as monitored with SEM analysis, and an increase in the void fraction (from 26% in the pristine sample to 48%).

Ellipsometry gives a different response for the O_2 plasma-treated samples, as shown in *Figure 5.3b*. The void fraction tends to decrease with plasma exposure time (from 29% to 17% after 10 s of treatment), indicating a densification of the surface layer. Furthermore, the refractive index of the modeled surface layer is found to be comparable (2.33 for the O_2 plasma treatment vs 2.37 for the pristine MAPI surface, accounting for the void fraction) across the entire wavelength range explored. No sub-bandgap absorption is modeled, indicating lower surface roughness of the perovskite, as also observed in the SEM analysis. Finally, the critical points retain their position and intensity, except for the bandgap, which undergoes widening and a redshift after the first exposure to oxygen plasma, with no significant changes over the exposure time. The formation of a PbO layer is hypothesized, which could shield the perovskite surface from further plasma damage, unlike the other treatments that etch and dramatically modify the material's surface.

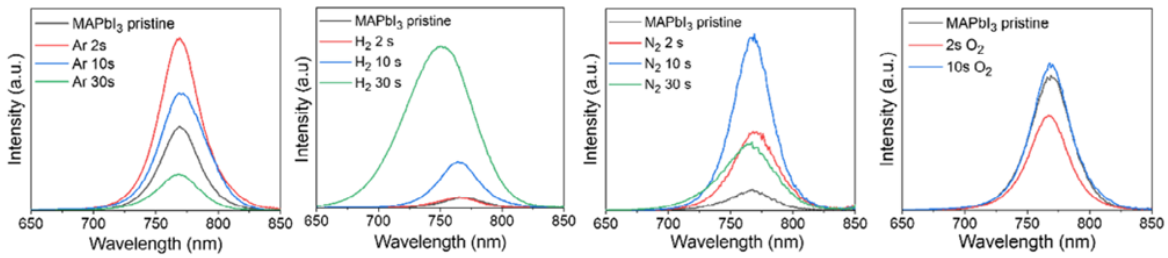

Figure 5.4 Steady state PL spectra of pristine MAPI and of samples after Ar; H_2; N_2 and O_2 plasma treatment.

Optical analysis was completed by PL investigation to provide information about defects and charge-trapping states within the perovskite film (*Figure 5.4*). All treated samples, except the 30 s one, show a more intense PL emission than the pristine material, with the highest value after processing of only 2 s. The increased emission suggests efficient reduction of electronically active surface defects. In contrast, a longer treatment time shows a monotonic reduction of the emission intensity, in line with the deterioration of the MAPI surface. H_2 - treated films show a continuous improvement of PL emission with time. Peculiar is the sample treated with H_2 plasma for 30 s, showing a much higher emission and a blue shift of about 20 nm, which is usually associated with suppressed non-radiative recombination due to reduced surface defects [17].

The trend in PL with N_2 plasma treatment time is not reproducible over different samples. However, a decrease in PL emission is observed after the same N_2 plasma treatment on a

different batch. This suggests a nontrivial and complex interaction between the perovskite and N_2 plasma.
Finally, O_2 plasma-treated MAPI shows an unclear trend in PL emission as a function of the treatment time, however, significantly worsening the PL intensity.

5.2.4 Chemical Characterization.
XPS analyses are carried out to gain more insight into the surface chemical modifications upon plasma treatment. The XPS spectrum for a typical MAPI perovskite shows peaks at binding energies of 533 eV, 403 eV, and 284.8 eV corresponding to the photoelectron peaks of O 1s, N 1s, and C 1s, respectively (*Figure 5.5*). The doublet peaks of I and Pb are located around 619 eV and 139 eV, respectively, with their associated spin-orbit splitting, according with literature [18]. To evaluate the chemical changes in our MAPI films produced with plasma gases treatment, it is recorded the high-resolution photoelectron spectra of each sample.

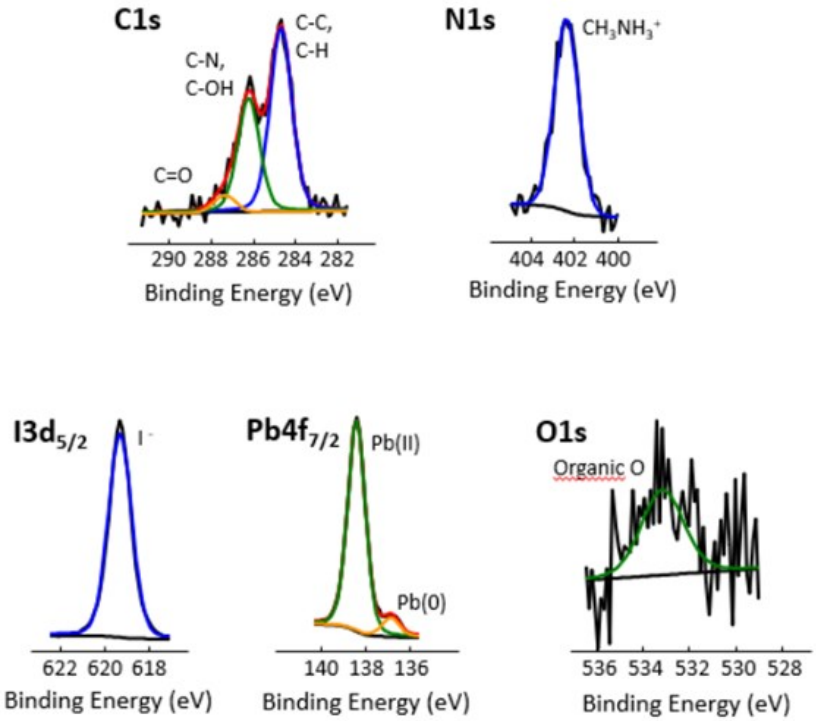

Figure 5.5 XPS high-resolution of pristine MAPI.

The atomic concentrations of the functional groups derived from the high-resolution XPS peaks of carbon, nitrogen, lead and iodine are reported in *Figure 5.6*, as a function of the plasma treatment time. The superficial atomic concentration of nitrogen tends to decrease for all gases, whereas carbon decreases in all cases except for N_2, as will be discussed later in the text. The reduction of nitrogen as a function of the treatment time is compatible with the removal of the methylammonium cation. For Ar plasma (*Figure 5.6a,b*), oxidized carbon is formed and increases as a function of the plasma treatment, together with an increased oxygen concentration. C–O (286.0 eV) tends to decrease in favor of more carbonyl (287.1 eV) and carboxyl (288.8 eV) moieties at the surface level. Their formation is due to the exposure of the perovskite layers to air after the treatment, as the Ar plasma alone cannot introduce additional chemical moieties at the perovskite surface but can only contribute, via ion bombardment, to

the aforementioned morphological changes. For a longer treatment time, the formation of lead oxide and hydroxide is found, as retrieved from the components at 529.5 and 531.5 eV, respectively. These findings suggest that, after the removal of methylammonium cations caused by ion bombardment, the inorganic surface becomes further activated, leading to a reaction of the exposed lead rich surface with oxygen containing species from the air. [I]-to-[Pb(II)] ratio, calculated from the high resolution peaks at 619.3 eV (iodine) and 138.4 eV(lead(II)), decreases from 2.6 to 2.4, showing a general decrease of iodine(*Figure 5.6*). While for the Ar plasma treatment, an interplay between surface activation and air exposure accounts for the surface chemical modification; for the other gases, additional chemical functionalities are measured which are also induced by the reactive plasma chemistry during treatment. In the H_2 treated samples (*Figure 5.6c,d*), an increase of Pb (II) (138.5 eV) can be observed after 30 s of treatment caused by the reducing nature of H_2 plasma. In the H_2-treated samples, an increase of Pb (II)(138.5 eV) can be observed after 30 s of treatment caused by the reducing nature of H_2 plasma in this case with simultaneous increase of Pb(0) (136.8 eV). The formation of Pb(0), together with the blueshift in UV–vis, was further observed by Jinet al. by exposing a perovskite surface-to-electron bombardment [17]. The blueshift is attributed to the exposure of a fresh surface with suppressed defects [5] after the knock-on effect induced by electrons. In a similar way, we observed a blue shift in a reducing environment, even though, in our case, the plasma dynamics and induced morphological changes make the deduction more complex.

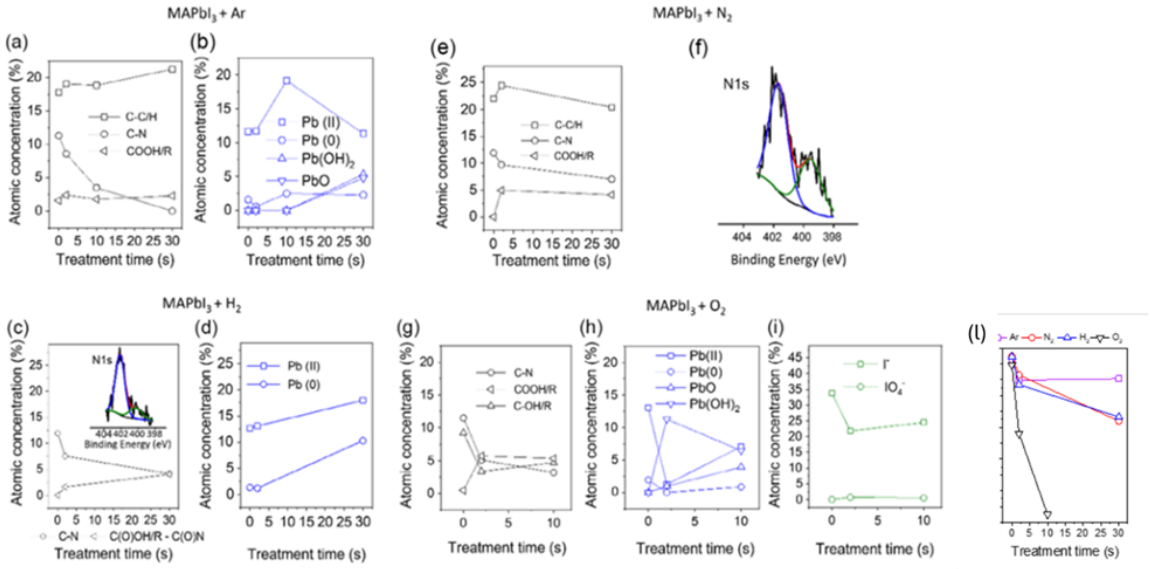

Figure 5.6 XPS atomic concentration as a function of plasma treatment time for a,b) Ar; c,d) H_2 ; e,f) N_2 ; g–i) O_2 plasma treatment (l) . [I]-to-[Pb(II)] ratio calculated for all the gases as a function of treatment time.

In addition, unlike Ar plasma, H_2 plasma treatment determines a reduction of the hydrocarbon component (284.8 eV), while as for the Ar plasma, there is an increase in surface C–O and carboxyl moieties. Furthermore, after 2 s of treatment, a new peak appears in the high-resolution N1s spectrum at low binding energy (400.3 eV), which can be attributed to an additional amide group. This counterintuitive oxidation of the amine can be explained not as the effect of the direct interaction between the H_2 plasma and perovskite surface, but more likely because of the interaction between the activated perovskite surface and the external ambient. Exposure of the activated surfaces in a controlled environment would help to isolate the effect of H_2 plasma

alone. The [I]-to-[Pb(II)] ratio decreases from 2.7 to 1.9, confirming a general decrease of the iodine content also in this case. Different from Ar and H_2 plasma, the N_2 -treated samples show a slight increase in surface carbon, originating from the external ambient, as shown in *Figure 5.6e,f*. Most likely, the increase of the carbon moieties plays a crucial role both for PL emission and for the device performances. In addition, a slight reduction of the C–N component and an increase of C–O and carboxyl moieties can be observed. After 30 s of treatment, a new peak appears at low binding energy (399.5 eV), as shown in the *Figure 5.6e*. This new functionality can be attributed to an additional amine group formed after exposure of the perovskite to the N_2 plasma, which may originate from the methylammonium ion decomposition or by the introduction of N-containing moieties on the adventitious carbon. Comparable to the other gases, [I]-to-[Pb(II)] ratio reduces from 2.7 to 1.9. O_2 plasma causes a decrease in carbon, nitrogen, and iodine with simultaneous increase in lead and oxygen surface concentration. A significant increase of carbonyl and carboxyl moieties can be observed after 10 s of treatment (*Figure 5.6g-i*). Notably, it is observed substantial increase in $Pb(OH)_2$, PbO, and IO_4 (624 eV) concentration. These moieties can form an insulating surface layer, which can hamper interfacial electron transfer from the perovskite to the PCBM electron transport layer, explaining the deterioration of the device performance. The [I]-to-[Pb(II)] ratio decreases from 2.6 to 0.7 after 10 s of treatment, pointing at a profound modification of the surface chemical composition. The formation of an insulating denser PbO layer on the surface of the MAPI is also in agreement with SEM images (*Figure 5.1*) and ellipsometry (*Figure 5.3*).

5.2.5 Theoretical Rationalization.

Short-time surface treatment with Ar plasma shows the removal MAI from the surface, leaving partially PbI_2-terminated grains. Density-functional theory (DFT) calculations predict adsorption energies of 0.69 eV for acetic acid and of 0.86 eV for formamide on a MAPI surface, representative for the experimentally observed carboxyl and carbonyl moieties (*Figure 5.7a,b*), respectively. Both species may passivate undercoordinated Pb surface atoms via formation of Pb─O bonds without introducing electronic states in the bandgap. The surface passivation likely causes enhanced PL (Figure 5.4) and improves the Voc and FF (*Figure 5.2*) at 2 s Ar plasma treatment. On longer time scales, hydroxide ions may accelerate surface degradation by deprotonation of the MA cation [19]. It is further expected to be a strong increase in defect density due to the reduction of grain size after 10 s, see Figure 5.1, as grain surfaces and GBs are sources of halide defects which may act as trap states.

H_2 plasma results in comparable changes such as for Ar plasma. In addition, H_2 plasma treatment reduces Pb(II) to metallic Pb(0). N_2 plasma introduces carboxyl moieties and additional amine groups (see *Figure 5.6e,f*). It is computed adsorption energies on PbI_2-terminated surfaces, matching the experimentally observed surface composition, for methylamine, dimethylamine, and trimethylamine of 0.85, 0.92, and 0.89 eV, respectively (*Figure 5.7c-f*).

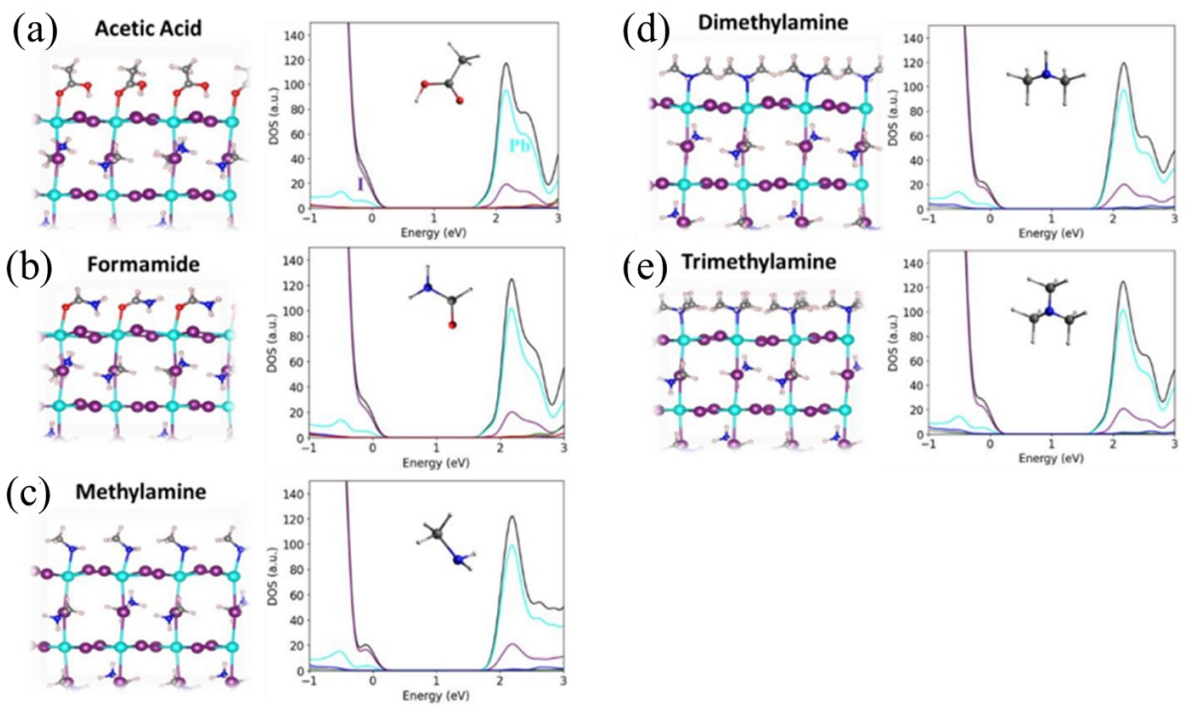

Figure 5.7 Geometric and electronic structure of adsorption on the PbI_2-terminated MAPI surfaces for following molecules: (a) Acetic acid; (b) formamide; (c) methylamine; (d) dimethylamine; (e) trimethylamine.

As for the acetic acid, all considered amines do not introduce gap states and passivate the undercoordinated Pb atoms via formation of strong Pb─N bonds, yielding the experimentally observed PL increase. The increased number of methyl groups, however, may weaken the binding of the perovskite with the transport layers, likely resulting in an increased surface resistance and consequently, as experimentally observed, reduced Jsc and FF. The increase in $Pb(OH)_2$ and PbO upon O_2 plasma treatment has also been observed in previous photo-oxidation experiments of MAPI [20,21] likely mediated through the light-induced formation of superoxide species. Thus, we may rationalize the formation of given lead oxide species due to electronic excitations of the O_2 molecules in the plasma environment.

The increase of these moieties can be responsible for the formation of an insulating layer on top of the perovskite surface, which hampers the electron transfer to the electron transport layer in PSCs. To the best of our knowledge, periodate, IO_4^-, has not been reported in perovskite degradation studies. It is performed DFT calculations to investigate IO_4^- formation and its impact on the electronic properties of MAPI. The oxidation of I^- at the MAI-terminated MAPI surface to IO_4^- consumes two oxygen molecules, following Equation 5.1.

$$I^- + 2O_2 \rightarrow IO_4^- \qquad (5.1)$$

The oxidation product bonds with an oxygen atom to the adjacent Pb ion, resulting in a Pb─O─I^- bond network (Figure 6.8a). Calculations suggest that Equation 6.1 is endothermic with calculated energy difference of $\Delta E = +0.29$eV, while previous studies reported an exothermic nature of IO_3^- formation [22]. The observation of IO_4^- by XPS, suggests that the aggressive plasma treatment is sufficient to activate the endothermic periodate formation, which otherwise may be ruled out under standard fabrication conditions. Interestingly, surface IO_4^- introduces electronic states in the bandgap at 0.4 eV above the valence band maximum of MAPI, see Figure 6.8b. Moreover, the assigned orbital is strongly localized on IO_4^- , see *Figure*

5.8a, which may consequently act as an electronic trap state and deteriorate the electronic performance of O_2 plasma-treated perovskite films.

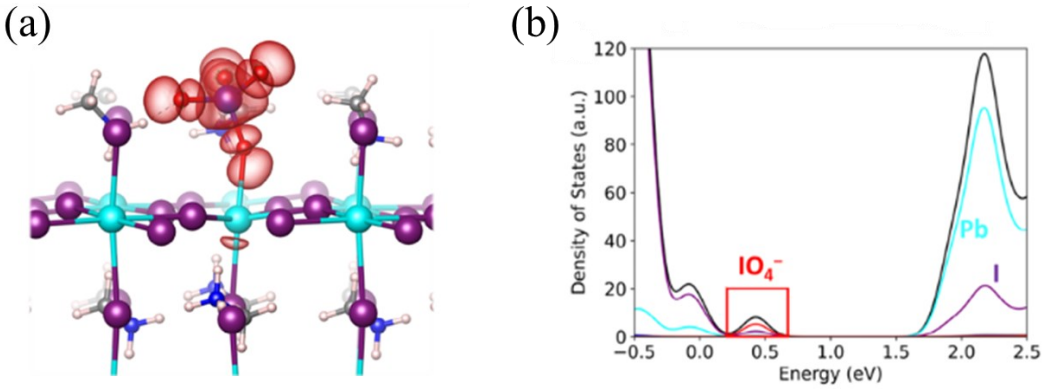

Figure 5.8 a) Visualization of unoccupied electronic state on surface IO_4^-.The color code is as follows: purple I; red O; cyan Pb; blue N; grey C; white H; b) density of states of the MAI-terminated MAPI with IO_4^-.

5.3 Conclusions.

In conclusion, the impact of various plasma treatments on MAPI surface has been evaluated and rationalized. The different plasma chemistries of the considered gases, Ar, N_2, H_2 and O_2 ,are found to differently affect the morphological, chemical, and optoelectronic properties of the perovskite films, as well as the performances of deriving MAPI-based p–i–n solar cells. The conditions associated with a more aggressive environment toward perovskite surface (Ar and H_2 gasses), in terms of organic component removal and film etching, are also the ones that more positively impact the corresponding device performances. The removal of the superficial organic components helps to better passivate the photoactive layer when included in the device structure, likely due to an enhanced coupling with electron-extracting PCBM layer. Another interesting aspect of the chemical modification induced by plasmas is the in situ generation of chemical functionalities (e.g., amides, amines) that change the energetic landscape of the interfaces, as confirmed by modeling. It is observed a general positive effect on the bandgap engineering with respect to PCBM. This positive effect is however counterbalanced by the surface activation, which, for mild plasma conditions, leads to the formation of an insulating layer likely deriving from the capture of environmental pollutants (N_2 gas). Noticeably, the controlled introduction of additional chemical functionalities at the perovskite surface, via plasma, opens novel possibilities for the MAPI surface engineering as an alternative, less invasive, and technologically mature route to classical wet chemistry. Finally, a peculiar behavior is observed when O_2 plasma is applied: the introduction of insulating $Pb(OH)_2$,PbO, and periodate IO_4^-. The electrical barrier generated by the formed compounds, in particular PbO, has a clear negative effect on the solar cell performances. This finding adds an important piece of information to the defect chemistry of perovskite materials: the oxidation of iodide resulting in periodate IO_4^- is possible in O_2 plasma conditions and despite showing substantial positive formation energies has never been reported so far as degradation intermediate in MAPI. Overall, these results underline the great potential of plasma-based treatment to passivate and functionalize the surface of MAPI; at the same time it raises the need for additional efforts in the engineering of the plasma conditions to minimize plasma damage and controlled surface modification.

5.4 References.

[1] Synthesis and crystal chemistry of the hybrid perovskite $(CH_3NH_3)PbI_3$ for solid-state sensitised solar cell applications. Tom Baikie, Yanan Fang, Jeannette M. Kadro, Martin Schreyer, Fengxia Wei, Subodh G. Mhaisalkar, Michael Graetzel and Tim J. White. J. Mater. Chem. A. 1 (2013) 5628–5641.

[2] Organic−Inorganic Perovskites: Structural Versatility for Functional Materials Design Bayrammurad Saparov and David B. Mitzi. Chem. Rev. 116 (2016) 4558−4596.

[3] Electronic Properties of Meso-Superstructured and Planar Organometal Halide Perovskite Films: Charge Trapping, Photodoping, and Carrier Mobility. Leijtens, T.; Stranks, S. D.; Eperon, G. E.; Lindblad, R.; Johansson, E. M. J.; McPherson, I. J.; Rensmo, H.; Ball, J. M.; Lee, M. M.; Snaith, H. J. ACS Nano. 8 (2014) 7147−7155.

[4] High Charge Carrier Mobilities and Lifetimes in Organolead Trihalide Perovskites. Wehrenfennig, C.; Eperon, G. E.; Johnston, M. B.; Snaith, H. J.; Herz, L. M. Adv. Mater. 26 (2014) 1584−1589.

[5] Origin and elimination of photocurrent hysteresis by fullerene passivation in $CH_3NH_3PbI_3$ planar heterojunction solar cells. Yuchuan Shao, Zhengguo Xiao, Cheng Bi, Yongbo Yuan and Jinsong Huang. Nature Communications 5 (2014) 5784.

[6] Argon Plasma Treatment to Tune Perovskite Surface Composition for High Efficiency Solar Cells and Fast Photodetectors. Xun Xiao, Chunxiong Bao, Yanjun Fang, Jun Dai, Benjamin R. Ecker, Congcong Wang, Yuze Lin, Shi Tang, Ye Liu, Yehao Deng, Xiaopeng Zheng, Yongli Gao, Xiao Cheng Zeng and Jinsong Huang. Adv. Mater. 30 (2018) 1705176.

[7] Surface Property Tuning of Methylammonium Lead Iodide by Plasma for Use in Planar Perovskite Solar Cells. Masoud Shekargoftar, Jan Pospisil, Jan Duga, Martin Weiter, and Tomaš Homola. ACS Omega. 5 (2020) 18384−18390.

[8] Novel method for dry etching $CH_3NH_3PbI_3$ perovskite films utilizing atmospheric-hydrogen-plasma. Hayk Khachatryan, Hyeong-Pil Kim, Sung-Nam Lee, Han-Ki Kim, Moojin Kim, Kyoung-Bo Kim, Jin Jang. Materials Science in Semiconductor Processing 75 (2018) 1-9.

[9] Plasma processes at atmospheric and low pressures. Ladislav Bardos, Hana Barankova´. Vacuum 83 (2009) 522–527.

[10] A Study on the Effect of Ambient Air Plasma Treatment on the Properties of Methylammonium Lead Halide Perovskite Films. M. Shekargoftar, J. Jurmanová, T. Homola. Metals (Basel) 9 (2029), 991.

[11] Properties of atmospheric-hydrogen-plasma-treated $CH_3NH_3PbI_3$ perovskite films. Hyeong-Pil Kim, Moojin Kim, Kyoung-Bo Kim, Hayk Khachatryan, Jin Jang. Surface and Coatings Technology. 330 (2017) 228-233.

[12] Plasma-Driven Atomic-Scale Tuning of Metal Halide Perovskite Surfaces: Rationale and Photovoltaic ApplicationAlberto Perrotta, Sara Covella, Francesca Russo, Fabio Palumbo, Antonella Milella, Vincenza Armenise, Francesco Fracassi, Aurora Rizzo, Silvia Colella,

Waldemar Kaiser, Asma A. Alothman, Edoardo Mosconi, Filippo De Angelis, and Andrea Listorti. Sol. RRL. 7 (2023), 2300345.

[13] Unveiling facet-dependent degradation and facet engineering for stable perovskite solar cells. C. Ma, F. T. Eickemeyer, S.-H. Lee, D.-H. Kang, S. J. Kwon, M. Grätzel, N.-G. Park, Science. 379 (2023) 173.

[14] Plasma-Deposited Fluorocarbon Coatings on Methylammonium Lead Iodide Perovskite Films. V. Armenise, S. Colella, A. Milella, F. Palumbo, F. Fracassi, A. Listorti. Energies. 15 (2022) 4512.

[15] Optical Transitions in Hybrid Perovskite Solar Cells: Ellipsometry, Density Functional Theory, and Quantum Efficiency Analyses for $CH_3NH_3PbI_3$. Masaki Shirayama, Hideyuki Kadowaki, Tetsuhiko Miyadera, Takeshi Sugita, Masato Tamakoshi, Masato Kato, Takemasa Fujiseki, Daisuke Murata, Shota Hara, Takurou N. Murakami, Shohei Fujimoto, Masayuki Chikamatsu, and Hiroyuki Fujiwara. Phys. Rev. Applied 5 (2016) 014012.

[16] A review of characterization of perovskite film in solar cells by spectroscopic ellipsometry. Huihui Li, Changcai Cui, Xipeng Xu, Subiao Bian, Chanisorn Ngaojampa, Pipat Ruankham, Atchara Punya Jaroenjittchai. Sol. Energy. 212 (2020) 48.

[17] Suppression of Phase Transitions in Perovskite Thin Films through Cryogenic Electron Beam Irradiation. B. Jin, D. Zhao, F. Liang, L. Liu, D. Liu, P. Wang, M. Qiu. Research. 2021(2021), 9797058.

[18] Understanding surface chemistry during MAPbI3 spray deposition and its effect on photovoltaic performance. Conor Rocks, Vladimir Svrcek, Paul Maguire and Davide Mariotti. J. Mater. Chem. C. 5 (2017) 902-916.

[19] Accumulation of Deep Traps at Grain Boundaries in Halide Perovskites. Ji-Sang Park, Joaquín Calbo, Young-Kwang Jung, Lucy D. Whalley and Aron Walsh. ACS Energy Lett. 4 (2019) 1321.

[20] Photo-oxidative degradation of methylammonium lead iodide perovskite: mechanism and protection. Y. Ouyang, Y. Li, P. Zhu, Q. Li, Y. Gao, J. Tong, L. Shi, Q. Zhou,C. Ling, Q. Chen, Z. Deng, H. Tan, W. Deng, J. Wang. J. Mater.Chem. A. 7 (2019) 2275.

[21] Light and oxygen induced degradation limits the operational stability of methylammonium lead triiodide perovskite solar cells. D. Bryant, N. Aristidou, S. Pont, I. Sanchez-Molina,T. Chotchunangatchaval, S. Wheeler, J. R. Durrant, S. A. Haque. Energy Environ. Sci. 9 (2016) 1655.

[22] Mechanism of Reversible Trap Passivation by Molecular Oxygen in Lead-Halide Perovskites. D. Meggiolaro, E. Mosconi, F. de Angelis. ACS Energy Lett. 2 (2017) 2794.

Chapter 6

Conclusions and final remarks.

The transition toward a "smart and sustainable" industry model, driven by the integration of advanced technologies, is critical in addressing global challenges such as energy demand growth and the depletion of non-renewable resources. Solar energy emerges as a cornerstone of this transition due to its abundance, cleanliness, and scalability. This dissertation addresses critical challenges in perovskite solar cells (PSCs), focusing on stability, performance, and scalability, through innovative strategies involving bio-inspired materials, advanced interlayers, and plasma-based surface engineering. By systematically exploring these strategies, this work advances the scientific understanding and practical applicability of PSCs. Each chapter provides unique insights into specific aspects of PSC technology, collectively forming a comprehensive framework for addressing the key limitations of these materials.

6.1 Summary of Key Findings.

Chapter 3 investigates the use of β-carotene and PHB as additives to improve the stability and performance of PSCs. Biomaterials offer several advantages: they are renewable, cost-effective, and readily available, making them a sustainable alternative to conventional materials. Their use aligns with eco-friendly principles, reducing carbon emissions during production and supporting a circular economy. Bio-derived materials are biodegradable and biocompatible, minimizing environmental impact throughout their life cycle.

β-carotene, inspired by natural photosynthetic processes, demonstrates an exceptional ability to mitigate oxidative stress, preserving the chemical integrity and optoelectronic properties of perovskite films. $MAPb(Br_{0.2}I_{0.8})_3$ devices treated with β-carotene achieve a PCE of around 20%, with a high V_{oc} of 1.2 V. In $FAPbI_3$ and $CsPbI_3$ perovskites, which are prone to moisture and thermodynamic degradation (transitioning from alpha to delta phases), PHB bio-additives contribute to defect passivation. PHB also improves grain size and increases charge carrier lifetimes, resulting in a PCE of 9.3%. Additionally, PHB's dual role as both an additive and flexible substrate highlights its versatility. However, concentration optimization proves crucial, as higher amounts of PHB lead to the formation of non-perovskite phases.

The integration of β-carotene and PHB in PSCs addresses the chemical, morphological, and mechanical challenges faced by perovskite materials. While β-carotene enhances chemical stability and optoelectronic properties, PHB contributes to improved morphology and flexibility. These additives collectively advance the potential of perovskite solar cells as sustainable, high-performance photovoltaic materials and provide valuable pathways for future innovation in the field.

Chapter 4 explores CsPbI3 as a promising alternative to the organic-inorganic halide perovskites used in PSCs. $CsPbI_3$ offers key advantages, including enhanced thermal stability, non-volatility, and a relatively wide bandgap (1.60–1.72 eV), making it suitable for indoor applications and as part of tandem solar cell configurations. However, $CsPbI_3$ faces challenges with phase instability, particularly with its black beta phase, which is essential for high efficiency but prone to degradation. This chapter introduces a novel approach for stabilizing the black beta phase by using $DMAPbI_3$ as a dual-purpose additive that both stabilizes the phase and provides a lead source. Additionally, DMACl is used as an additive to improve the crystallization of $CsPbI_3$ films, thereby optimizing the film morphology and surface quality, which contributes to higher device performance at the optimum concentration of 4% w/v.

The use of TTH, a novel diradicaloid interlayer, improves device stability and performance, achieving a PCE of 8.12% by reducing interfacial recombination and promoting efficient charge separation. This compound demonstrates superior resistance to photobleaching, a critical factor in improving long-term stability. By analyzing the performance of TTH-treated devices through impedance spectroscopy, reduced recombination resistance and lower interfacial losses are observed, contributing to the improved V_{oc} and FF. This research advances the potential of $CsPbI_3$-based PSCs, addressing the phase instability challenge and enhancing the overall efficiency and longevity of these devices.

From a sustainability perspective, plasma treatments offer a promising approach for improving PSCs with minimal environmental impact. The use of plasma processes does not require harmful solvents or chemicals, often involved in traditional surface treatments. Plasma treatment is a dry process that can be easily integrated into high-throughput manufacturing, making it both efficient and scalable. Additionally, plasma treatments can be precisely tuned to optimize surface passivation without introducing toxic byproducts, aligning with the principles of green chemistry and reducing the environmental footprint of PSC fabrication.

Chapter 5 explores the effects of plasma treatments on methylammonium lead iodide (MAPI) surfaces, showcasing the potential of plasma-based methods for surface functionalization and passivation. Different plasma chemistries, including Ar, N_2, H_2, and O_2, are found to have unique effects on the morphological, chemical, and optoelectronic properties of perovskite films. Treatment with argon (Ar) for 2 seconds results in the most significant improvements in device performance, particularly in PCE and FF. Longer plasma exposure times of 10 seconds or 30 seconds lead to noticeable morphological changes that negatively impact device efficiency. Ar and H2 plasma treatments are effective in removing surface organic components, improving the interaction with the PCBM electron-extracting layer, and boosting device performance.

N_2 plasma shows a more moderate effect, with minor changes in surface morphology, leading to a reduction in performance compared to Ar and H_2 treatments. While N_2 plasma does not induce significant morphological alterations, its impact on interface properties still contributes to lower performance. O_2 plasma treatment leads to the formation of insulating compounds like PbO and $Pb(OH)_2$, which reduce the overall efficiency of the devices. These results emphasize the beneficial effects of plasma treatments on surface properties while highlighting the importance of precise control to avoid undesirable outcomes.

6.2 Future works.

The findings of this dissertation open several pathways for future research aimed at further advancing the field of PSCs with a focus on improving stability, performance, and scalability. Building upon the insights gained from the bio-inspired additives, interlayers, and plasma treatments explored here, future work can be directed.

Given the wide bandgap of $CsPbI_3$, future research explores its integration into tandem solar cell configurations. This involves combining $CsPbI_3$-based PSCs with other photovoltaic technologies, such as silicon or perovskite-silicon tandem cells, to achieve higher efficiencies. In addition to conventional outdoor applications, integrating $CsPbI_3$-based PSCs in indoor applications, where lower light intensities and specific spectral conditions prevail, holds great promise. The ability of $CsPbI_3$ to perform well under low light conditions makes it an ideal candidate for indoor photovoltaic applications, such as in windows, smart buildings, and portable electronics.

While plasma treatment offers a promising pathway for large-scale production, future research focuses on scaling up the processes explored in this dissertation. Investigating the feasibility of integrating plasma treatments into continuous, roll-to-roll manufacturing processes is crucial for the commercial viability of PSCs. Additionally, exploring the combination of plasma treatments with other surface modification techniques, such as laser processing or solution-based approaches, could provide more efficient and cost-effective fabrication methods.

As the field of perovskite solar cells progresses, a more comprehensive life cycle assessment (LCA) should be conducted to evaluate the environmental impact of the new materials and fabrication techniques explored in this work. The LCA should focus on factors such as energy consumption, resource depletion, and the potential for recycling or disposal of PSCs at the end of their life cycle. This will guide the development of more sustainable production methods and materials, ensuring that PSCs remain a viable and eco-friendly energy solution.

6.3 List of publications and congresses.

The following is a collection of my three-year doctoral research:

-Plasma-Driven Atomic-Scale Tuning of Metal Halide Perovskite Surfaces: Rationale and Photovoltaic ApplicationAlberto Perrotta, Sara Covella, Francesca Russo, Fabio Palumbo, Antonella Milella, Vincenza Armenise, Francesco Fracassi, Aurora Rizzo, Silvia Colella, Waldemar Kaiser, Asma A. Alothman, Edoardo Mosconi, Filippo De Angelis, and Andrea Listorti. Sol. RRL. 7 (2023), 2300345.

- Mimicking Natural Antioxidant Systems for Improved Photostability in Wide-Band-Gap Perovskite Solar Cells. Francesco Bisconti, Mauro Leoncini, Salvatore Gambino, Nadir Vanni, Sonia Carallo, Francesca Russo, Vincenza Armenise, Andrea Listorti, Silvia Colella, Salvatore Valastro, Alessandra Alberti, Giovanni Mannino and Aurora Rizzo. ACS Nano. 18 (2024) 1573−1581

- Singlet diradicaloids as n-type passivating interlayer for $CsPbI_3$ perovskite solar cells. Francesca Russo, Davide Blasi, Sofia Masi, Edoardo Mosconi, Andrea Listorti, Ivan Mora-Sero and Silvia Colella (article in draft).

-Stabilizing the black-Phase of $CsPbI_3$ Perovskite by crystallization kinetics modulation. Francesca Russo, Elisabetta Fanizza, Francesco Fracassi, Aurora Rizzo, Andrea Listorti and Silvia Colella. Proceedings of Matsus nanoge 2023 (Pavia).

- Advancing Energy Harvesting: Strategies for Stability and Efficiency in $CsPbI_3$ Perovskite Thin Films. Francesca Russo, Elisabetta Fanizza, Gennaro Ventruti, Sofia Masi, Ivan Mora Serò, Francesco Fracassi, Andrea Listorti and Silvia Colella. Proceedings of E-MRS 2024 Spring Meeting (Strasburg).

-Enhancing $CsPbI_3$ Perovskite stability via Crystallization Kinetics Modulation. Francesca Russo, Elisabetta Fanizza, Gennaro Ventruti, Sofia Masi, Ivan Mora Serò, Francesco Fracassi, Andrea Listorti and Silvia Colella. Proceedings of Matsus nanoge 2024 (Barcellona).

Acknowledgments.

In questi tre anni, il percorso di crescita personale e professionale è stato un viaggio intenso, fatto di sfide, scoperte e continue evoluzioni. Il miglioramento non è un traguardo statico, ma un processo in continua trasformazione, che richiede dedizione, consapevolezza e il coraggio di mettersi sempre in discussione. Ogni difficoltà affrontata, ogni errore compreso e ogni successo raggiunto hanno contribuito a plasmare non solo le mie competenze, ma anche il mio carattere, insegnandomi il valore della resilienza, della curiosità e della perseveranza. Fondamentale in questo percorso è stato l'incontro con persone che, con la loro guida e il loro esempio, hanno reso questa crescita possibile.

Rivolgo la mia più profonda gratitudine al mio supervisore il Professor Listorti, un mentore illuminato la cui guida attenta e il costante incoraggiamento hanno reso questo percorso non solo possibile, ma anche incredibilmente stimolante.

Un ringraziamento speciale va alla Dott.ssa Colella, che incarna l'essenza più autentica dell'insegnamento. L'insegnamento non è semplicemente un trasferimento di informazioni, ma un incontro tra due persone: da un lato, chi desidera apprendere con curiosità e passione; dall'altro, chi si dedica con impegno a condividere non solo il proprio sapere, ma anche la propria esperienza umana e intellettuale. È in questa connessione profonda che si realizza la vera evoluzione, un cammino di conoscenza che si costruisce insieme e che lascia un segno indelebile.

Un ringraziamento alla Prof.ssa Fanizza, per la fiducia umana e scientifica. Per aver sempre creduto nelle mie possibilità ed essere stata sempre pronta a fornirmi una nuova prospettiva nei momenti di sconforto. Solo chi conosce il valore della delicatezza sa donarla agli altri.

Un ringraziamento all'azienda che ha collaborato a questo progetto di dottorato, Egg Plants con sede a Polignano. In particolare, al Dott. Carofiglio.

Un grazie al collegio di dottorato in ''Smart and Sustainable Industry'' e alla coordinatrice la Prof.ssa Ciminelli.

Ringrazio il gruppo di plasmi di Bari, di cui i capostipiti il Prof. Fracassi, il Prof. Favia, la Prof.ssa Milella ed il Dott. Palumbo per avermi sempre fatto sentire a casa. La Dott.ssa Armenise perché è stata per me più di una collega, ma una confidente e amica. Savino e Danilo, per la loro disponibilità che non conosce limiti.

Le mie colleghe ed il mio collega di laboratorio e di ufficio SaraC., Regina, Francesca, Marianna, Angelica, SaraL., Angela e Sohail. In questa nostra esperienza inizialmente da ''coinquilini'' di spazi e poi da colleghi e amici, desidero porgere a loro il mio più caloroso grazie. Nonostante le differenze nelle tematiche di ricerca, il dialogo che ne è derivato ha portato ad uno scambio costruttivo e di supporto reciproco, arricchendo il mio percorso con nuove prospettive e idee.

Un grazie a tutto il gruppo CNR-NANOTECH di Lecce e al capogruppo la Dott.ssa Rizzo, perché nei miei numerosi viaggi si sono sempre resi disponibili e accoglienti. Concedendomi l'opportunità di imparare nuove metodologie con estrema onestà intellettuale.

Desidero esprimere la mia gratitudine a tutto il gruppo INAM in Spagna, che mi ha accolto per nove mesi facendomi sentire parte integrante della loro squadra. Un ringraziamento speciale va al Prof. Iván Mora Serò, la cui inesauribile dedizione nell'affrontare ogni sfida è un esempio

prezioso e una fonte costante di ispirazione. Alla Prof.ssa Masi, sono profondamente grata per avermi insegnato il valore dell'equilibrio e l'importanza di saper voltare pagina con consapevolezza e serenità. Inoltre, la sua passione per la scienza e la sua capacità di affrontare ogni aspetto della ricerca con un approccio meticoloso e umile sono state fondamentali per il mio percorso, ispirandomi a vedere ogni ''tentativo di ricerca'' come un'opportunità di crescita continua e non come un fallimento. Un grazie a tutti i ragazzi in particolare Carina, Sergio, Alex, Fabian, Teresa, Olfa, Thais, Jeevan and Jesus per avermi regalato uno dei periodi che più caldamente hanno rappresentato la bellezza di questi 3 anni.
Concludo con il ringraziamento più intimo e meno formale, quello per la mia splendida famiglia. La loro costante vicinanza mi dà la stabilità e il coraggio di affrontare le tempeste e di restare salda. A mio marito, che mi ha spronata anche a prolungare il periodo estero, dimostrando sempre fiducia nelle mie scelte e nel mio percorso, e a cui devo tanto per la sua pazienza, il suo amore incondizionato e il suo sostegno incessante.

La borsa di dottorato è stata cofinanziata con risorse del
Programma Operativo Nazionale Ricerca e Innovazione 2014-2020, risorse FSE REACT-EU
Azione IV.4 “Dottorati e contratti di ricerca su tematiche dell’innovazione”
e Azione IV.5 “Dottorati su tematiche Green”.

The doctoral scholarship was co-funded with resources from the National Operational Programme for Research and Innovation 2014-2020, FSE REACT-EU resources, Action IV.4 "Doctoral and research contracts on innovation topics" and Action IV.5 "Doctorates on Green topics".